

**STRUCTURAL SYSTEMS
RESEARCH PROJECT**



PB98-174501

Report No.
SSRP - 97/17

**EXPERIMENTAL INVESTIGATION OF
DUCTILITY OF IN-GROUND HINGES IN
SOLID AND HOLLOW PRESTRESSED
PILES**

by

**Andrew M. Budek
Gianmario Benzoni
M.J. Nigel Priestley**

Final Report on a Research Project funded by Caltrans under
Contract No. DOT 59V375

November 1997

Division of Structural Engineering
University of California, San Diego
La Jolla, California 92093-0085



DISCLAIMER

This document contains
tone-on-tone or color
graphs, charts and/or pictures
which have been reproduced in
black and white.



Structural Systems Research Project

Report No. SSRP-97/17

**EXPERIMENTAL INVESTIGATION OF DUCTILITY OF
IN-GROUND HINGES IN SOLID AND HOLLOW
PRESTRESSED PILES**

by

Andrew M. Budek

Gianmario Benzoni

M.J. Nigel Priestley

Final Report on a Research Project funded by Caltrans
under Contract No. DOT 59V375

November 1997



Memorandum

To: JAMES E. ROBERTS, Director
Engineering Service Center

Date: September 2, 1998
File: 59V375-Area 3
Report SSRP-97/17
900.17

From: DEPARTMENT OF TRANSPORTATION
Engineering Service Center
Office of Earthquake Engineering and Design Support

Subject: Final Report for Caltrans "Problem Focused Study" Project Titled:

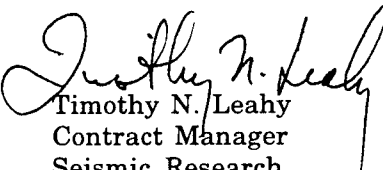
**"Experimental Investigation of
Ductility of In-Ground Hinges in
Solid and Hollow Prestressed Piles"**

The attached report was completed as part of the proposed work in contract #59-V-375, a Research Technical Agreement between Caltrans and the University of California, San Diego, for the project titled; "Coordinated Seismic Bridge Research Program at the University of California, San Diego" The authors are: Andrew M. Budek, Gianmario Benzoni, and M.J. Nigel Priestly. The report number is "UCSD/SSRP-97/17". This is the fourth final report of 4 that has been produced as the product of "Area 3 of 3" of the contract; and is one of 11 reports that will be produced from this contract.

The primary goal of this part of the research study was to investigate column/pile shafts, prestressed solid piles, and prestressed hollow piles. A summary of the conclusions of this report begins on page 104; and includes the following:


- Solid prestressed piles have a considerably greater plastic potential than has been previously believed.....
- Hollow prestressed piles have remarkable in-sensitivity to most parameter variations, and their use should be for members in the elastic range.....
- Glass-fibre jacketed solid prestressed piles (in the configuration tested) are not suitable for use in the sub-grade hinge range of a pile/shaft.....

The total contract cost was \$1,427,000, and the original performance period was August 1, 1993 thru January 31, 1996. Amendment #1 extended the termination to March 31, 1997.


Timothy N. Leahy
Contract Manager
Seismic Research

Attach

cc: Jallison, ESC Deputy Director
CT Hdqrts Library
TRC
Design Sections (14 copies)
Office Chiefs (except noted)
Seismic Seniors & Specialists
Other State contact list

1. Report No. SSRP-97/17	2. Government Accession  PB98-174501	3. Recipient's Catalog No.	
4. Title and Subtitle EXPERIMENTAL INVESTIGATION OF DUCTILITY OF IN-GROUND HINGES IN SOLID AND HOLLOW PRESTRESSED PILES		5. Report Date November 1997	
		6. Performing Organization Code	
7. Author(s) Andrew M. Budek, Gianmario Benzoni, M.J. Nigel Priestley		8. Performing Organization Report No.	
9. Performing Organization Name and Address Division of Structural Engineering School of Engineering University of California, San Diego La Jolla, California 92093-0085		10. Work Unit No. (TRAIS)	
		11. Contract or Grant No. 59V375	
12. Sponsoring Agency Name and Address California Department of Transportation Division of Structures 1801 30th Street Sacramento, California 95807		13. Type of Report and Period Covered	
		14. Sponsoring Agency Code	
15. Supplementary Notes			
16. Abstract <p>Analytical studies have indicated that, in developing the full inelastic potential of the pile-cap connection, a plastic hinge may be expected to form in the pile shaft. An experimental programme of six solid and four hollow prestressed piles was completed. Parameters varied in the solid pile test programme were transverse reinforcement levels, presence and absence of external confinement (as would be provided by soil in an <i>in situ</i> pile), and the addition of a glassfibre jacket to the plastic hinge region. The hollow piles varied transverse reinforcement, presence and absence of external confinement, and the addition of nonprestressed longitudinal reinforcement to the plastic hinge region. In the case of solid piles, external confinement greatly increased ductility capacity, to the point that only light transverse reinforcement ($\rho_t=0.005$) was needed to provide acceptable inelastic performance. In the absence of external confinement, somewhat more reinforcement ($\rho_t\approx 0.015$) would provide more than enough rotational capacity. Glassfibre jacketing significantly increased maximum flexural strength at the expense of ductility, and at the cost of an undesirable failure mode (complete tendon rupture); glassfibre jackets in the configuration tested can therefore only be recommended when ductility demands are low to moderate. The hollow piles tested failed through compression failure of the shell. The performance of hollow prestressed piles was insensitive to transverse reinforcement and external confinement, and ductility capacity was reduced by the inclusion of nonprestressed longitudinal reinforcement.</p>			
17. Key Words		18. Distribution Statement Final report	
19. Security Classification (of this report) Unclassified	20. Security Classification (of this page) Unclassified	21. No. of Pages ~127	22. Price



Acknowledgments

The research described in this report was funded by the California Department of Transportation (CALTRANS) under contract DOT-59V375. Conclusions and recommendations in this report are those of the authors alone; endorsement by CALTRANS is neither expressed nor implied.

Special thanks are due to Utility Vault Co., of Fontana, California, for the donation of pile shaft test units PS7 - PS16 described herein, and to Hexcell/Fyfe, of San Diego, California, for the glassfibre wraps of PS15 and PS16.



Table of Contents

Acknowledgments	ii
Table of Contents	iii
List of Figures	iv
List of Tables.....	xii
List of Symbols.....	xiii
Abstract.....	xv
1. Introduction.....	1
2. Theoretical Background and Previous Experimental Work.....	3
2.1 Analysis of the test units.....	3
2.2 Experimental work on pile shaft response.....	3
3. Experimental Apparatus and Pile Shaft Test Units.....	14
3.1 Experimental Apparatus	14
3.2 Solid Pile Shaft Test Units PS7-PS10	17
3.3 Hollow Piles PS11-PS14	21
3.4 Solid Prestressed Piles with Glassfibre Jackets.....	25
4. Experimental Procedure.....	31
4.1 Loading schedule, solid prestressed piles PS7-PS10	31
4.2 Loading schedule, hollow prestressed piles PS11-PS14	32
4.3 Loading schedule, glassfibre-jacketed piles	33
4.4 Instrumentation.....	34
5. Results - Solid Prestressed Piles.....	36
5.1 PS7	36
5.2 PS8	40
5.3 PS9	45
5.4 PS10	49
5.5 Comparisons between Solid Prestressed Piles PS7-PS10	54
6. Results - Hollow Prestressed Piles	62
6.1 PS11	62
6.2 PS12.....	68
6.3 PS13	74
6.4 PS14.....	79
6.5 Comparisons between the Hollow Piles Tests	84
7. Results - Glassfibre-Jacketed Solid Prestressed Piles	90
7.1 PS15	90
7.2 PS16.....	96
7.3 Comparisons between PS15, PS16, and PS10 (unjacketed)	101
8. Conclusions	104
9. References.....	107



List of Figures

Fig. 1.1: Prototype prestressed pile moment vs. height.....	1
Fig. 1.2: Solid prestressed pile shaft test units PS7-PS10 - theoretical moment patterns	2
Fig. 2.1: Comparison of spans and loading points of pile tests described by Sheppard (drawings are to true scale)	5
Fig. 2.2: Configuration of pile test units described by Ikeda et al (drawn to scale)	6
Fig. 2.3: Pile test configuration described by Banerjee et al (drawn to scale)	8
Fig. 2.4: Pile test configuration described by Falconer and Park (drawn to scale; piles tested by Pam, Park, and Priestley were similar).....	9
Fig. 2.5: Pile test configuration described by Muguruma et al (drawn to scale).....	12
Fig. 2.6: Cast-in-place pile test configuration by Budek, Benzoni, and Priestley (drawn to scale; PS2 omitted the center load point)	13
Fig. 2.7: Comparison of geometry and loading of previous pile body tests with present work (drawings do not necessarily imply unidirectional loading; axial loading, where present, omitted for clarity)	13
Fig. 3.1: General arrangement of test apparatus used for PS7-10 (scrap views: for PS7 and PS8 the center actuator was removed, and load ratio C was thus zero).....	14
Fig. 3.2: Pile shaft test rig, PS9 and PS10 configuration.....	15
Fig. 3.3: Cross-section of loading apparatus used for pile shaft test units PS7-10	16
Fig. 3.4: Axial load mechanism - top view.....	16
Fig. 3.5: Side view of axial load strongback and leveling mechanism	16
Fig. 3.6: Dimensional and reinforcement details of pile shaft test units PS7 - PS10	18
Fig. 3.7: Theoretical moment-curvature data for pile shaft test units PS7 - PS10, using actual material properties.....	18



Fig. 3.8: Prestressed piles in casting beds, prior to cast	20
Fig. 3.9: Prestressed piles being cast	20
Fig. 3.10: Comparison of theoretical shear capacity with experimentally observed shear, pile shaft test unit PS10	21
Fig. 3.11: Dimensional and reinforcement details of pile shaft test units PS11 and PS14.....	22
Fig. 3.12: Dimensional and reinforcement details of pile shaft test units PS12 and PS13.....	22
Fig. 3.13: Theoretical moment-curvature data for pile shaft test units PS11 - PS14, using actual material properties (axial load of 890 kN).....	24
Fig. 3.14: Hollow prestressed pile in casting bed, prior to cast. Note Sonovoid™ used to form void.	24
Fig. 3.15: Comparison of theoretical shear capacity with experimentally observed shear, hollow pile PS12	25
Fig. 3.16: Dimensional and reinforcement details of pile shaft test units PS15 and PS16	26
Fig. 3.17: Theoretical moment-curvature data for pile shaft test units PS15 and PS16, using actual material properties (axial load of 890 kN); PS10 (unjacketed) included for reference	26
Fig. 3.18: Glassfibre wraps applied to prestressed pile shaft test units PS15 and PS16	28
Fig. 3.19: Transverse cut through jacket of PS16.....	29
Fig. 3.20: Application of glassfibre wrap to pile shaft test unit PS15	29
Fig. 3.21: Comparison of theoretical shear capacity with experimentally observed shear, glassfibre-jacketed solid prestressed pile PS15	30
Fig. 4.1: Transverse steel strain gauge locations.....	35



Fig. 4.2: Mounting of displacement transducers to measure curvature, test units PS7 - PS10.....	35
Fig. 5.1.1: Prestressed pile shaft test unit PS7 at $\mu=3$	37
Fig. 5.1.2: Prestressed pile shaft test unit PS7 at $\mu=6$	37
Fig. 5.1.3: Force-displacement hysteresis loops for pile shaft test unit PS7	38
Fig. 5.1.4: Moment-curvature hysteresis loops about the center of prestressed pile shaft test unit PS7.....	38
Fig. 5.1.5: Curvature profiles for pile shaft test unit PS7	39
Fig. 5.1.6: Confining steel strain, prestressed pile shaft test unit PS7	39
Fig. 5.1.7: Shear steel strain, prestressed pile shaft test unit PS7	40
Fig. 5.2.1: Prestressed pile shaft test unit PS8 at $\mu=6$	41
Fig. 5.2.2: Buckling of strands within prestressing tendons in PS8 at $\mu=6$	41
Fig. 5.2.3: Force-displacement hysteresis loops for pile shaft test unit PS8	42
Fig. 5.2.4: Moment-curvature hysteresis loops about longitudinal midpoint, prestressed pile shaft test unit PS8	43
Fig. 5.2.5: Curvature profiles, prestressed pile shaft test unit PS8.....	43
Fig. 5.2.6: Confining steel strains, prestressed pile shaft test unit PS8.....	44
Fig. 5.2.7: Shear steel strains, prestressed pile shaft test unit PS8.....	44
Fig. 5.3.1: Prestressed pile shaft test unit PS9 at $\mu=8$	46
Fig. 5.3.2: Detail of crushing and spalling of cover, PS9 at $\mu=8$	46
Fig. 5.3.3: Force-displacement hysteresis loops for pile shaft test unit PS9	47
Fig. 5.3.4: Moment-curvature hysteresis loops about test unit midpoint, prestressed pile shaft test unit PS9	47



Fig. 5.3.5: Curvature profiles, prestressed pile shaft test unit PS9.....	48
Fig. 5.3.6: Confining steel strains, prestressed pile shaft test unit PS9.....	48
Fig. 5.3.7: Shear steel strains, prestressed pile shaft test unit PS9.....	49
Fig. 5.4.1: Prestressed pile shaft test unit PS10 at $\mu=8$	50
Fig. 5.4.2: Initial asymmetry of plastic hinge of pile shaft test unit PS10	50
Fig. 5.4.3: Force-displacement hysteresis loops for pile shaft test unit PS10	51
Fig. 5.4.4: Moment-curvature hysteresis loops about test unit midpoint, prestressed pile shaft test unit PS10	52
Fig. 5.4.5: Curvature profiles, prestressed pile shaft test unit PS10.....	52
Fig. 5.4.6: Confining steel strains, prestressed pile shaft test unit PS10.....	53
Fig. 5.4.7: Shear steel strains, prestressed pile shaft test unit PS10	53
Fig. 5.5.1: Comparison of force-displacement hysteresis loops for prestressed pile shaft test units PS7 - PS10.....	54
Fig. 5.5.2: Force-displacement envelopes for PS7 ($\rho_t=0.015$) and PS8 ($\rho_t=0.010$); no external confinement about plastic hinge	55
Fig. 5.5.3: Force-displacement envelopes for PS9 ($\rho_t=0.010$) and PS10 ($\rho_t=0.005$); with external confinement about plastic hinge.....	56
Fig. 5.5.4: Force-displacement envelopes for PS8 ($\rho_t=0.010$) and PS9 ($\rho_t=0.010$); PS8 with no external confinement about plastic hinge, PS9 with external confinement	56
Fig. 5.5.5: Determination of plastic rotation	57
Fig. 5.5.6: Comparison of moment-curvature hysteresis loops for prestressed pile shaft test units PS7 - PS10.....	59
Fig. 5.5.7: Curvature profiles, PS7 ($\rho_t=0.015$) and PS8 ($\rho_t=0.010$); no external confinement	60



Fig. 5.5.8: Curvature profiles, PS9 ($\rho_t=0.010$) and PS10 ($\rho_t=0.005$); with external confinement	60
Fig. 5.5.9: Curvature profiles, PS8 and PS9 (both $\rho_t=0.010$); PS9 with external confinement, PS8 without	61
Fig. 6.1.1: Push-cycle compression zone of PS11 after removal of fixturing (heavy reinforcement, plastic hinge confined)	63
Fig. 6.1.2: PS11 after sectioning, showing spalled area of core face (heavy reinforcement, plastic hinge confined)	63
Fig. 6.1.3: The spalled cover of PS11 could be easily removed, showing that the damage went all the way through the shell (heavy reinforcement, plastic hinge confined)	64
Fig. 6.1.4: Force-deflection hysteresis loops for hollow pile shaft test unit PS11 (heavy reinforcement, plastic hinge confined)	65
Fig. 6.1.5: Interpolated critical section core strain envelope vs. curvature for hollow pile shaft test unit PS11, push cycles (heavy reinforcement, plastic hinge confined)	65
Fig. 6.1.6: Moment-curvature hysteresis loops at longitudinal midpoint, hollow pile PS11 (heavy reinforcement, plastic hinge confined)	66
Fig. 6.1.7: Curvature profiles, hollow pile PS11 (heavy reinforcement, plastic hinge confined)	66
Fig. 6.1.8: Confining steel strain, hollow pile test unit PS11 (plastic hinge confined, heavy reinforcement)	67
Fig. 6.1.9: Shear steel strain, hollow pile PS11 (heavy reinforcement, plastic hinge confined)	67
Fig. 6.2.1: Hollow pile PS12, compression zone failure (medium reinforcement, plastic hinge unconfined)	68
Fig. 6.2.2: Hollow pile PS12, buckled prestressing tendons (medium reinforcement, plastic hinge unconfined)	69
Fig. 6.2.3: Spalling and tendon buckling on hollow pile test unit PS12 (medium reinforcement, plastic hinge unconfined)	70



Fig. 6.2.4: Force-displacement hysteresis loops for hollow pile shaft test unit PS12 (medium reinforcement, plastic hinge unconfined).....	70
Fig. 6.2.5: Interpolated critical section core strain envelope vs. curvature for hollow pile shaft test unit PS12, push cycles (medium reinforcement, plastic hinge unconfined)	71
Fig. 6.2.6: Moment-curvature hysteresis loops at longitudinal midpoint, hollow pile PS12 (medium reinforcement, plastic hinge unconfined).....	72
Fig. 6.2.7: Curvature profiles, hollow pile PS12 (medium reinforcement, plastic hinge unconfined)	72
Fig. 6.2.8: Confining steel strains, hollow pile PS12 (medium reinforcement, plastic hinge unconfined)	73
Fig. 6.2.9: Shear steel strain, hollow pile PS12 (medium reinforcement, plastic hinge unconfined)	73
Fig. 6.3.1: Initial compression failure of hollow pile PS13 (medium reinforcement, plastic hinge unconfined, dowels in p.h. region)	74
Fig. 6.3.2: Close-up of compression zone failure, hollow pile PS13 (medium reinforcement, plastic hinge unconfined, dowels in p.h. region)	75
Fig. 6.3.3: Force-deflection hysteresis loops for hollow pile shaft test unit PS13 (medium reinforcement, plastic hinge unconfined, dowels in p.h. region).....	76
Fig. 6.3.4: Interpolated critical section core strain envelope vs. curvature for hollow pile shaft test unit PS13, final push cycle(medium reinforcement, plastic hinge unconfined, with mild steel dowels in p.h. region).....	77
Fig. 6.3.5: Moment-curvature hysteresis loops at test unit midpoint, hollow pile PS13 (medium reinforcement, plastic hinge unconfined, with mild steel dowels in p.h. region).....	77
Fig. 6.3.6: Curvature profiles, hollow pile PS13 (medium reinforcement, plastic hinge unconfined, with mild steel dowels in p.h. region).....	78
Fig. 6.3.7: Confining steel strains, hollow pile PS13 (medium reinforcement, plastic hinge unconfined, with mild steel dowels in p.h. region)	78



Fig. 6.3.8: Shear steel strains, hollow pile PS13 (medium reinforcement, plastic hinge unconfined, with mild steel dowels in p.h. region).....	79
Fig. 6.4.1: Hollow pile PS14 at $\mu=4$ (light reinforcement, plastic hinge confined).....	80
Fig. 6.4.2: Force-displacement hysteresis loops for hollow pile shaft test unit PS14 (light reinforcement, plastic hinge confined).....	81
Fig. 6.4.3: Interpolated critical section core strain envelope vs. curvature for hollow pile shaft test unit PS14, push cycles (light reinforcement, plastic hinge confined).....	82
Fig. 6.4.4: Moment-curvature hysteresis loops at longitudinal midpoint, hollow pile PS14 (light reinforcement, plastic hinge confined).....	82
Fig. 6.4.5: Curvature profiles, hollow pile PS14 (light reinforcement, plastic hinge confined).....	83
Fig. 6.4.6: Confining steel strains, hollow pile PS14 (light reinforcement, plastic hinge confined).....	83
Fig. 6.4.7: Shear steel strain, hollow pile PS14 (light reinforcement, plastic hinge confined).....	84
Fig. 6.5.1: Comparison of force-displacement envelopes, PS11 (heavy transverse reinforcement) and PS14 (light transverse reinforcement)	85
Fig. 6.5.2: Comparison of core strain, PS11 (heavy transverse reinforcement) and PS14 (light transverse reinforcement)	85
Fig. 6.5.3: Comparison of force-displacement envelopes, PS12 (no nonprestressed reinforcement in plastic hinge region) and PS13 (with nonprestressed longitudinal reinforcement in plastic hinge region).....	86
Fig. 6.5.4: Comparison of core strain, PS12 (no nonprestressed reinforcement in plastic hinge region) and PS13 (with nonprestressed longitudinal reinforcement in plastic hinge region).....	87
Fig. 6.5.5: Comparison of force-displacement hysteresis loops for hollow piles PS11 - PS14: a) PS11 (heavy reinforcement, plastic hinge confined); b) PS12 (medium reinforcement, plastic hinge unconfined); c) PS13 (medium reinforcement, plastic hinge unconfined).....	88



Fig. 7.1.1: Pile shaft test unit PS15 at $\mu=8$ (low reinforcement, glassfibre-jacketed, jacket uncut).....	90
Fig. 7.1.2: Flexure crack in jacket of PS15 (low reinforcement, glassfibre-jacketed, jacket uncut).....	91
Fig. 7.1.3: Jacket removed from PS15's pull-cycle compression side; note "notch" where concrete has been crushed and has powdered away (low reinforcement, glassfibre-jacketed, jacket uncut)	91
Fig. 7.1.4: Ruptured and buckled tendons, PS15 (low reinforcement, glassfibre-jacketed, jacket uncut).....	92
Fig. 7.1.5: Force-displacement hysteresis loops for pile shaft test unit PS15 (jacket uncut, plastic hinge confined).....	93
Fig. 7.1.6: Moment-curvature hysteresis loops (at longitudinal midpoint) for glassfibre-jacketed prestressed pile PS15 (jacket uncut, plastic hinge confined)	94
Fig. 7.1.7: Curvature profiles for glassfibre-jacketed prestressed pile PS15 (jacket uncut, plastic hinge confined).....	94
Fig. 7.1.8: Glassfibre jacket confining strains, PS15 (jacket uncut, plastic hinge confined)	95
Fig. 7.1.9: Confining steel strains, glassfibre-jacketed prestressed pile PS15 (jacket uncut, plastic hinge confined).....	95
Fig. 7.1.10: Shear steel strains, glassfibre-jacketed prestressed pile PS15 (jacket cut, plastic hinge confined)	96
Fig. 7.2.1: Pile shaft test unit PS16 at $\mu=8$, showing flexure crack in jacket (low reinforcement, glassfibre-jacketed, jacket cut).....	97
Fig. 7.2.2: Midline flexural crack in PS16 (glassfibre jacket with transverse cuts, plastic hinge unconfined)	97
Fig. 7.2.3: Force-displacement hysteresis loops, pile shaft test unit PS16 (glassfibre jacket with transverse cuts, plastic hinge unconfined).....	98
Fig. 7.2.4: Moment-curvature hysteresis loops, PS16 (glassfibre jacket with transverse cuts, plastic hinge unconfined).....	99



Fig. 7.2.5: Curvature profiles, pile shaft test unit PS16 (glassfibre jacket with transverse cuts, plastic hinge unconfined).....	99
Fig. 7.2.6: Glassfibre jacket strains, PS16 (glassfibre jacket with transverse cuts, plastic hinge unconfined)	100
Fig. 7.2.7: Confining steel strains, PS16 (glassfibre jacket with transverse cuts, plastic hinge unconfined)	100
Fig. 7.2.8: Shear steel strains, PS16 (glassfibre jacket with transverse cuts, plastic hinge unconfined)	101
Fig. 7.3.1: Force-displacement envelopes, PS10, PS15, and PS16	102
Fig. 7.3.2 : Comparison of curvature profiles: a) PS15 (glassfibre jacket, plastic hinge confined); b) PS16 (glassfibre jacket w/transverse slits, plastic hinge unconfined); c) PS10 (unjacketed, plastic hinge confined)...all had transverse reinforcement $\rho_t=0.005$	102

LIST OF TABLES

Table 1.1: Prestressed pile test unit parameters varied	2
Table 3.1: Prestressed pile shaft test unit PS7-10 material properties.....	18
Table 3.2: Prestressed pile shaft test unit PS7-10 theoretical shear strength.....	21
Table 3.3: Hollow prestressed pile shaft test unit PS11-14 material properties.....	23
Table 3.4: Hollow prestressed pile shaft test unit PS11-14 theoretical shear strength	25
Table 3.5: Glassfibre-jacketed solid prestressed pile shaft test unit PS15-16 material properties	26
Table 3.6: Glassfibre-jacketed prestressed pile shaft test unit PS15-16 theoretical shear strength	30
Table 4.1: Ultimate ductilities achieved, PS7-10.....	32
Table 4.2: Ultimate ductilities achieved, PS11-14.....	33
Table 4.3: Ultimate ductilities achieved, PS15-16.....	34
Table 5.1: Predicted vs. actual plastic hinge lengths, PS7-10	57
Table 5.2: Predicted vs. actual ultimate displacement, PS7-10	58
Table 6.1: Predicted vs. actual plastic hinge lengths, hollow piles PS11-14.....	88
Table 6.2: Predicted vs. actual ultimate displacement, hollow piles PS11-14	89
Table 7.1: Predicted and actual plastic hinge lengths, glassfibre-jacketed piles PS15 and PS16	103



Table 7.2: Predicted vs. actual ultimate displacement, glassfibre-jacketed piles PS15 and PS16.....	103
--	-----

List of Symbols

A_e	- effective area (taken as $0.8A_g$)
A_g	- gross section area
A_s	- transverse steel bar area
D	- section diameter
D'	- transverse reinforcement spiral diameter
E_j	- glassfibre jacket elastic modulus
M	- moment
P	- maximum shear load
P_e	- axial load
V_c	- concrete shear-resisting mechanism of a circular section
V_p	- axial-load enhancement of shear-resistance
V_s	- reinforcing steel truss shear-resisting mechanism of a circular section
b	- transverse dimension of load saddle
c	- cover to clear spiral steel
f_c	- strength of unconfined concrete
f_e	- external confining pressure
f_l	- confining pressure from transverse steel
f_{pu}	- ultimate strength of prestressing tendons
f_{py}	- yield strength of prestressing tendons
f_u	- ultimate steel strength
f'_{uj}	- glassfibre jacket ultimate strength
f_y	- steel yield strength
f_{yh}	- yield strength of transverse reinforcement
l	- half-length of loaded area of test unit
l_p	- plastic hinge length
s	- pitch of transverse reinforcing spirals
t_j	- glassfibre jacket thickness
x	- neutral axis depth
Δ	- displacement
$\Delta_{ult, exp.}$	- ultimate measured displacement
$\Delta_{ult, pred.}$	- ultimate predicted displacement
Φ	- strength reduction factor
Θ	- angle between shear cracks and pile axis
Θ_p	- plastic rotation
Θ_y	- rotation at design strength (corresponding to extreme fibre $\epsilon_c=0.004$)



α	- angle of axial-load-induced compression strut to pile axis
ϵ_c	- concrete compression strain
ϵ_{cu}	- ultimate allowable concrete compression strain
ϵ_{sm}	- steel strain at maximum confining steel stress
ϵ_{uj}	- glassfibre jacket ultimate strain
μ, μ_Δ	- displacement ductility
μ_ϕ	- curvature ductility
ϕ_{ult}	- ultimate curvature
ϕ_{yield}	- curvature at design strength (corresponding to extreme fibre $\epsilon_c=0.004$)
ρ_t	- volumetric ratio of transverse reinforcement



Abstract

Analytical studies have indicated that, in developing the full inelastic potential of the pile-cap connection, a plastic hinge may be expected to form in the pile shaft. An experimental programme of six solid and four hollow prestressed piles was completed. Parameters varied in the solid pile test programme were transverse reinforcement levels, presence and absence of external confinement (as would be provided by soil in an *in situ* pile), and the addition of a glassfibre jacket to the plastic hinge region. The hollow piles varied transverse reinforcement, presence and absence of external confinement, and the addition of nonprestressed longitudinal reinforcement to the plastic hinge region. In the case of solid piles, external confinement greatly increased ductility capacity, to the point that only light transverse reinforcement ($\rho_t=0.005$) was needed to provide acceptable inelastic performance. In the absence of external confinement, somewhat more reinforcement ($\rho_t\approx 0.015$) would provide more than enough rotational capacity. Glassfibre jacketing significantly increased maximum flexural strength at the expense of ductility, and at the cost of an undesirable failure mode (complete tendon rupture); glassfibre jackets in the configuration tested can therefore only be recommended when ductility demands are low to moderate. The hollow piles tested failed through compression failure of the shell. The performance of hollow prestressed piles was insensitive to transverse reinforcement and external confinement, and ductility capacity was reduced by the inclusion of nonprestressed longitudinal reinforcement.



1. INTRODUCTION

This is a summary report on the testing of prestressed pile shaft units PS7 - PS16, performed to help characterize the subgrade hinge in solid, hollow, and solid glassfibre-jacketed prestressed piles. This series of tests investigated the effect of transverse reinforcement, and the confining effect of soil on the structure's performance.

The motivation for this series of tests was the indication from extensive theoretical analyses^[1] that the development of the full inelastic capacity of a pile-cap connection would require the formation of a plastic hinge in the pile shaft. Previous experimental work in this program dealt with model CIDH pile shafts^[15].

The test apparatus was designed to simulate a symmetrical moment pattern between points of contraflexure in an in-situ prototype, as derived from theoretical analysis based on a bilinear soil model described in reference [1]. This series of tests, PS7-16, loaded the test units through a series of saddles extending 100° about the circumference of the shaft, top and bottom, to simulate lateral confinement by soil. Prototype and representative test unit moment patterns are shown in figs. 1.1 and 1.2.

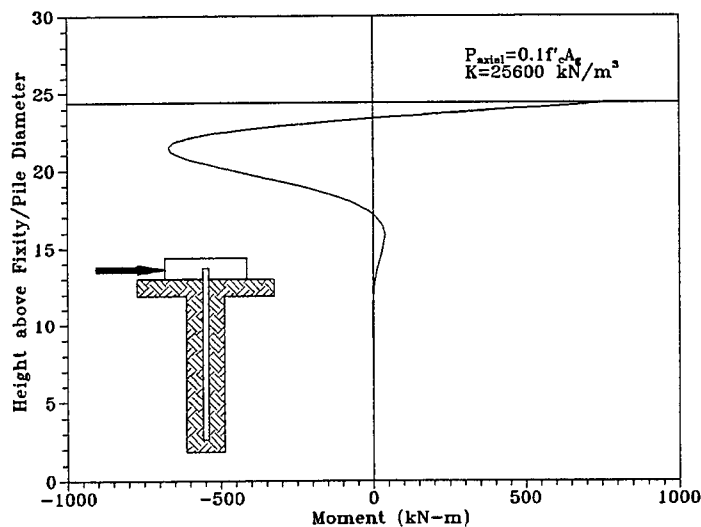


Fig. 1.1: Prototype pile moment vs. height

The prototype solid pile analyzed was a 610 mm diameter section with 24 prestressing tendons of 13.2 mm diameter (area 106 mm², 1860 MPa ultimate, 1302 MPa nominal yield) prestressed at 1061 MPa to give a nominal section prestress of 9.3 MPa. Transverse reinforcement was provided by W11 A82 spiral (D9.5, 565 MPa nominal yield) with a pitch of 63.5 mm, for a transverse reinforcement ratio $\rho_t = 0.011$. Assumed concrete strength for the model was 41.3 MPa

The solid pile test units PS7 through PS10, PS15, and PS16 were designed to full scale in physical dimensions, and retained a similar configuration of prestressing tendons; transverse reinforcement and method of loading (i.e., whether soil pressure about the plastic hinge region was modeled, or not) were varied in this series, as shown in table 1.1.

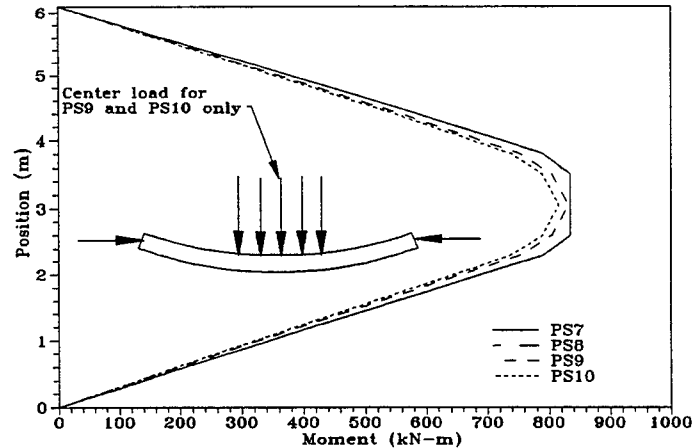


Fig. 1.2: Solid prestressed pile shaft test units PS7-PS10 - theoretical moment patterns

TABLE 1.1: PRESTRESSED PILE TEST UNIT PARAMETERS VARIED

Test Unit	ρ_t (reinforcement details)	Loading Method	Date of Test
PS7 (solid)	0.0151 (W11 A82 @ 41 mm)	Plastic hinge unconfined	May 10, 1996
PS8 (solid)	0.0098 (W11 A82 @ 64 mm)	Plastic hinge unconfined	March 7, 1996
PS9 (solid)	0.0098 (W11 A82 @ 64mm)	Plastic hinge confined	March 28, 1996
PS10 (solid)	0.0054 (W6.5 A82 @ 70mm)	Plastic hinge confined	April 23, 1996
PS11 (hollow)	0.0297 (W8 A82 @ 51mm)	Plastic hinge confined	January 22- 23, 1997
PS12 (hollow)	0.0194 (W8 A82 @ 76mm)	Plastic hinge unconfined	July 9, 1997
PS13 (hollow)	0.0194 (W8 A82 @ 76mm)	Plastic hinge unconfined	July 18, 1997
PS14 (hollow)	0.0117 (W6.5 A82 @ 76mm)	Plastic hinge confined	February 19- 20, 1997
PS15 (solid, glassfibre jacket)	0.0054 (W6.5 A82 @ 70mm)	Plastic hinge confined, jacket uncut	August 12, 1997
PS16 (solid, glassfibre jacket)	0.0054 (W6.5 A82 @ 70mm)	Plastic hinge unconfined, jacket with transverse cuts	August 26, 1997

The hollow pile test units PS11 - PS14 were based upon a 1.22 m diameter marine piling with a 152 mm wall. They were constructed to half-scale; however, the wall

thickness was increased slightly ($t/D=.154$ as opposed to the prototype's $t/D=.125$) to make construction of the test units more practical. Parameters varied in the hollow pile tests were transverse reinforcement ratio, and external confinement to the plastic hinge. Additionally, one test unit (PS13) had nonprestressed longitudinal reinforcement in the plastic hinge region.

The glassfibre-reinforced pile shafts PS15 and PS16 were nominally similar to PS10 in terms of their prestressing and transverse reinforcement. After casting, the plastic hinge regions were wrapped with 7 plies of unidirectional E-glass, with the main fibres running in the transverse (hoop) direction, to provide external confinement.

Glassfibre reinforcement to the plastic hinge region of driven piles was examined as a possible modification to new-build driven precast piles; while it might seem that driving would immediately strip off the jacket, this is not necessarily the case; only the top portion of the pile would need to be jacketed, and the passage of the lower portion of the pile through the soil would tend to degrade the soil's frictional capacity. This, combined with tapering of the leading edge of the jacket, would ameliorate any tendency for the jacket to strip away.

2. THEORETICAL BACKGROUND AND PREVIOUS EXPERIMENTAL WORK

2.1 Analysis of the Test Units

The prototype pile-column and the test units were analyzed using a purpose-designed inelastic finite-element code^[1]. The basic model for the prototype was that of a beam on an elastic foundation, with the pile-column's stiffness reduced after first yield in accordance with discretized moment-curvature data (theoretical moment-curvature data for the test units are shown in section 3). The same code was used for analysis of the test units, with suitable modifications for the different physical configuration.

Previous analytical studies^[1] have indicated that the interaction of soil with a laterally loaded pile would result in a subgrade moment pattern with a relatively broad 'peak', whose depth would be largely determined by soil stiffness and structural geometry of the pile and superstructure. The same general pattern of behavior held true for both linear and nonlinear (bilinear and hyperbolic) soil models. While the use of a hyperbolic soil model (which is based on the small-strain soil modulus, and has greater stiffness through the lower range of lateral displacement) would indicate a sharper peak in the moment curve, the hysteretic degradation of the soil would in practice give the linear and bilinear models the advantage in accuracy. The overall geometry and configuration of the test rig was designed to simulate (to within 2%) a representative moment pattern about the subgrade hinge (i.e., between the points of contraflexure in an *in situ* prototype).

2.2 Experimental Work on Pile Shaft Response

By far the majority of pile tests involve subjecting test piles to loadings and conditions of restraint that coarsely simulate real installations. The reality of pile response is of course much more complicated, because at its heart is a difficult-to-quantify soil-

structure interaction. While a number of in-situ tests have been performed, most have the aim of establishing elastic stiffness at a specific site^[2,3,4,5]. More thorough investigations into nonlinear pile behavior have been undertaken by Cox, Reese, and Grubbs^[6] (Mustang Island, 1974) and Priestley^[7] (Mangere Bridge, 1974). Both Mustang Island and Mangere Bridge validated the use of finite element predictions of pile response (this was particularly important in Priestley's test, in which the soil profile was nonhomogeneous and thus not amenable to an elastic continuum approach). Priestley also instrumented the Mangere Bridge pile in such a way that bending moments, shear force patterns, and pressure distributions could be obtained, giving quantitative confirmation to the analytically-derived assumed patterns.

Sheppard^[8]

Sheppard reported a series of tests on prestressed piles in California. The first, referred to as the 1972 Santa Fe/Pomeroy test, tested two square piles, of 406 mm and 457 mm section, respectively. They were given an effective prestress of 4.82 MPa, and confined with W3.5 A82 spirals at a 150 mm pitch (giving a volumetric ρ_t of less than 0.0025). Axial load levels were 0.29 and 0.22 $f_c A_g$, respectively. The piles were point-loaded at mid-length (they were 13.1 m long); the load was increased monotonically until failure, which was sudden and brittle in both cases, and occurred shortly after the onset of cracking.

The second test detailed by Sheppard is known as the 1974 Santa Fe/Pomeroy test. It consisted of a single 305 mm square pile, with W3.5 spiral at 150 mm (giving a volumetric transverse reinforcement ratio of 0.003). Axial load level was 0.23 $f_c A_g$, and lateral loading was again at mid-length, and monotonic until failure. Failure was again sudden and brittle, with little evidence of ductile behavior.

Sheppard's third reported tests are the 1976 PCMAC/Santa Fe/Pomeroy tests, in which he considered two of the test piles to give significant results. Specimen 1 was identical to the 1974 Santa Fe/Pomeroy test pile, while Specimen 2 utilized a much higher level of transverse reinforcement, provided by W8 A82 spiral at 50 mm ($\rho_t=0.02$). Both test piles had an axial load level of 0.35 $f_c A_g$, and were loaded cyclically in the lateral direction, with full load reversals at each cycle. Two lateral point loads, symmetrically placed about midspan, were applied. Loads were gradually increased as the tests progressed. Specimen 1 showed a similar response to the 1974 test piece; it failed suddenly, and in a brittle manner, shortly after the first cracks were noted. Specimen 2, however, was able to carry its axial load (albeit with a drop in moment capacity) at a level of curvature three times that achieved by Specimen 1 at failure; the test was halted before Specimen 2 was deemed to have failed (displacement ductility capacity for Specimen 2 was $\mu_\Delta=4$ at that point; Specimen 1 achieved $\mu_\Delta=1.17$ at failure).

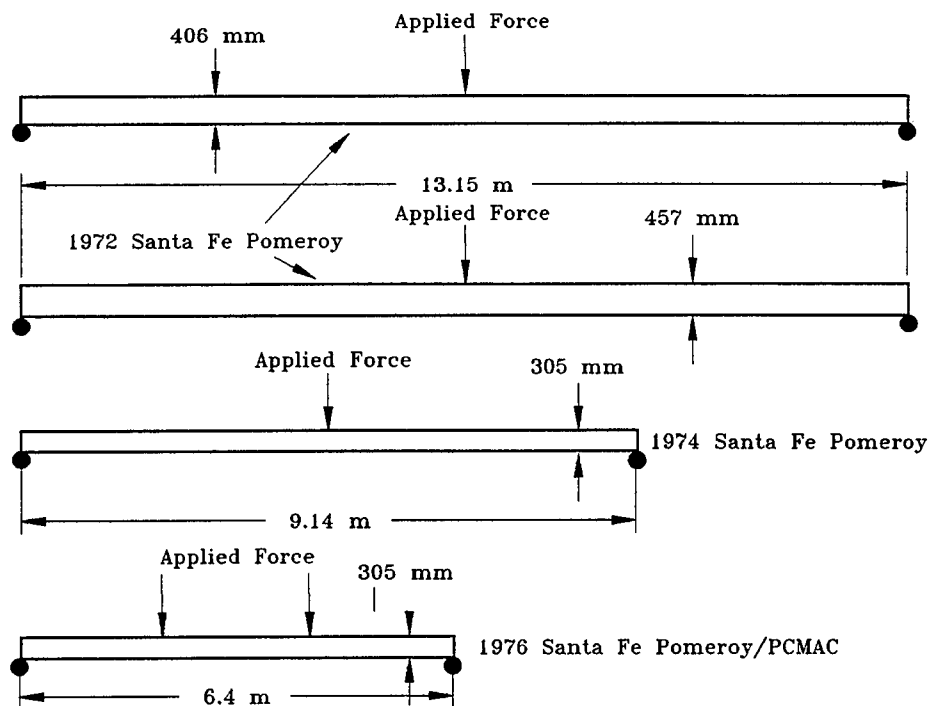


Fig. 2.1: Comparison of spans and loading points of pile tests described by Sheppard (drawings are to true scale)

Sheppard's report on these tests are an important step in developing a rational approach to developing adequate ductility capacity in prestressed pile shafts. He felt that the very light transverse reinforcement seen in the 1972 and 1974 tests precluded the piles' developing any meaningful level of inelastic curvature. He also stated that the axial load levels used in the 1976 tests ($0.35f_cA_g$) were too high, and that $0.2f_cA_g$ was a more realistic figure.

Two features of this series of tests are also of note; first, the piles were axially loaded by post-tensioning through the center of the test piece, which would minimize any possible p-delta effect. Second, the 1972 and 1974 tests utilized single, central point loads, while the 1976 tests had multiple (2) loading points. Given the assumption that the soil surrounding a pile shaft will provide some degree of lateral support (and thus a curved moment pattern), the earlier tests were perhaps unrealistically severe in their modeling of the in situ loading. Also, no effective external confinement (as may be provided by the soil surrounding the pile shaft) was provided to the piles by the loading system.

Ikeda, Tsubaki, and Yamaguchi^[9]

An investigation into the ductility of prestressed piles commonly used in Japan was reported in 1982 by Ikeda, Tsubaki, and Yamaguchi. The piles were circular, hollow section units of 400 mm diameter with a wall thickness of 70 mm. High-strength concrete was used ($f_c=87.4$ MPa). Three groups of tests were described.

The first tests were on piles designated as Type A and Type B; they differed in the number of prestressing tendons used, with Type A having six 9.2 mm tendons (effective section prestress of 6.07 MPa), and Type B, twelve (effective section prestress of 12.14

MPa). Both types A and B had transverse reinforcement consisting of spiral steel with a diameter of 3.2 mm, pitched at 50 mm ($\rho_t=0.0023$). Both cyclic and unidirectional repeated loading regimes were used. Failure was sudden and brittle, occurring at $\mu=4$ for Type A and $\mu=5$ for Type B through fracture of the prestressing tendons. Failure modes were similar for both unidirectional and cyclic loading.

The second group of test piles were modifications of Type A and B piles. Type AR was similar to the Type A described above, but reinforced with six 13 mm deformed steel (non prestressed) bars. Type BR6 was similar to Type B, but had twelve deformed steel reinforcing bars, and 6 mm spiral steel pitched at 50 mm ($\rho_t=0.0081$). The AR pile failed through tendon rupture at $\mu=8$, and BR6 reached $\mu=6$ before failing through the same mechanism. As might be expected, cyclic loading resulted in a greater degree of buckling of the longitudinal steel.

The third group of piles tested in this series were unprestressed piles that were reinforced either by deformed reinforcing steel (Type BRR6; 24 bars) or unstressed prestressing tendons (Type ANN6; 12 tendons). The ANN6 pile failed in a brittle manner after undergoing a yield deflection three times that of a normal type A pile (the large yield deflection being a consequence of the low initial stiffness of the nonprestressed section). The BRR6 piles showed ductile behavior, reaching $\mu=13$ in unidirectional loading and $\mu=8$ in cyclic loading (buckling of the longitudinal steel in cyclic loading resulted in low cycle fatigue failure at the lower ductility level).

The conclusions of the investigators was that the undesirable tendency of high-strength prestressed piles to fail in a brittle manner shortly after yield could be ameliorated in a number of ways: 1) a sufficiently close spacing of transverse reinforcement, to confine the core and prevent shear failure which would prevent the pile from reaching its flexural capacity; 2) addition of nonprestressed longitudinal steel (deformed bars or unstressed tendons), which provide scope for ductile behavior even after rupture of the prestressed tendons.

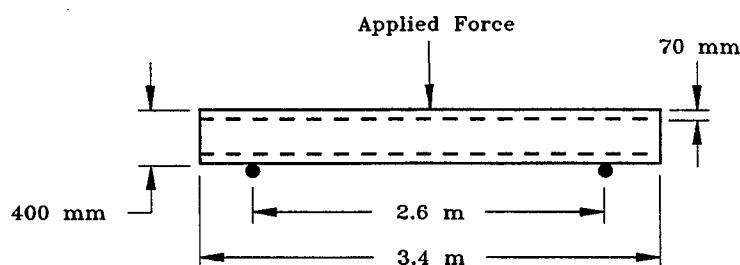


Fig. 2.2: Configuration of pile test units described by Ikeda et al (drawn to scale)

Banerjee, Stanton, and Hawkins^[10]

This group of tests came about from the issuance of the Tentative Proposal for the Development of Seismic Regulations for Buildings, ACT-06, which virtually proscribed the use of precast prestressed piles in regions of high seismicity; the intended requirement was that they not be used to resist flexure unless they remained elastic in Category C structures (structures in regions of high seismicity), and that they not be used at all in structures of Category D (essential structures in regions of the most severe seismicity).

While an industry review of the proposed specifications found them to be overly restrictive, it was felt desirable to analytically measure curvature demands, and experimentally measure curvature capacities.

The experimental phase of this study (it will be recalled that the theoretical aspect of this work, relating to curvature demand, was discussed in the previous section) examined twelve solid prestressed octagonal-section piles of 355 mm diameter, and two hollow octagonal piles of the same outside dimension (the test piles were similar in their structural details to those commonly used in the western United States). The concrete compressive strength in the test piles ranged from 38 to 53 MPa. Two piles contained nonprestressed longitudinal reinforcement additional to the tendons. Confinement was varied: two test units (one solid, and one hollow) utilized W5.5 (6.5 mm diameter) wire pitched at 76 mm. Another solid pile used W3.5 (5.4 mm diameter) wire at 203 mm (giving a volumetric transverse reinforcement ratio of 0.0035). The remainder had W3.5 wire at 102 mm. One of the solid piles had 25 mm of cover concrete; the rest of the piles in the series had 50 mm.

The test units were first subjected to lateral loading, applied cyclically in all but one case. Applied axial loads were varied to represent typical service loading. After being tested as pile shafts, a number of the dead test units were cast into pile cap models for further tests of the pile-pile cap connection (these tests will be discussed in the next section).

The pile shaft test showed that the maximum sustainable curvature could be developed at low axial loads, given adequate transverse reinforcement; addition of additional nonprestressed longitudinal reinforcement did not enhance the piles' ductile performance, and in fact reduced the maximum curvatures achieved. The most lightly reinforced test unit achieved a curvature of about one-third that of the maximum. The two hollow piles failed by implosion at the inner face of the shell, with little effect from their differing levels of transverse reinforcement. All of the solid piles failed through fracture of the spiral and subsequent degradation of the core's compressive capacity. No pile failed in shear.

Conclusions from the experimental program were:

- 1) Pile capacity is most strongly influenced by the level of transverse steel provided, the applied axial load, and the embedment conditions of the pile into the cap.
- 2) Three levels of pile performance, dictated by transverse reinforcement, were identified. a) Piles with $\rho_t < 0.0035$ were deemed unsuitable for most seismic applications; b) Piles with $0.0035 < \rho_t < 0.02$ provided sufficient curvature capacity for most applications; c) Piles with transverse reinforcement ratios above 0.02 were forecast to provide virtually unlimited curvature capacity.
- 3) The addition of additional nonprestressed longitudinal steel does not improve ductility; the amount of transverse steel dictates this aspect of performance.
- 4) The apparent failure mode of hollow piles was implosion of the core surface; the investigators suggested that this mechanism be studied further.

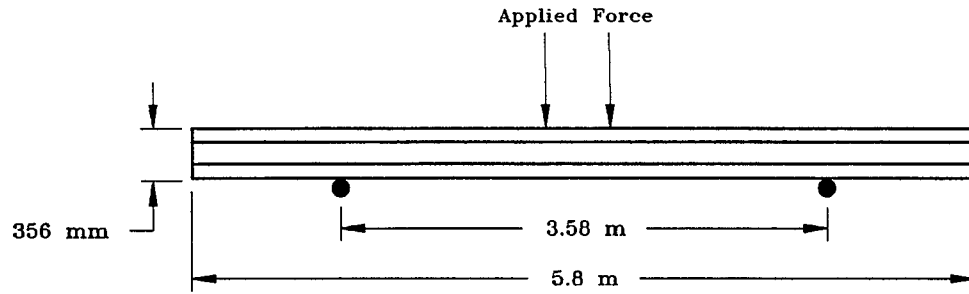


Fig. 2.3: Pile test configuration described by Banerjee et al (drawn to scale)

Falconer and Park^[11]

Because prestressed piles were perceived to lack adequate ductility and curvature capacity for seismic applications, New Zealand designers were turning more often to alternatives such as structural-steel-section piles, concrete-filled steel shells, and reinforced concrete cylinder piles. An investigation was therefore undertaken into whether the provisions of NZS3101^[12], which specified levels of transverse reinforcement for reinforced concrete columns and piers might be adequate for prestressed piles, and so engender confidence in their use.

Five full-scale test piles were constructed, of octagonal cross-section and 400 mm diameter. Each had similar amounts of prestressing steel (ten 12.5 mm strands, giving an effective section prestress of 8.54 MPa), but the quantities of spiral steel were varied; four of the piles were reinforced per NZS3101:

$$\rho_s = 0.45 \left(\frac{A_g}{A_c} - 1 \right) \frac{f'_c}{f_{yh}} \left(0.5 + 1.25 \frac{P_e}{\Phi f'_c A_g} \right) \quad (2.1)$$

or

$$\rho_s = 0.12 \frac{f'_c}{f_{yh}} \left(0.5 + 1.25 \frac{P_e}{\Phi f'_c A_g} \right) \quad (2.2)$$

whichever is greater. In the above equations, A_g is the gross section area, A_c is the core area (measured to the outside of the transverse reinforcement), f'_c is the unconfined concrete strength, f_{yh} is the specified yield strength of the transverse steel, P_e is the axial load due to both gravity and seismic loading, and Φ is the strength reduction factor ($= 0.9$ for confined columns).

One was designed solely for shear resistance, giving only a nominal level of transverse reinforcement. Also, one test pile had ten nonprestressed 20 mm bars. Three levels of applied axial load were tested (0.1 , 0.3 , and $0.6f'_c A_g$); lateral loading was applied through a load stub at midspan, and was cyclic. This method of loading simulated, on either side of the load stub, the area immediately adjacent to the pile cap.

The three piles reinforced per NZS3101 (volumetric transverse steel ratios of 0.0205 , 0.0264 , and 0.0380 , carrying axial loads of 0.1 , 0.3 , and $0.6f'_c A_g$, respectively) performed very well, withstanding ductility levels of $\mu = \pm 8$ without significant degradation

in lateral capacity. The pile that was designed for shear only, with $\rho_t=0.0071$ and an axial load of $0.3F_cA_g$, failed suddenly at the low displacement ductility level of $\mu=2$. Finally, the pile that contained nonprestressed longitudinal reinforcement showed greater energy absorption through cyclic loading, and also had a higher flexural strength.

The investigators concluded that the provisions of NZS3101 could be applied to prestressed piles to good advantage; the specifications of transverse reinforcement were sufficient to provide adequate ductility for seismic applications. Designing transverse reinforcement for shear resistance only was not recommended, as it would provide insufficient confinement to the core concrete and thus allow a sudden degradation and failure of the compression block at low levels of displacement ductility. Addition of nonprestressed longitudinal reinforcement was deemed unnecessary, unless higher flexural strength was required, or bars were needed for the connection to the pile cap.

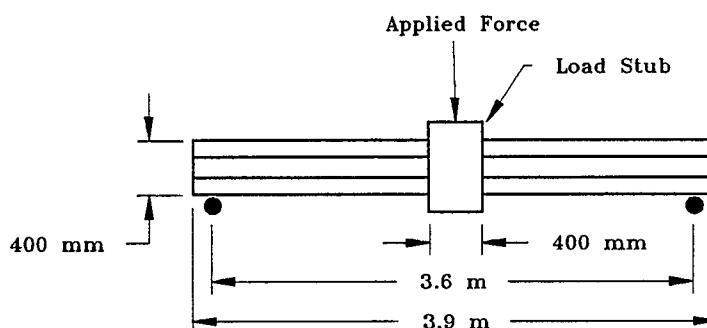


Fig. 2.4: Pile test configuration described by Falconer and Park (drawn to scale; piles tested by Pam, Park, and Priestley were similar)

Pam, Park, and Priestley^[13]

Six test piles (similar those described by Falconer and Park; see fig. 2.4 above) were constructed for a series of tests intended to refine the standards put forward in ATC2-06. These were designed using as a basis the standard bridge designs put forward by the New Zealand Ministry of Works and Development (MWD), and the New Zealand concrete design code, NZS3101. They varied in transverse steel content and grade. No nonprestressed longitudinal reinforcement was used. (Part of this test program included six units testing the pile-pile cap connection; these will be covered in the next section.)

The piles were of 400 mm diameter, with 30 mm of cover to the spiral steel. Ten prestressing tendons of 12.5 mm diameter were used, stressed such that the tensile stress within the strands would not exceed 70% of their nominal ultimate stress immediately after transfer (that is, after tensile stress in the strand is transferred to the body of the pile when the strands are cut loose from the stressing form after the concrete has achieved a specified compressive strength). Transverse reinforcement was provided in the form of Grade 275 mild steel (10 mm in diameter) and Grade 485 hard-drawn wire of 7.5 mm and 9.5 mm diameter. Two piles utilized the mild steel, at 50 and 35 mm pitch, respectively, in the plastic hinge region. The other four used HD wire, at 50, 40, and 30 mm pitch.

The test piles were subjected to cyclic lateral loads, applied at a load stub cast at the longitudinal midpoint of the shaft. This effectively simulated the section of pile adjacent to the cap on both sides of the load stub. Because the load stub could rotate,

measured response during the course of the test was asymmetric, leading to different plastic hinge lengths and ductilities for each half of each test unit. Units P1 through P5 had an applied axial load of $0.3f_c A_g$, while P6 had $0.5f_c A_g$. A reversed cyclic lateral load was applied at the midspan load stub.

Crushing of the cover concrete generally began at $\mu=2$ in all of the test units; ultimate ductilities achieved were very high, ranging from 7.5 to better than 15 for P1, P2, and P4-6 (these are overall displacement ductilities; the aforementioned asymmetry of response resulted in much higher local ductilities adjacent to the load stub). P3 failed suddenly at about $\mu=3.75$ through fracture of spiral steel. P3 offers a direct comparison with P1; both had the same nominal transverse reinforcement (just under 60% of that specified by NZS3101), but P1 used mild steel (Grade 275) while P3 was reinforced with hard drawn Grade 485 wire. The overall displacement ductility reached by P1 was nearly twice what P3 achieved. This can be attributed directly to the properties of the transverse reinforcement; Grade 275 has a relatively low yield strength with a long post-yield plateau, while Grade 485 has virtually no post-yield plateau, and an elongation to fracture of only 11%.

Generally, it was found that hard-drawn wire spiral reinforcement gave satisfactory results if the reinforcement level was equal to or greater than that specified by code. Though spiral fracture did occur in two test piles so reinforced, this happened at ductility levels that would be unrealistic to expect in an actual installation. It was noted that mild steel reinforcement at this level gave results equal to the test units reinforced with hard-drawn wire, but without spiral fracture.

Conclusions drawn from this group of tests were as follows:

- 1) Piles reinforced as per NZS3101, and carrying axial loads of less than $0.5f_c A_g$, achieved an acceptable level of ductility with either mild steel (Grade 275) or hard-drawn wire (Grade 485) reinforcement.
- 2) Piles with less than the code specification of transverse steel should use mild steel spiral to avoid brittle failure of the pile following spiral fracture at low levels of ductility.
- 3) A suggested modification for equations 2.1 and 2.2, specifying confinement for a circular column, is

$$\rho_s = 0.45 \left(\frac{A_g}{A_c} - 1 \right) \frac{f'_c}{f_{yh}} \left(0.5 + \frac{1.25}{\Phi} \left(\frac{P_e}{f'_c A_g} + f_p \right) \right) \quad (2.3)$$

or

$$\rho_s = 0.12 \frac{f'_c}{f_{yh}} \left(0.5 + \frac{1.25}{\Phi} \left(\frac{P_e}{f'_c A_g} + f_p \right) \right) \quad (2.4)$$

in which f_p is the effective prestress force in the section

- 4) Spiral steel in piles using 12.5mm seven-wire strand should be pitched at no more than 50 mm ($4d_b$) to forestall tendon buckling; this may, however, hinder the placement and vibration of the concrete.
- 5) Nonprestressed longitudinal steel is not needed to augment ductility, provided sufficient confining steel is specified. Nonprestressed longitudinal bars may, however, be required in the pile-pile cap connection.

- 6) The plastic hinge length allowed for in the New Zealand code was found to be barely adequate at moderate axial load ($0.3f_c A_g$), and totally inadequate at high axial load ($0.5f_c A_g$).

Muguruma, Watanabe, and Nishiyama^[14]

Four groups of high-strength spun concrete prestressed hollow piles, comprising thirteen test units in all, were tested to determine practical approaches to improving their flexural ductility. Each was 0.4 m in diameter, with a wall thickness of 150 mm, and contained sixteen deformed steel prestressing bars of 9.2 mm diameter. The section prestress was 10 MPa; concrete compressive strength ranged from 95 to 106 MPa, and the piles had 10 mm of cover concrete. Transverse reinforcement varied from *none* to a net volumetric transverse reinforcement ratio (based on net area) of $\rho_t=0.03$ (high-strength wire in diameters of 5, 6, and 7 mm was used; yield strength was 1000 MPa). The piles were each 5 m in length, and were tested in unidirectional flexural loading.

The first group of piles were unconfined, and used prestressing bars with a uniform elongation (that is, the elongation equivalent to the attainment of maximum stress on the stress-strain curve) of 2%. The second group contained of five piles with the same type of prestressing steel as the first, but incorporated spiral steel as described above. The third and fourth groups contained three piles each, with spiral steel, and used prestressing bars whose maximum elongations were 5.13% and 4.73%, respectively.

The unconfined piles of the first group both failed by crushing of the concrete in the compression zone when the peak applied load was achieved; no plastic behavior was to be expected, nor was any observed. The strains in the prestressing bars reached only about 1.26%, far below the nominal 2% at maximum strength.

Confinement of the core changed the picture dramatically; the prestressing bars showed a large post-peak deformation before fracture. The maximum measured flexural strength of the confined piles was similar to that of the unconfined test units; however, the measured tensile strains in the prestressing bars of the confined piles corresponded to elongations of 1.81% in the second group, 4.621% in the third group, and 4.891% in the fourth group. These are clearly close to the unit elongations of 2%, 5.13%, and 4.73% for these groups.

To describe ductility in quantitative terms, the unitary values for displacement (μ_Δ) and curvature (μ_ϕ) ductility were defined by the unconfined test piles; according to this definition, the piles in the second group averaged $\mu_\Delta=1.326$ and $\mu_\phi=1.602$, while the third and fourth groups averaged $\mu_\Delta=2.891$ and $\mu_\phi=4.779$.

This series of tests was intended from the beginning to provide a basis for the formulation of design aids (in the form of design charts) using a curvature ductility approach for the design of piles. Starting from idealized stress-strain curves for concrete and prestressing steel, the derivation involved an estimation of the amount of confining steel necessary to support the needed concrete compression strain that would allow development of the desired level of curvature at the design ultimate load.

Muguruma et al. put forward the following conclusions:

- 1) The flexural capacity of high-strength spun concrete prestressed hollow piles can be significantly enhanced by the use of high-uniform-elongation prestressing steel.

- 2) The unit uniform elongation for prestressing bar should be regarded as its ultimate tensile strain capacity.
- 3) As fracture of the prestressing bars is not a desirable failure mode, care should be taken in specifying levels of transverse reinforcement, as the enhancement of ductility provided by confining steel can result in high tensile strain demands on the prestressing bars.

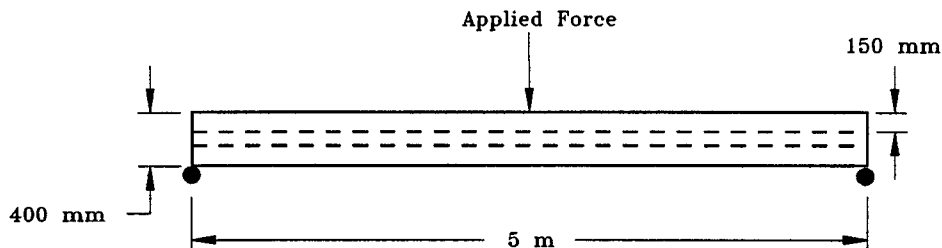


Fig 2.5: Pile test configuration described by Muguruma et al (drawn to scale)

It may be seen from the above survey that there exists a gap in the experimental analysis of piles; namely, the effect of soil confinement on the plastic hinge region of the pile shaft. This was investigated in the following series of tests, which were the direct precursors to the present programme.

Budek, Benzoni, and Priestley^[15]

Six cast-in-place pile shafts, one-third-scale models of a design commonly used by the California Department of Transportation (CALTRANS) for pile-columns, were tested to examine the effect of transverse reinforcement and external confinement (as may be provided by soil) on the below-ground plastic hinge.

All of the test piles had nonprestressed longitudinal reinforcement, provided by 36 #5 Grade 60 bars (D16, 455 MPa nominal yield) for a volumetric longitudinal reinforcement ratio of 0.022. Transverse reinforcement was provided by deformed Grade 60 spiral, pitched to give 0.3%, 0.6%, and 0.9% volumetric ratios. Two piles were constructed at each level of transverse reinforcement. Concrete strength over the series of tests averaged 41 MPa, and these was 25 mm of cover.

The test rig (which was the same used in the testing of PS7 - PS16, here under consideration; see fig. 3.1, 3.2, and 3.3) simulated, through the use of a whiffle tree, a 'generic' subgrade moment pattern that would result from lateral force at the end of an in-situ pile. Two methods of transferring load to the pile were employed: a series of 'saddles' that simulated soil confinement about the pile shaft (see again figs. 3.1-3.3), and pins riding in sleeves cast into the pile, to totally eliminate any external confinement while providing a similar moment pattern. Pairs of test piles with similar level of transverse reinforcement were thus tested with and without external confinement. PS1 ($\rho_t=0.009$) and PS3 ($\rho_t=0.003$) were tested with full external confinement about the plastic hinge region, while PS2 ($\rho_t=0.006$) left the plastic hinge region unconfined, while using the confining fixturing at the outboard load points. PS4, PS5, and PS6 (duplicates of PS1 through PS3, respectively) were loaded through pins. An axial load of 200 kips was applied through the course of the test, providing $11\%f_cA_g$.

The results indicated that the presence of external confinement nearly rendered moot the level of transverse steel; indeed, PS3, with one-third the transverse reinforcement ratio of PS1, virtually duplicated PS1's performance up to the limit of travel of the test rig ($\mu=6$). In the absence of external confinement, the influence of varied transverse reinforcement was more clearly seen, with PS6 failing at $\mu=3$, PS5 failing at $\mu=5$, and PS4 reaching $\mu=6$. (The loading of PS2, in which the fixturing about the plastic hinge was omitted, paralleled that of PS5; PS2 failed slightly earlier. PS7 and PS8, in the current series of tests, were loaded in the same manner as was PS2.)

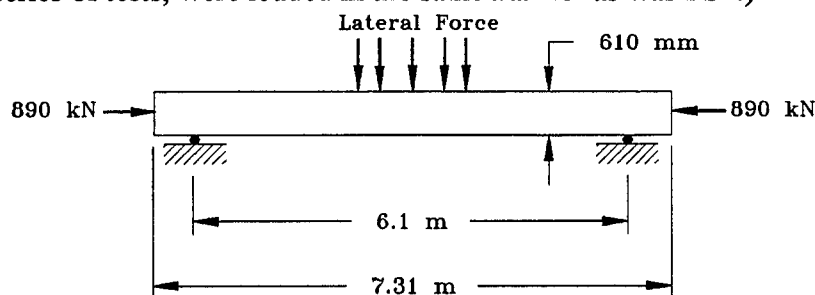


Fig. 2.6: Cast-in-place pile test configuration by Budek, Benzoni, and Priestley (drawn to scale; PS2 omitted the center later load point)

Shown in fig. 2.7 are test loadings and spans, among the past work present tests.

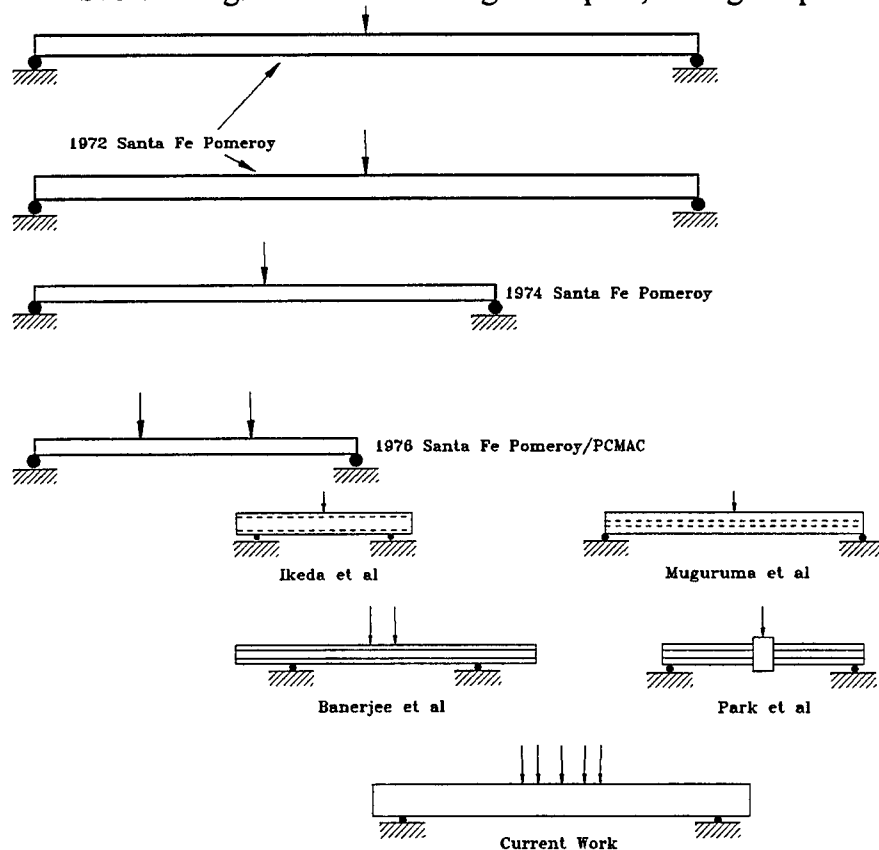


Fig. 2.7: Comparison of geometry and loading of previous pile body tests with present work; the cast-in-place pile shaft tests of Budek, Benzoni, and Priestley used the same test configuration as the present work)

3. EXPERIMENTAL APPARATUS AND PILE SHAFT TEST UNITS

3.1 Experimental Apparatus

The test apparatus was designed to load the test units in a way that would as closely as possible simulate the moment pattern produced by the lateral pressure of soil on a pile shaft. Basically a whiffle tree, the loading mechanism distributed the applied force from three (two, in the cases of PS7, PS8, PS12, PS13, and PS16) 980 kN MTS actuators through five (four for PS7, PS8, PS12, PS13, and PS16) symmetrically arrayed load points. Shown in fig. 3.1 is the general configuration used for this series of tests.

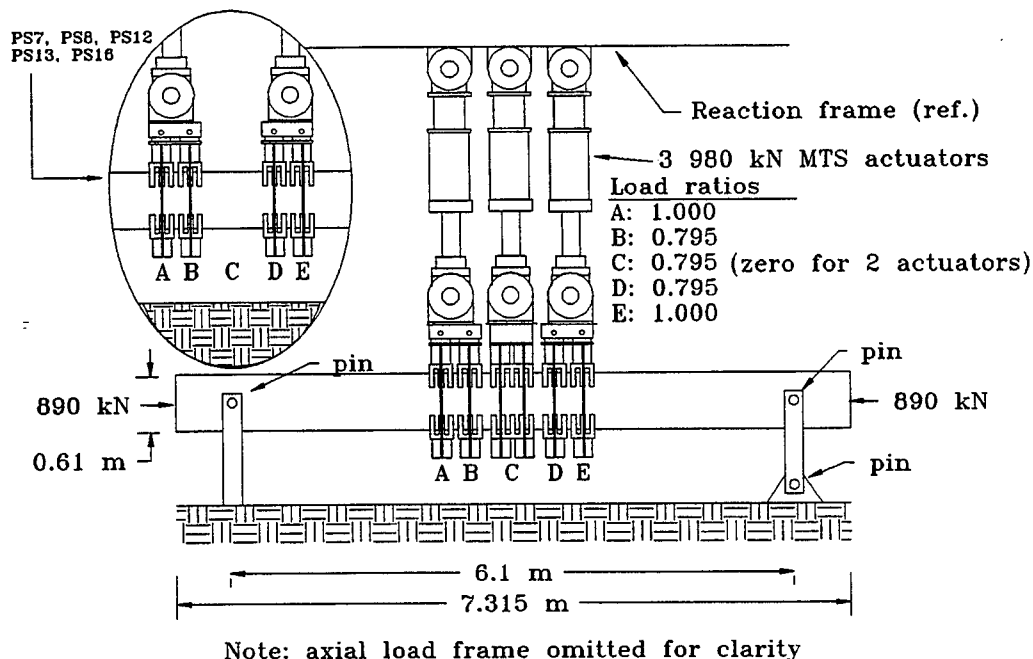


Fig. 3.1: General arrangement of test apparatus used for PS7-16 (scrap views: for PS7, PS8, PS12, PS13, and PS16 the center actuator was removed, and load ratio C was thus zero)

Fig. 3.2 is a photograph of the test rig, in the three-actuator configuration used for PS9, PS10, PS11, PS14, and PS15. Note the bars carrying the axial load running horizontally across the picture, parallel to the pile shaft.

As mentioned above, the piles were loaded through a series of saddles which covered 100° of the shaft circumference, top and bottom (fig. 3.3). The saddles were lined with pads, 25.4 mm thick, of 70 Duro 'A' rubber, to simulate soil with a subgrade reaction modulus of 25600 kN/m³. The top and bottom saddles were tied together with threaded rod; adjustments were made to ensure that the saddles would fit lightly against the surface of the test unit, and did not in themselves apply a compressive force. PS9, PS10, PS11, PS14, and PS15 utilized three actuators (fig. 3.1). Two actuators were used

for PS7, PS8, PS12, PS13, and PS16 (previous experience with cast-in-place pile shaft test units PS1 through PS3 indicated that external confinement of the plastic hinge region played a very significant role in the structure's response). The center actuator was omitted in the specified tests to leave a gap of 610 mm (1D) in this external confinement (the resulting moment pattern was virtually unchanged).

An axial load of 890 kN was maintained during the tests to give a nominal $P_{ax}=0.074f_cA_g$ for the solid piles ($0.12f_cA_g$ for the hollow piles, PS11-14) Axial load was applied by strongbacks at either end of the test units, connected by high strength steel rods running down either side (fig. 3.4). Load was applied via hollow-core jacks, and monitored by load cells. The strongbacks were kept level through the tests by a manually-controlled system of jacks (fig. 3.5). A significant P- Δ effect was expected as the solid piles were able to reach maximum midpoint displacements of about 200 mm (@10% drift).



Fig. 3.2: Pile shaft test rig, three-actuator configuration



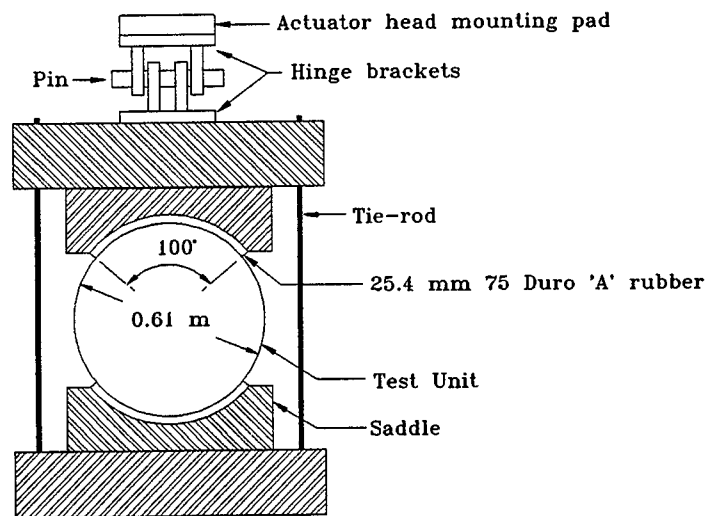


Fig. 3.3: Cross-section of loading apparatus used for pile shaft test units PS7-PS16

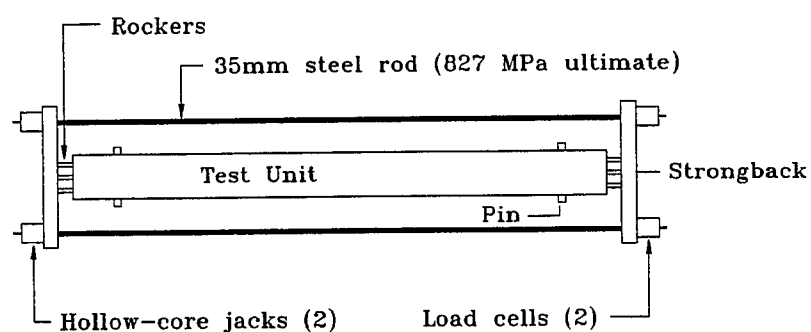


Fig. 3.4: Axial load mechanism - top view

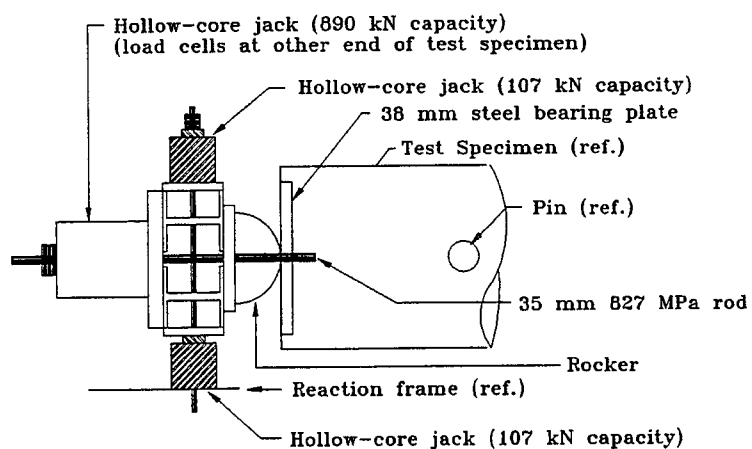


Fig. 3.5: Side view of axial load strongback and leveling mechanism

3.2 Solid Pile Shaft Test Units PS7 - PS10

The test units were circular-section pile shafts of 610 mm diameter, with a nominal 76 mm cover to the tendons (fig. 3.6). Actual cover thickness to the tendons averaged 86 mm. Transverse reinforcement details are given in table 1.1. The test piles were 6.1 m between pins, and 7.315 m long overall. Moment-curvature data for the sections are shown in fig. 3.7. Ultimate theoretical capacity was determined by a simplified expression of the Mander model for the ultimate allowable strain of confined concrete^[16]:

$$\epsilon_{cc} = 0.004 + \frac{1.4\rho_s f_{yh} \epsilon_{su}}{f'_{cc}} \quad (3.1)$$

in which ρ_s is the volumetric reinforcement ratio, f_{yh} is the yield stress of the transverse reinforcement, ϵ_{su} is the steel strain at its maximum tensile stress (assumed to be 0.11 for the A82 spiral used in these tests), and f'_{cc} is the confined concrete strength (assumed to be 1.5 times f'_c). Table 3.1 gives concrete and steel physical properties, and fig. 3.7 displays moment-curvature properties for the sections.

PS7 - PS10 were cast on November 17, 1995. Concrete strength at transfer (i.e., cutting of the tendons at the pile ends) was 27.7 MPa.

Shown in figs. 3.8 and 3.9 are steps in the construction of the test piles. The casting beds were steel forms, bolted to a concrete base. The basic forms (which were symmetrical about their long axis and could thus run two sets of tendons) gave the 'bottom' half of the section. Clamshell doors closed over the top of the form (leaving a gap through which concrete could be cast) to give the complete circular section. Stressing bulkheads (drilled with the appropriate tendon pattern) were placed at each end of the assembled forms; the tensioning jack, and the fixed ends of the tendons, reacted against these. Into the forms were first placed movable steel bulkheads (called 'cookies'), drilled for the tendon pattern, which delineated the pile ends (i.e., for a pile of overall length 7.315 m the cookies would be placed that distance apart). In the actual construction of the piles, spiral steel was first placed into the forms, and the tendons then run through one bulkhead, through the first cookie, through the spiral steel, through the second cookie, and out through the terminal bulkhead, where they were secured with chocks (PS7-10 were built two-to-a-side in the forms, so an additional cookie and set of spiral steel was incorporated into the above procedure). The tendons were then given an initial pull of 9 kN, and the spiral stretched out into the proper pitch. The tendons were then given a final pull to bring them up to their desired level of stress, and the spiral tied in place. The forms and doors were oiled, and the doors were then closed over the cages, bolted down, and the concrete cast through the top opening (fig. 3.9). Vibration was by hand-held 'stinger' vibrators and a pneumatic 'vibra-track', a very powerful vibrator that was pulled along tracks running down either side of the form. (The foregoing description is a generic work-flow for precast-prestressed pile construction; instrumentation and

fixturing, such as the vertical tubes seen in fig. 3.88, which carried the mounting-pins for the test rig, peculiar to these piles were added at appropriate points in the construction process.)

TABLE 3.1: PRESTRESSED PILE SHAFT TEST UNIT PS7-10 MATERIAL PROPERTIES

Test Unit	f_c (MPa)	transverse steel strength	
		f_{yt} (MPa)	f_u (MPa)
PS7	47.1	482	551
PS8	53.4	482	551
PS9	49.9	482	551
PS10	49.3	654	723

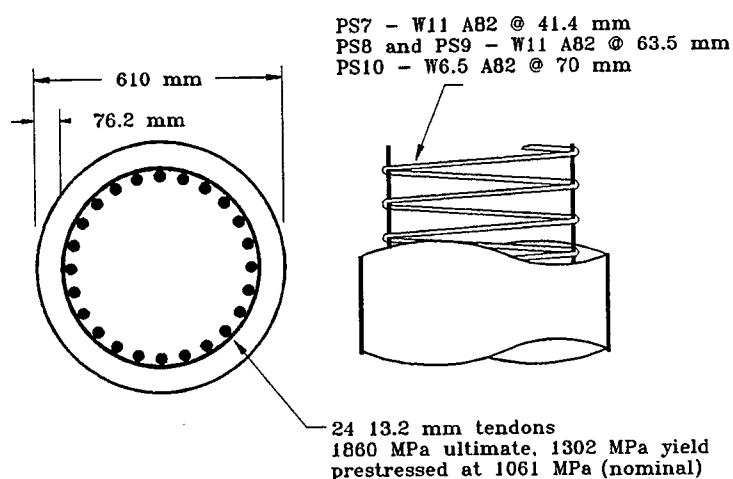


Fig. 3.6: Dimensional and reinforcement details of pile shaft test units PS7 - PS10

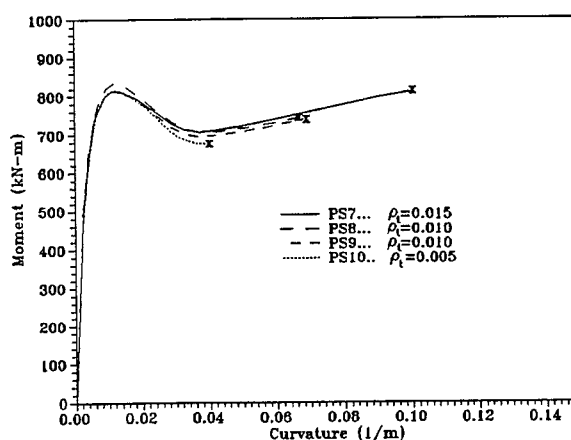


Fig. 3.7: Theoretical moment-curvature data for pile shaft test units PS7 - PS10, using actual material properties

The prestressing tendons could not be tested because of equipment limitations. Their nominal properties were

ultimate strength f_{pu}	=	1860 MPa
yield strength f_{py}	=	1302 MPa
diameter		13.2 mm
area		106 mm ²

Theoretical shear strength of a circular section is given by [16]

$$V_d = V_c + V_s + V_p \quad (3.2)$$

in which equation V_c is the concrete shear-resisting mechanism, V_s is provided by the steel truss mechanism, and V_p is an enhancement from axial load forming a diagonal compression strut:

$$V_c = 0.29\sqrt{f'_c}A_e \text{ for } \mu_\Delta \leq 2 \text{ (MPa units)}$$

$$V_c = 0.10\sqrt{f'_c}A_e \text{ for } \mu_\Delta \geq 4 \text{ (MPa units)}$$

$$V_c = 0.05\sqrt{f'_c}A_e \text{ for } \mu_\Delta \geq 8 \text{ (MPa units)}$$

$$V_s = \frac{\pi A_h f_{yh} (D - c - x)}{2s} \cot \theta \quad (\theta = 30^\circ)$$

$$V_p = P_{axial} \tan \alpha \quad (\alpha = 5^\circ)$$

in which

f'_c = confined concrete strength

$A_e = 0.8A_{gross}$

A_h = area of transverse bar

f_{yh} = yield strength of transverse bar

D = diameter

s = spiral pitch

θ = angle of shear cracks to column axis

α = angle between column axis and strut

c = cover to spiral

x = neutral axis depth



Fig. 3.8: Prestressed piles in casting beds, prior to cast

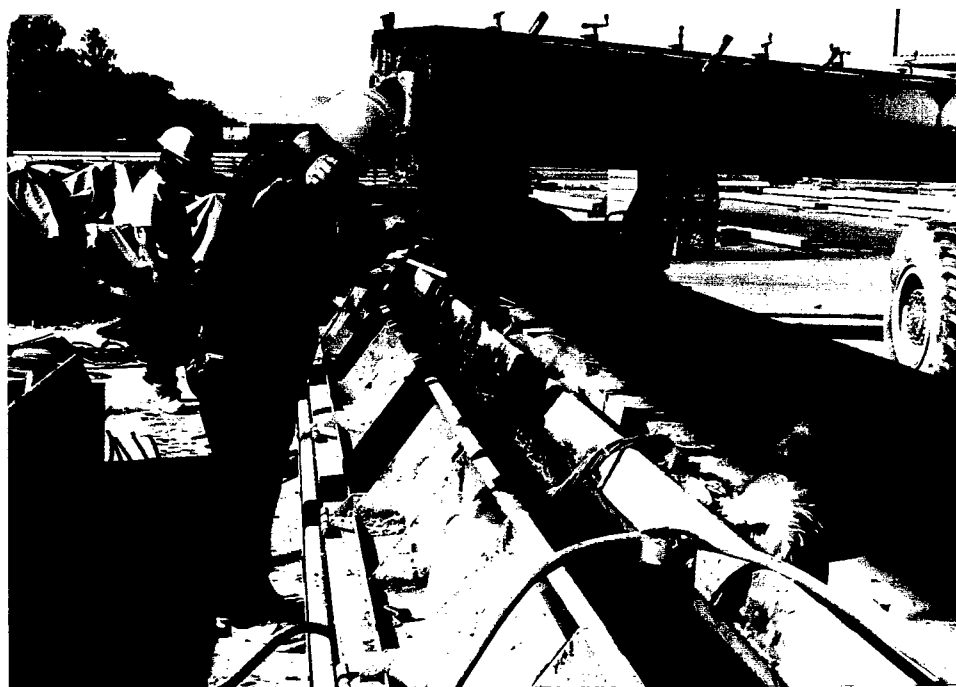


Fig. 3.9: Prestressed piles being cast



Table 3.2 gives the theoretical shear strengths of each test unit; a linear interpolation is used between $\mu=2$ and $\mu=4$, and between $\mu=4$ and $\mu=8$.

TABLE 3.2: PRESTRESSED PILE SHAFT TEST UNIT PS7-10 THEORETICAL SHEAR STRENGTH

Test Unit	Shear strength $\mu_{\Delta} \leq 2$	Shear strength $\mu_{\Delta} \geq 4$	Shear strength $\mu_{\Delta} \geq 8$	Maximum shear experienced
PS7	1149 kN	800 kN	682 kN	373 kN
PS8	1045 kN	692 kN	582 kN	339 kN
PS9	1028 kN	686 kN	579 kN	340 kN
PS10	955 kN	621 kN	522 kN	338 kN

Fig. 3.10 shows a comparison of experimentally observed shear vs. theoretical shear capacity for PS10 (in which the theoretical and response envelopes would have been closest). Clearly shear was not expected to be critical for these piles.

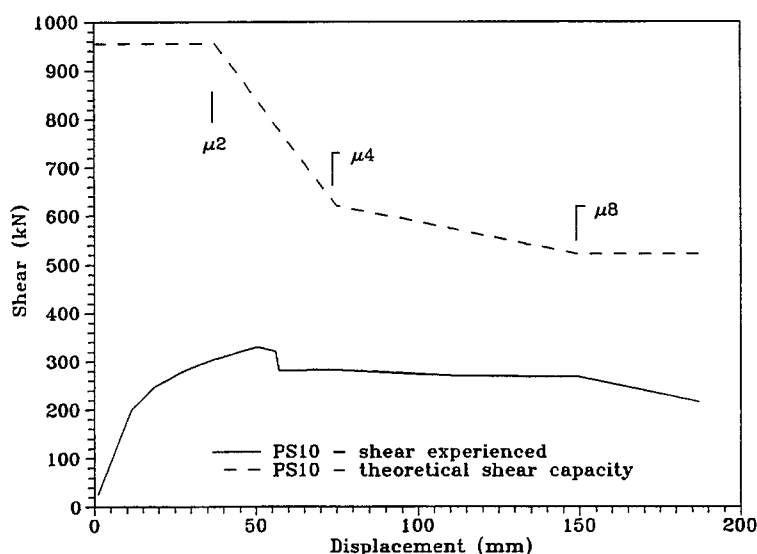


Fig. 3.10: Comparison of theoretical shear capacity with experimentally observed shear, pile shaft test unit PS10

3.3 Hollow Piles PS11 - PS14

The test units were circular-section prestressed piles of 0.6096 m diameter, with 41 mm cover to the spiral steel, and a core diameter of 0.422 m, giving a shell thickness of 94 mm. Prestressing steel consisted of 16 7-wire tendons ($f_{pu}=1860$ MPa nominal) for all piles; in the case of PS11 and PS14, 11.1 mm diameter tendons was used, stressed at 1061 MPa (after losses). Because of a shortage of stressing chucks, and a need to

clear the stressing beds in timely fashion, 12.7 mm tendons had to be used for PS12 and PS13; 16 tendons were used, stressed at 744 MPa (after losses), to give the same effective section prestress. This substitution was judged acceptable because the expected failure mode was crushing of the core concrete; the tendons were not expected to come anywhere near their ultimate capacity in strain or stress. Transverse reinforcement was varied through the series; PS11 had a nominal transverse reinforcement ratio of 0.03; PS12 and PS13, 0.02; and PS14, 0.01 (sections are shown in figs. 3.11 and 3.12). Concrete and steel physical properties appear in table 3.3, and theoretical moment-curvature data is shown in fig. 3.13. (the extra flexural steel area provided by the tendons in PS12 and PS13 increased the predicted and actual flexural strength of those test units).

PS13 differed from PS12 in having eight #4 Grade 60 bars (D12.5, 455 MPa nominal) running through the plastic hinge region.

Construction of the hollow piles was similar to the procedure described above, but for the inclusion of the void within the pile. The void was created by placing a sealed length (3.35 m long, centered on the pile's longitudinal centerline) of Sonovoid™ inside the cage of tendons and spiral in the casting form. The Sonovoid™ was blocked against the stressed tendons, and was additionally braced to the doors of the form, to prevent float. The Sonovoid™ could not, of course, be removed after casting, and so the void was filled with water through provided vents, so that the unprotected inner cardboard surface would be softened and thus provide negligible confinement to the core concrete. Samples placed in water indicated that soaked Sonovoid™ delaminates, and has virtually no residual strength.

Hollow pile test units PS11 - PS14 were cast on July 23, 1996. Concrete strength at transfer (i.e., cutting of the tendons at the pile ends) was 40.9 MPa. The prestressing tendons could not be tested because of equipment limitations. Their nominal properties are:

f_y	1585 MPa
f_u	1860 MPa
diameter	11.1 mm (PS11, PS14)
	12.5 mm (PS12, PS13)
area	71 mm ² (PS11, PS14)
	99 mm ² (PS12, PS13)

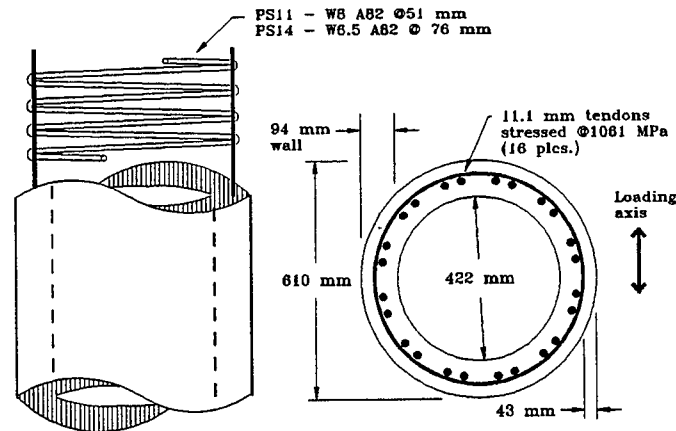


Fig. 3.11: Dimensional and reinforcement details of pile shaft test units PS11 and PS14

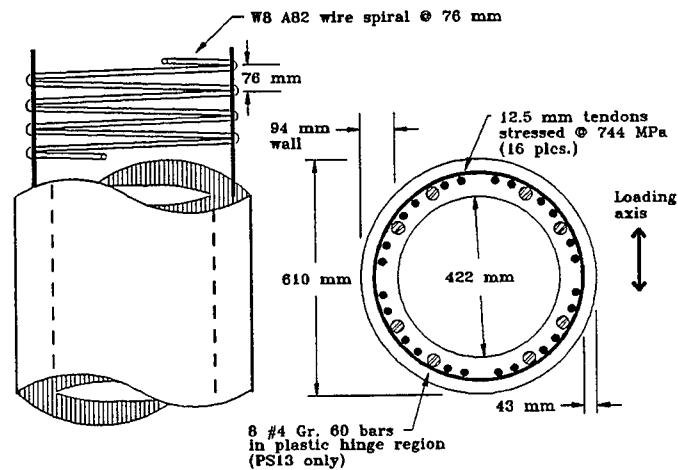


Fig. 3.12: Dimensional and reinforcement details of pile shaft test units PS12 and PS13

TABLE 3.3: HOLLOW PRESTRESSED PILE SHAFT TEST UNIT PS11-14 MATERIAL PROPERTIES

Test Unit	f'_c (MPa)	transverse steel strength	
		f_{yt} (MPa)	f_u (MPa)
PS11	67.0	647	816
PS12	67.8	647	816
PS13	67.7	647	816
PS14	53.5	664	760

The concrete strength of PS14 would seem to be anomalously low, and probably represents a sampling artifact.



The concrete strength of PS14 would seem to be anomalously low, and probably represents a sampling artifact.

Theoretical shear capacity for the hollow piles tested is given in table 3.4, and the theoretical and measured shear envelopes for PS12 are shown in fig. 3.15.

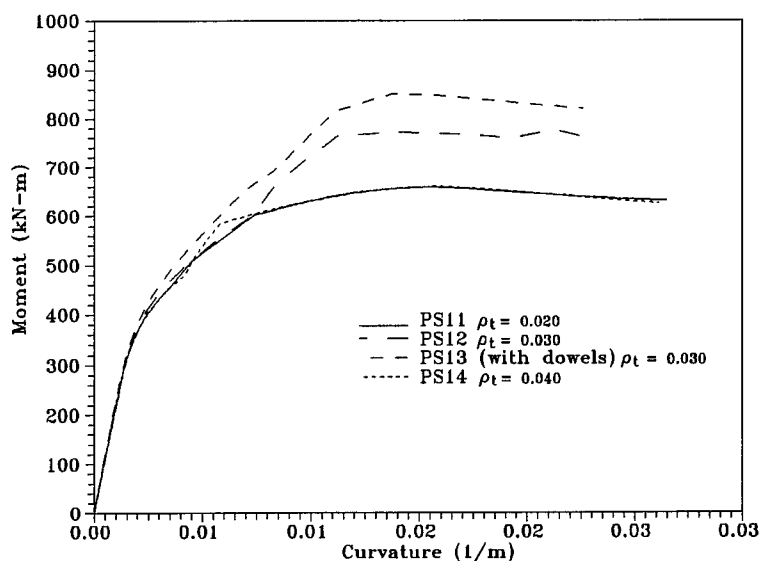


Fig. 3.13: Theoretical moment-curvature data for pile shaft test units PS11 - PS14, using actual material properties (axial load of 890 kN)

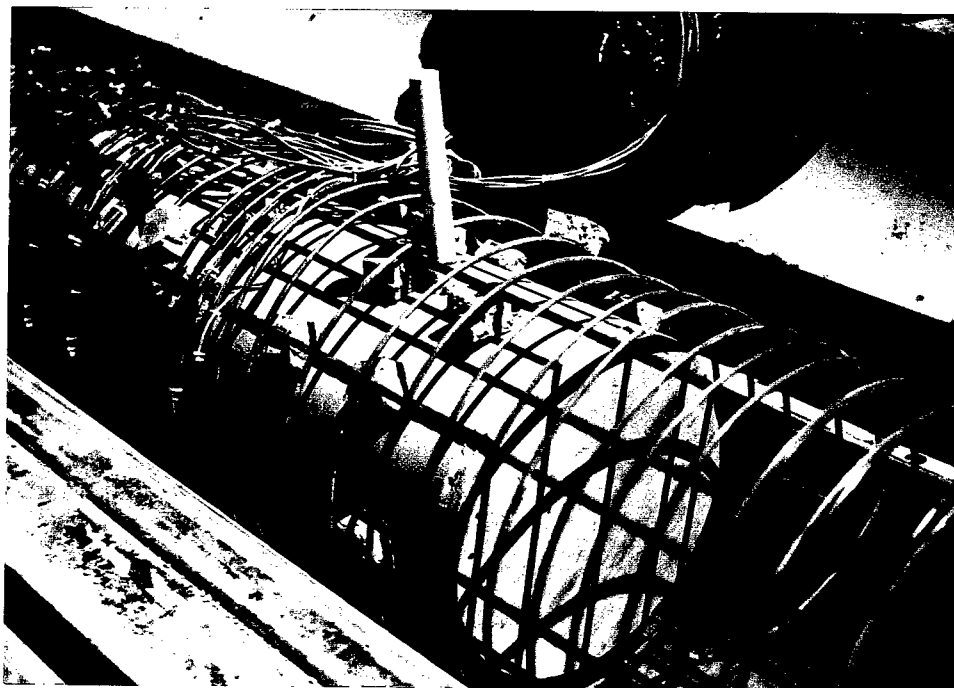


Fig. 3.14: Hollow prestressed pile in casting bed, prior to cast. Note Sonovoid™ used to form void.



**TABLE 3.4: HOLLOW PRESTRESSED PILE SHAFT TEST UNIT PS11-14
THEORETICAL SHEAR STRENGTH**

Test Unit	Shear strength $\mu_{\Delta} \leq 2$	Shear strength $\mu_{\Delta} \geq 4$	Maximum shear experienced
PS11	637 kN	447 kN	251 kN
PS12	622 kN	431 kN	329 kN
PS13	676 kN	485 kN	312 kN
PS14	595 kN	425 kN	245 kN

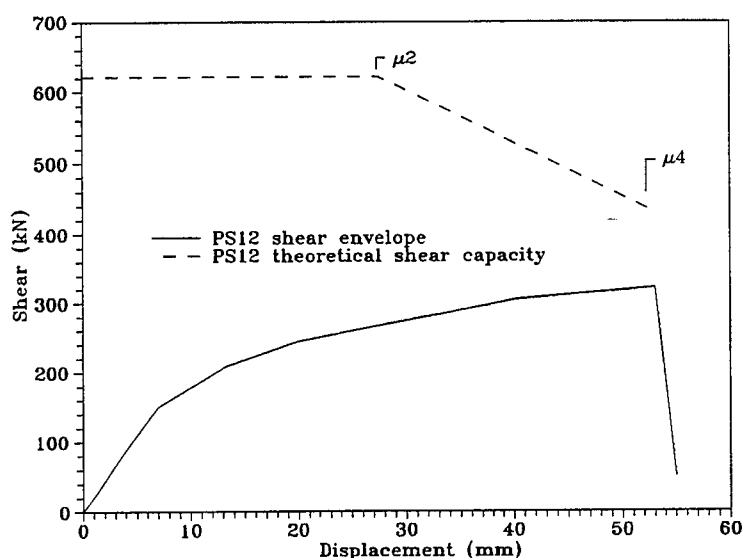


Fig. 3.15 Comparison of theoretical shear capacity with experimentally observed shear,
hollow pile PS12

3.4 Solid Prestressed Piles with Glassfibre Jackets

The test units were circular-section prestressed piles, similar in transverse reinforcement levels to PS10 (see section 3.1 above) of 0.6096 m diameter, with 76.2 mm cover to the tendons (fig. 3.16). Transverse reinforcement was W6.5 A82 grade (D9.5, 565 MPa nominal) spiral pitched at 55.9 mm, resulting in $\rho_t=0.005$. The unit was 6.096 m between pins, and 7.315 m overall. Theoretical moment-curvature data for this section (both jacketed - PS15 and PS16; and unjacketed - PS10) is shown in fig. 3.17.

The piles were cast on December 30, 1996. Concrete strength at transfer (i.e., cutting of the tendons at the pile ends) was 27.6 MPa. The prestressing tendons could not be tested because of equipment limitations.

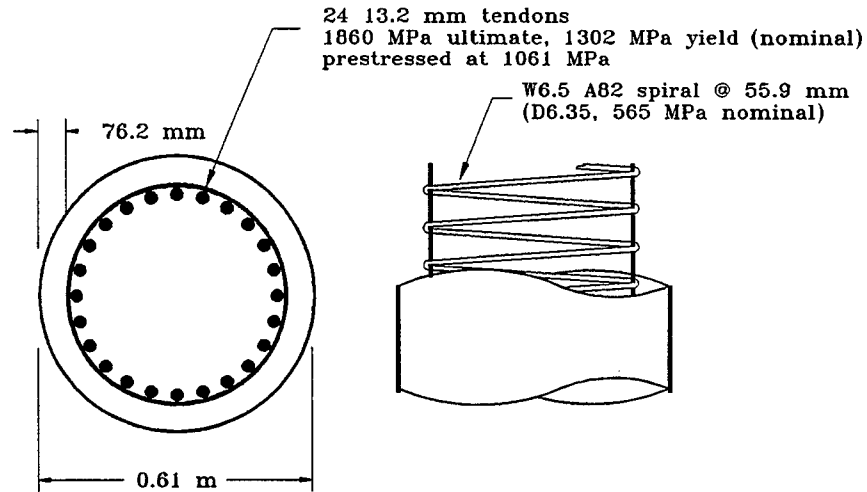


Fig. 3.16: Dimensional and reinforcement details of pile shaft test units PS15 and PS16

TABLE 3.5: GLASSFIBRE-JACKETED SOLID PRESTRESSED PILE SHAFT
TEST UNIT PS15-16 MATERIAL PROPERTIES

Test Unit	f'_c MPa	jacket strength (main fibre orientation)			jacket strength (90° off main fibre orientation)			transverse steel strength	
		f'_{uj}	ϵ_{uj}	E_j	f'_{uj}	ϵ_{uj}	E_j	f_{yt} (MPa)	f_u (MPa)
PS15	67.0	384 MPa	1.9%	23.1 GPa	---	---	---	664	760
PS16	67.8	442 MPa	1.8%	24.6 GP	46.1 MPa	0.612%	8.04 GPa	664	760

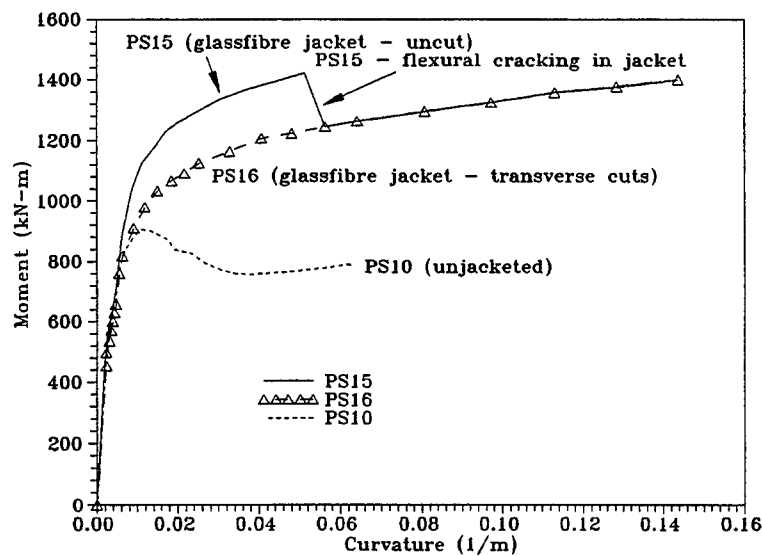


Fig. 3.17: Theoretical moment-curvature data for pile shaft test units PS15 and PS16, using actual material properties (axial load of 890 kN); PS10 (unjacketed) included for reference

Jacket design was done by considering the test unit at a midpoint deflection of 180 mm (PS10, with similar transverse reinforcement, and tested with external confinement, had failed at a displacement of 187 mm). The total rotation at this point would thus be

$$\Theta = \frac{\Delta}{L} = \frac{180\text{mm}}{3.05\text{m}} = 0.059$$

The measured plastic hinge length for PS10 was 0.903 pile diameters, in which case the curvature is

$$\phi = \frac{\Theta}{l_p} = \frac{0.059}{0.903 \times 0.61\text{m}} = 0.107/m$$

The maximum concrete compression strain may thus be found, using a neutral axis depth of 0.2 m^[16]

$$\epsilon_{cu} = (0.107/m)(0.2\text{m}) = 0.0214 = 0.004 + \frac{2.5\rho_s f_{uj} \epsilon_{uj}}{f'_{cc}}$$

in which are taken the design values for ultimate jacket stress as $f_{uj}=448$ MPa, ultimate jacket strain as $\epsilon_{uj}=0.02$, and $f'_{cc}=62$ MPa. Given that somewhat more compression strain might successfully be borne by the pile in the jacketed case, an ultimate value of concrete compression strain $\epsilon_{cu}=0.026$ was chosen for design. From the above equation, and the definition of the effective volumetric ration for a circular jacket retrofit

$$\rho_s = \frac{4t_j}{D}$$

in which t_j is the jacket thickness and D the section diameter, the required jacket thickness may be found

$$t_j = \frac{0.1(\epsilon_{cu} - 0.004)Df'_{cc}}{f_{uj}\epsilon_{uj}} = \frac{0.1 \times (0.026 - 0.004) \times 62\text{MPa} \times 0.61\text{m}}{448\text{MPa} \times 0.02} = 9.3\text{mm}$$

Seven wraps of unidirectional glass (1.27mm/wrap) were applied for a total jacket thickness of 9.1 mm.

PS15 and PS16 received their glassfibre jackets on July 31, 1997. The jackets were supplied and installed by Hexcell/Fyfe, of San Diego, California. They consisted of seven plies of the TYFO™ SEH-51 composite system, using TYFO™ S epoxy and

unidirectional E-glass. The main fibers of the E-glass were laid in the transverse direction, as the intention was to provide transverse reinforcement only; additional longitudinal reinforcement was not desired, nor was it desirable. Kevlar™ fibers were used as cross-links in the E-glass uni cloth. Two wraps were used, as per fig. 3.18; the joint was at the center of the pile. This was not expected to have significance, as, again, longitudinal reinforcement was not sought. However, testing of PS15 indicated that the jacket was providing some degree of longitudinal reinforcement which may have degraded the overall performance of the test unit. Therefore, circumferential cuts were made through the jacket of PS16 every 152 mm over a length of 912 mm (centered on the longitudinal midpoint), to force the jacket to provide pure hoop reinforcement in the plastic hinge region (fig. 3.19). Application of the glassfibre wraps is shown in fig. 3.20.

PS15 was tested with three actuators, and full complement of load saddles; PS16 used two actuators, leaving the center of the plastic hinge region without external confinement from the fixtures.

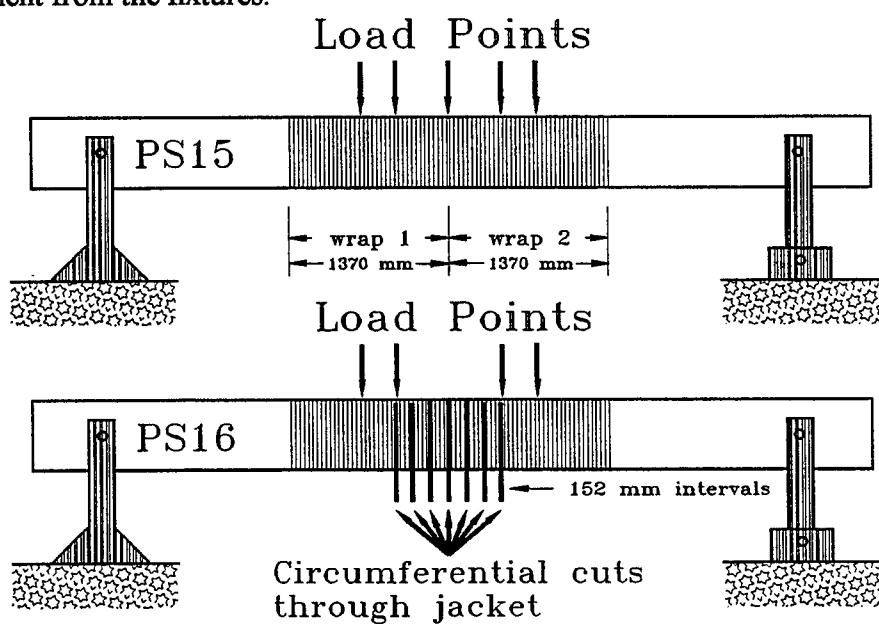


Fig. 3.18: Glassfibre wraps applied to prestressed pile shaft test units PS15 and PS16



Fig. 3.19: Application of glassfibre wrap to pile shaft test unit PS15

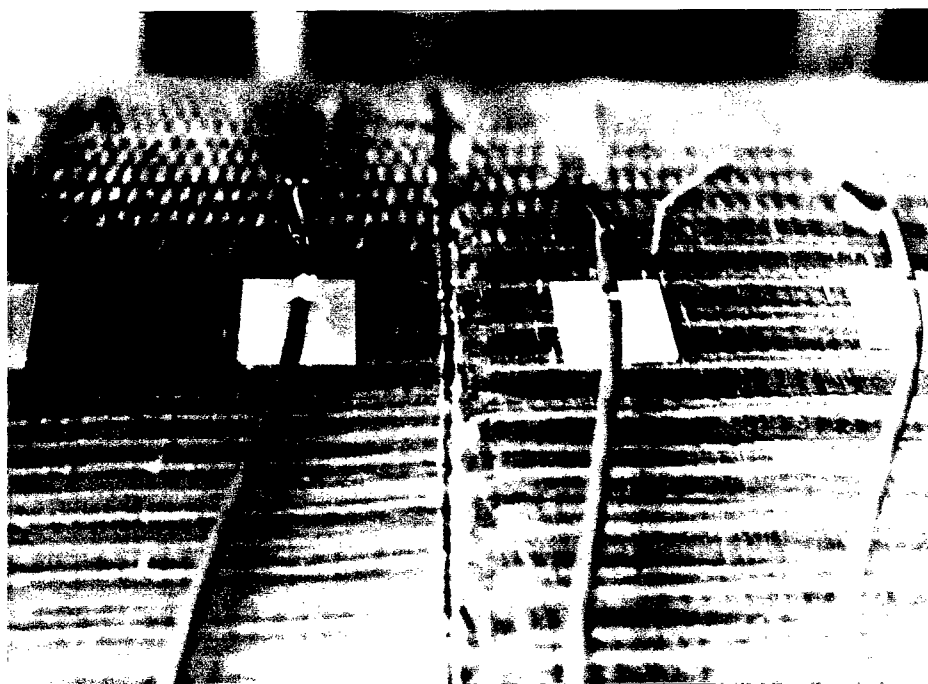


Fig. 3.20: Transverse cut through jacket of PS16



The contribution of the glassfibre jacket to the section shear strength is attained by analogy to the reinforcing steel

$$V_j = \frac{\pi}{2} t_j f_{yj} (D - h) \cot \Theta$$

in which t_j is the jacket thickness, $\Theta=30^\circ$, D is the section diameter, and h is the distance to the neutral axis. The jacket yield stress, f_{yj} is taken as the stress at a strain of 0.4%; using the ultimate stress of the jacket would imply strain dilations on a level that would not be sustainable by the aggregate interlock shear mechanism. The jacket yield stress is thus computed as

$$f_{yj} = 0.004 E_j$$

Table 3.6 gives theoretical shear strength for PS15 and PS16, and fig. 3.21 compares the theoretical shear envelope with shear actually experienced.

TABLE 3.6: GLASSFIBRE-JACKETED PRESTRESSED PILE SHAFT TEST UNIT PS7-10 THEORETICAL SHEAR STRENGTH

Test Unit	Shear strength $\mu_{\Delta} \leq 2$	Shear strength $\mu_{\Delta} \geq 4$	Shear strength $\mu_{\Delta} \geq 8$	Maximum shear experienced
PS15	1322 kN	881 kN	784 kN	440 kN
PS16	1346 kN	904 kN	806 kN	421 kN

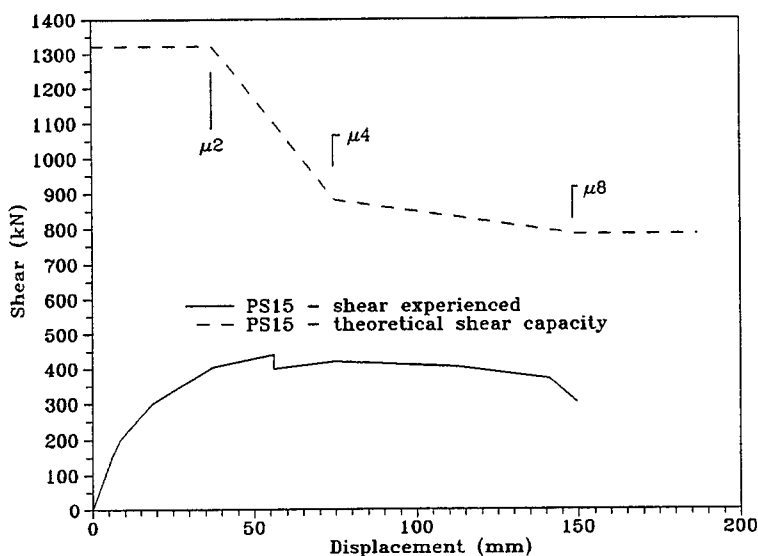


Fig. 3.21: Comparison of theoretical shear capacity with experimentally observed shear, glassfibre-jacketed solid prestressed pile PS15

4. EXPERIMENTAL PROCEDURE

4.1 Loading schedule, solid prestressed piles PS7 - PS10

The actuators were initially zeroed to compensate for the self-weight of the test units, and the dead load of the loading apparatus.

The test units were initially cycled at low loads, at 50 kN intervals from 50 to 200 kN. (Forces given are half-loads of the sum of the actuator forces, and thus correspond to maximum shear force, or end reaction.)

Displacement at ductility $\mu=1$ was then defined as

$$\mu_1 = \Delta_{200kN} \frac{M_{ideal}}{M_{200kN}} = 18.7 \text{ mm}$$

in which first-yield and ideal moments were obtained by through moment-curvature analysis using the Mander model for confined concrete. Similar displacements corresponding to the above value for $\mu=1$ were used for all four tests, to provide a level basis for comparison.

Loading was then continued as follows (test unit failure levels included):

- (6) 3 cycles at $\mu=1$
- (7) 3 cycles at $\mu=1.5$
- (8) 3 cycles at $\mu=2$
- (9) 3 cycles at $\mu=3$
- (10) 3 cycles at $\mu=4$
- (11) 3 cycles at $\mu=6$ (PS8 halted)
- (12) 3 cycles at $\mu=8$ (PS9 halted; PS7 two cycles)
- (13) 1 cycle at $\mu=10$ (PS10 only)

Testing of PS8 was halted before failure at $\mu=6$ for reasons of safety; tests done by previous researchers indicated the possibility of a sudden and brittle failure. As the axial load system used in this series of tests had to be manually controlled to remain stable, a brittle failure of the pile might not at all have been a good thing to experience. Subsequent review of the data, and the overall behavior of the test unit, obviated the need for this degree of caution, and two of the tests (PS7 and PS10) were carried to failure of the pile.

TABLE 4.1: ULTIMATE DUCTILITIES ACHIEVED, PS7-10

Test Unit	Method of Loading	ρ_t	$\mu_{\Delta, ultimate}$
PS7	plastic hinge unconfined	0.0151	8 (failed)
PS8	plastic hinge unconfined	0.0098	6 (incipient failure)
PS9	plastic hinge confined	0.0098	8 (no failure)
PS10	plastic hinge confined	0.0054	10 (failed)

4.2 Loading schedule, hollow prestressed piles PS11 - PS14

The actuators were initially zeroed to compensate for the self-weight of the test unit, and the weight of the test hardware which bore upon the column (i.e., that shown in fig. 6). The following loading program was then followed. Forces given are half-loads of the sum of the actuator forces.

- (1) +/- 30 kN, 1 cycle
- (2) +/- 60 kN, 1 cycle
- (3) +/- 90 kN, 1 cycle
- (4) +/- 120 kN, 1 cycle
- (5) +/- 150 kN, 1 cycle

In the case of PS11, PS12, and PS14, displacement at ductility $\mu=1$ was defined from predictive analysis as

$$\Delta_{0.75 \text{ ideal moment}} \times M_{\text{ideal}} / M_{0.75 \text{ ideal}} = 13.4 \text{ mm}$$

in which the moments specified were obtained by through moment-curvature analysis using the Mander model for confined concrete.

Loading was then continued as follows:

- 3 cycles at $\mu=1$
- 3 cycles at $\mu=1.5$
- 3 cycles at $\mu=2$
- 3 cycles at $\mu=2.5$ (PS14 only)
- 3 cycles at $\mu=3$
- 1 cycle at $\mu=4$ (one-half cycle for PS12 and PS14)

In the case of PS13, the addition of nonprestressed longitudinal reinforcement raised the yield displacement, and thus the displacement at $\mu=1$. The midpoint displacement used to define $\mu=1$ was thus 20.2 mm, with loading as follows:

3 cycles at $\mu=1$
 3 cycles at $\mu=1.5$
 3 cycles at $\mu=2$
 1 cycle at $\mu=2.5$

TABLE 4.2: ULTIMATE DUCTILITIES ACHIEVED, PS11-14

Test Unit	Method of Loading	ρ_t	$\mu_{\Delta, \text{ultimate}}$
PS11	plastic hinge confined	0.0297	4 (1 cycle)
PS12	plastic hinge unconfined	0.0194	4 (one-half cycle)
PS13	plastic hinge unconfined	0.0194	2.5 (1 cycle)
PS14	plastic hinge confined	0.0117	4 (one-half cycle)

4.3 Loading Schedule, Glassfibre-Jacketed Piles

Since PS15 and PS16 were nominally identical to PS10 in terms of their prestressing and transverse reinforcement, they were intended to follow the same loading schedule in terms of loads and displacement levels described in sec. 4.1 above. Because of an instability in the test rig that developed during the testing of PS16, however, PS16 could not be tested in push at $\mu=6$ or above; at this level of ductility and above, therefore, push excursions were limited to $\mu=3$. The inelastic testing of PS15 and PS16 was therefore performed as follows:

3 cycles at $\mu=1$
 3 cycles at $\mu=1.5$
 3 cycles at $\mu=2$
 3 cycles at $\mu=3$
 3 cycles at $\mu=4$
 3 cycles at $\mu=6$ (PS16 pull only)
 3 cycles at $\mu=8$ (PS15 1 cycle; PS16 pull only)

TABLE 4.3: ULTIMATE DUCTILITIES ACHIEVED, PS15-16

Test Unit	Method of Loading	ρ_t	$\mu_{\Delta, \text{ultimate}}$
PS15	plastic hinge confined	0.0054	8 (1 full cycle)
PS16	plastic hinge unconfined transverse cuts in jacket	0.0054	8 (3 pull cycles)

4.4 Instrumentation

Instrumentation on the spiral steel was similar for all of the prestressed piles. Strain gauges were placed on transverse steel through the loading area. In fig. 4.1 are shown the nominal positions of the transverse gauges. Foil resistance strain gauges of 5mm gauge length were used, bonded to cleaned and polished steel with cyanoacrylate adhesive, waterproofed, and protected against mechanical insult by mastic. Nominal locations are shown below; actual locations were dictated by configuration of the reinforcing steel cage.

Strains in the glassfibre jackets of PS15 and PS16 were measured using 60 mm foil resistance strain gauges, bonded to the roughened surface of the glassfibre with 2-part epoxy. Their spacing on the top and bottom (12 o'clock and 6 o'clock) of PS15 was dictated by the position of the 'teeth' of the load saddles; there were four gauges at 100 mm intervals. The gauges at 3 o'clock and 9 o'clock were similarly placed for consistency. In the case of PS16, six gauges were placed top and bottom, spaced at 76 mm. Four gauges were placed at 3 and 9 o'clock.

Instrumentation used to measure curvature consisted of sets of linear displacement transducers (± 19 mm travel), paired in vertical planes; the relative difference in their displacements was used to calculate section curvature. Curvature was measured through the loading area over a length similar to that instrumented with strain gauges. The transducers were mounted on aluminum angle brackets, which were in turn attached to steel thread rod cast into the test unit. In the case of PS7 - PS10, the loading system dictated the mounting of the curvature instrumentation along both sides of the test units (fig. 4.2); the results were averaged to eliminate errors caused by lateral 'sway' during test. The thread rod holding the bracketry was installed such that the rod on the compression side of each cycle would be in the forecast compression zone. The spacing of the curvature mounting rods was slightly altered for PS16, so that the 'bands' left after the transverse cuts were made in the glassfibre jacket were left as intact as possible.

Additionally, overall displacement of the test units was measured via displacement transducers at the longitudinal midpoint (± 228.6 mm travel), the end supports (± 19 mm travel), and the quarter-points (midway between support and midpoint) (± 152.4 mm travel).

5. RESULTS - SOLID PRESTRESSED PILES

5.1 PS7

Gross examination of PS7 during and after the test showed that plasticity was evident over a fairly wide area ($\approx 1D$), centered on the test unit's longitudinal midpoint. Incipient crushing began here at $\mu=2$, and spalling took place suddenly just prior to the completion of the first excursion to $\mu=3$, leading to a sudden, significant loss in load-carrying capacity. Spalling continued (and eventually spread about nearly the entire circumference of the pile) as the test unit was cycled through $\mu=6$, with relatively little loss (apart from $p-\Delta$ degradation) of strength. The first 'push' cycle at $\mu=8$ also maintained the previous level of strength, but on the way to the first pull at this level of ductility, two spirals fractured (note the 'notch' on fig. 5.1.3), and thereafter loss of strength was rapid.

Very few cracks were seen or expected, because of the high degree of prestressing in the section. Flexural cracks were seen up to 1.8 m from the longitudinal midpoint of the test unit, indicating a significant degree of curvature to that point.

As mentioned above, two spirals fractured on the way to $\mu=8$ (pull). At least two more had yielded, with necking seen in one of these. No individual strands within prestressing tendons were seen to have broken.

The force-deflection loops are shown in fig. 5.1.3. PS7 reached its peak strength just before $\mu=3$; the cover began to spall at this juncture, reducing the load-carrying capacity of the section by a significant amount. Repeated cycling at $\mu=3$ and beyond resulted in only a slow degradation of strength.

Theoretical force-deflection response also appears on fig. 5.1.3. This curve takes into account the $P-\Delta$ effect. The theoretical model agreed relatively well with the experimental results in terms of maximum lateral force capacity; strength after spalling of the cover was somewhat below that predicted (this was likely caused by the nature of loading; the omission of external confinement about the plastic hinge, combined with its presence immediately outboard of this region, served to concentrate curvature, and therefore, damage, into the critical region). However, the test unit showed more ductility before the cover spalled than was expected. Peak load occurred at a greater deflection than was predicted ($\approx \mu=2.2$ predicted vs. $\mu=3$ actual). Failure was predicted at $\mu \approx 7$; the test unit did survive two cycles (albeit with rapidly degrading strength) at $\mu=8$.





Fig. 5.1.1: Prestressed pile shaft test unit PS7 at $\mu=3$

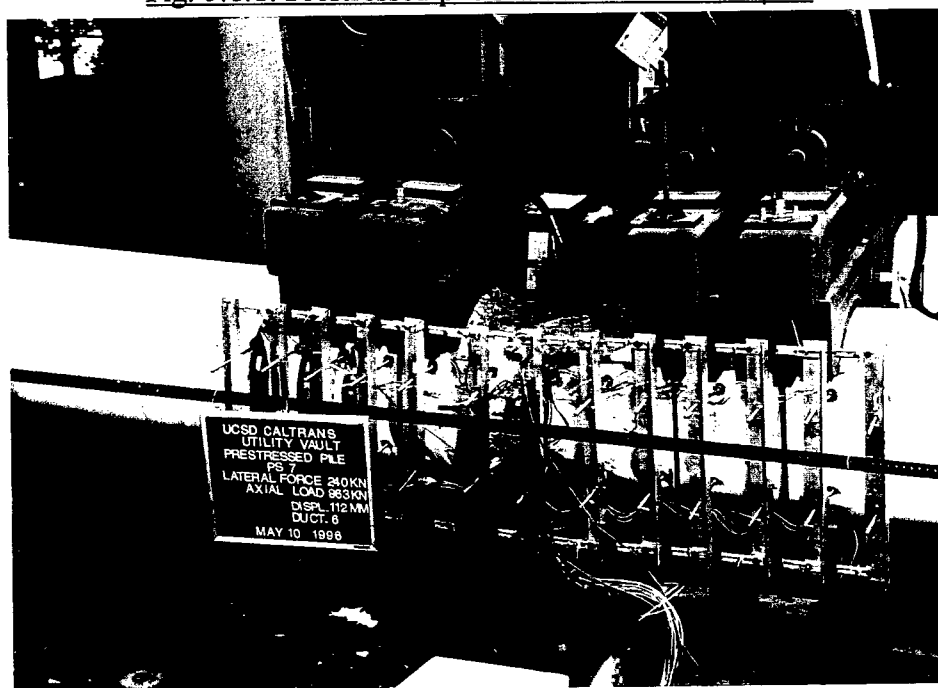


Fig. 5.1.2: Prestressed pile shaft test unit PS7 at $\mu=6$

1
2
3
4
5
6
7
8
9
10
11
12
13
14
15
16
17
18
19
20
21
22
23
24
25

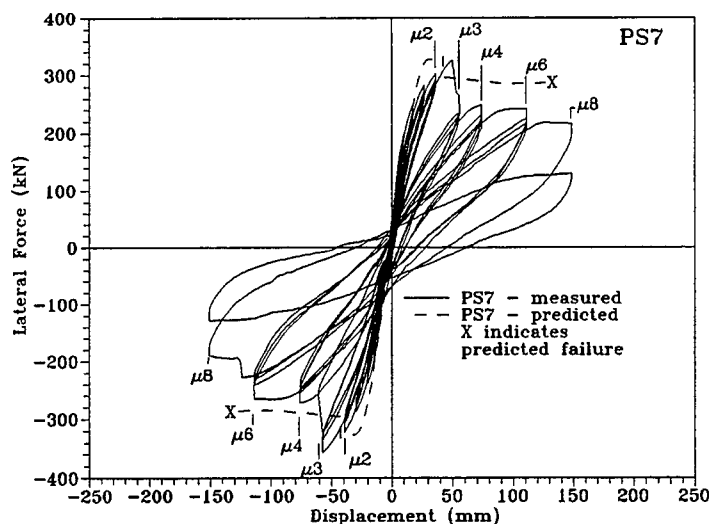


Fig. 5.1.3: Force-displacement hysteresis loops for pile shaft test unit PS7

Moment-curvature hysteresis loops appear in fig. 5.1.4, and show good agreement through the point noted by spalling of the cover at $\mu=3$. The post-spalling strength was somewhat lower than predicted, again, probably because of the test fixture concentrating curvature (and thus damage) into a limited area about the pile shaft's longitudinal midpoint (note that the measured critical-section curvature considerably exceeds that which was predicted at high levels of displacement ductility). (It may be noted that the predicted force-displacement response in fig. 5.1.3 takes $p-\Delta$ degradation into account, while the predicted moment-curvature in fig. 5.1.4 does not.)

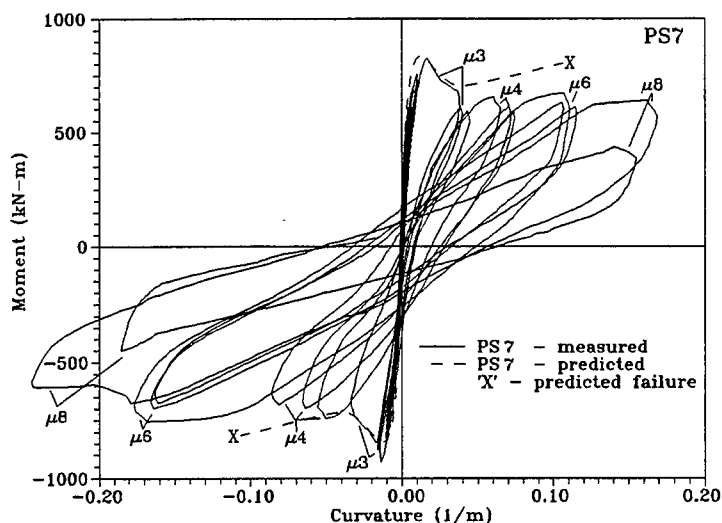


Fig. 5.1.4: Moment-curvature hysteresis loops about the center of prestressed pile shaft test unit PS7

Curvature profiles for PS7 are shown in fig. 5.1.5. Reasonably good agreement with predicted curvature is evident through lower ductilities up to $\mu=4$, but thereafter there was a concentration of curvature into the center of the test unit, somewhat greater than that which was predicted.

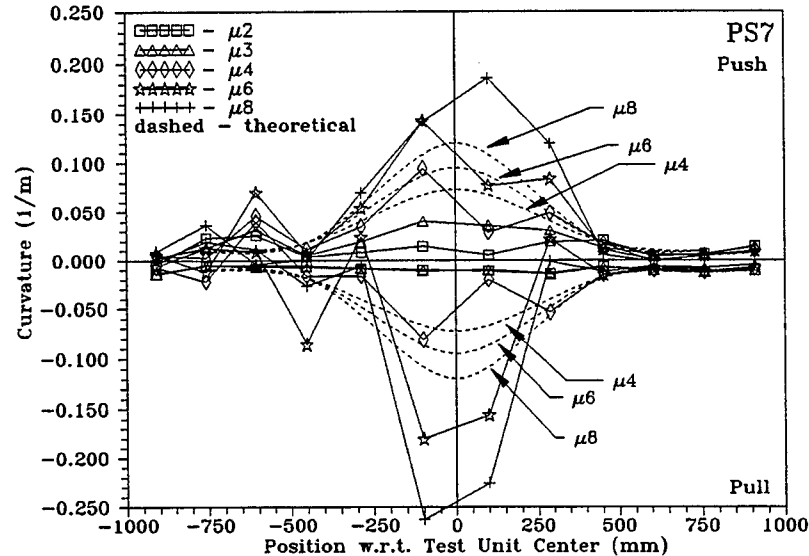


Fig. 5.1.5: Curvature profiles for pile shaft test unit PS7

Steel strain is shown in the next two figures, 5.1.6 (confining steel strain) and 5.1.7 (shear steel strain). Fig. 5.1.6 illustrates that which was seen in gross examination of the test unit; that is, that there was a significant degree of plasticity in the confining steel (it will be recalled that PS7's ultimate failure was presaged by fracture of confining steel).

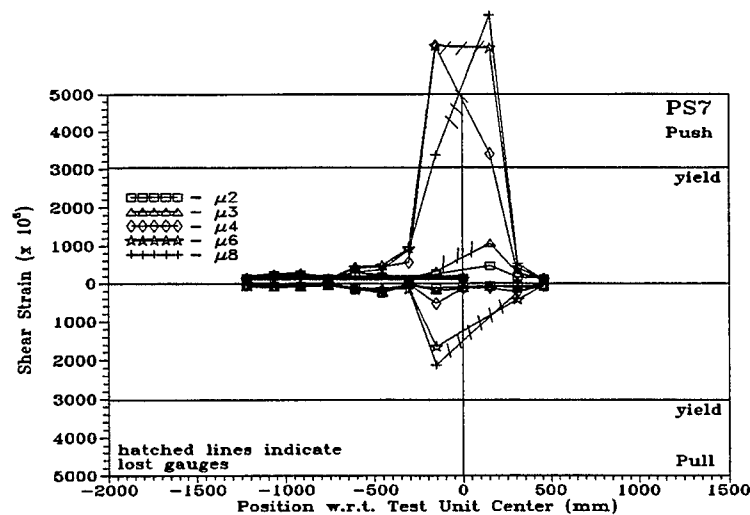


Fig. 5.1.6: Confining steel strain, prestressed pile shaft test unit PS7

Fig. 5.1.7 indicates that some plasticity was occurring at higher ductilities in the shear-resisting steel truss, as damage to the core concrete began to compromise that mechanism, or as confinement-induced strains spread to the horizontal axis.

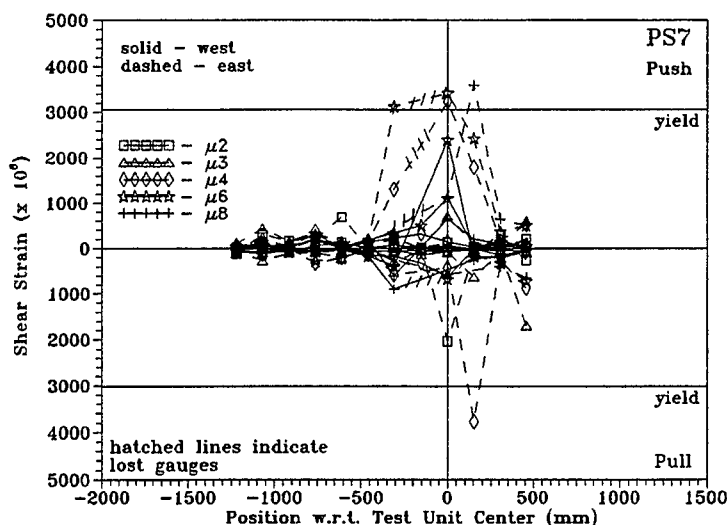


Fig. 5.1.7: Shear steel strain, prestressed pile shaft test unit PS7

5.2 PS8

Gross examination of PS8 during and after the test showed that plasticity was evident over a fairly wide area ($\approx 1D$), centered on the test unit's longitudinal midpoint. Incipient crushing began here at $\mu=3$, leading to a sudden and significant loss in load-carrying capacity. Spalling continued (and eventually spread about nearly the entire circumference of the pile) as the test unit was cycled through $\mu=6$, but there was relatively little degradation of strength. Spalling was seen beneath the inboard sections of saddles 'B' and 'D', as well.

Very few cracks were seen or expected, because of the nature of the prestressed section. Flexural cracks were seen over a span of 3.6 m, centered on the pile's longitudinal midpoint, indicating some significant degree of curvature through this area.

No prestressing tendons were fractured, nor were any of the transverse steel spirals. One spiral, however (located at the longitudinal midpoint, in the center of the top surface) exhibited necking and would likely have fractured had the test continued past $\mu=6$. At least four prestressing tendons on each side (top and bottom) were seen to buckle; at first, between spirals. At $\mu=6$ buckling was seen over a length of ≈ 200 mm, or approximately thrice the pitch of the spirals (the individual strands in the most severely buckled tendons were separated by over 6 mm). Because PS8 was the first prestressed pile tested in this series, and previous work indicated the possibility of a brittle failure,



testing was halted at $\mu=6$ for safety. (Post-mortem analysis of the test pile and the data resulted in a decision to go to higher levels of ductility, albeit with caution.)

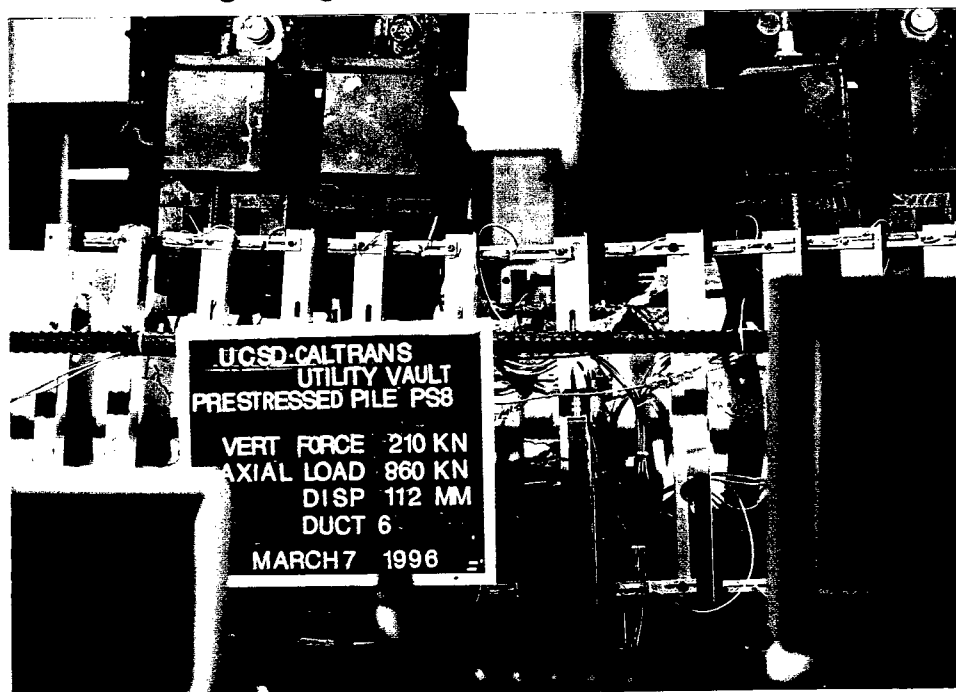


Fig. 5.2.1: Prestressed pile shaft test unit PS8 at $\mu=6$



Fig. 5.2.2: Buckling of strands within prestressing tendons in PS8 at $\mu=6$



The force deflection loops for PS8 are shown in fig. 5.2.3. PS8 reached its peak strength just before $\mu=3$, at which point the cover began to spall away, reducing the load-carrying capacity of the section by a significant amount. Repeated cycling at $\mu=3$ and beyond resulted in only a slow degradation of strength.

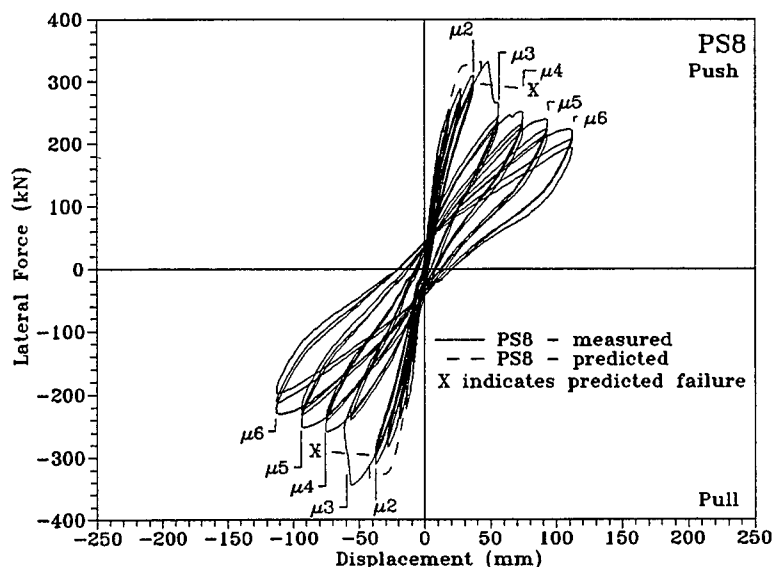


Fig. 5.2.3: Force-displacement hysteresis loops for pile shaft test unit PS8

Predicted force-deflection also appears on fig. 5.2.3. This prediction takes into account the P- Δ effect, and agrees relatively well with the experimental results in terms of maximum lateral force capacity. The test pile, however, showed considerably more ductility than was expected. Peak load occurred at a greater deflection than was predicted ($\mu \approx 2.2$ predicted vs. $\mu \approx 3$ actual). Failure was predicted at $\mu \approx 4.25$, but PS8 was still carrying load at $\mu=6$ (though, as explained below, was probably close to failure). Post-spalling strength was considerably below that which was predicted, as in the case of the similarly-loaded PS7 (i.e., no external confinement in the plastic hinge region).

Moment-curvature hysteresis loops for PS8 are shown in fig. 5.2.4, and show relatively good agreement with prediction through the softening branch (i.e., the spalling of the cover). Post-spalling strength is somewhat below that which was predicted, probably because the configuration of the test rig enhanced a concentration of curvature into the pile's longitudinal midpoint after spalling.

Curvature profiles for PS8 are shown in fig. 5.2.5, and are similar to those seen as a result of the testing of PS7; curvature is concentrated into the midpoint at higher ductilities. There is good agreement between the predicted and observed curvature profiles through the range of displacement ductility over which PS8 was cycled.

Confining steel strains for PS8 are given in fig. 5.2.6. Loss of strain gauge signal in the critical region unfortunately precludes a clear interpretation, but it would seem that

PS8's confining steel did undergo some degree of plasticity (recall that there was observable damage to confining steel, and that the observed buckling of tendons was certainly facilitated by plastic deformation of the confining spirals). The configuration of the load fixturing would have tended to concentrate curvature into the central region of the pile, and this seems to be reflected in fig. 5.2.6. (Also, it should be recalled that the testing of PS8 was halted before any drastic drop in capacity occurred.)

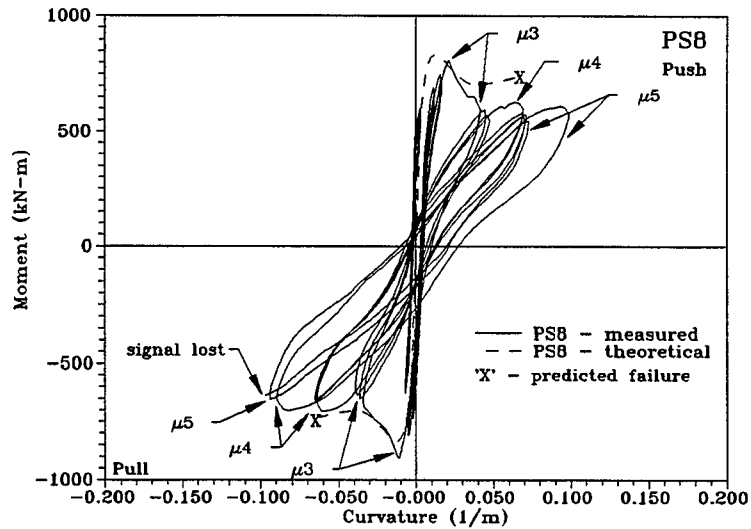


Fig. 5.2.4: Moment-curvature hysteresis loops about longitudinal midpoint, prestressed pile shaft test unit PS8

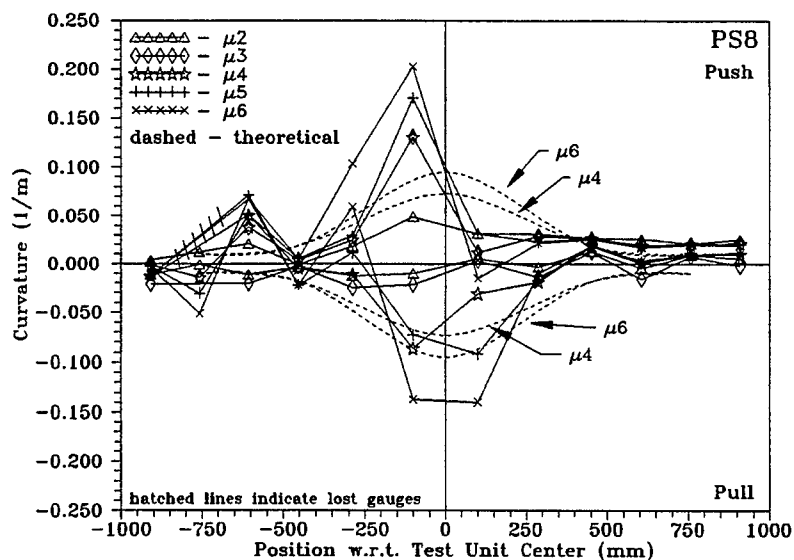


Fig. 5.2.5: Curvature profiles, prestressed pile shaft test unit PS8

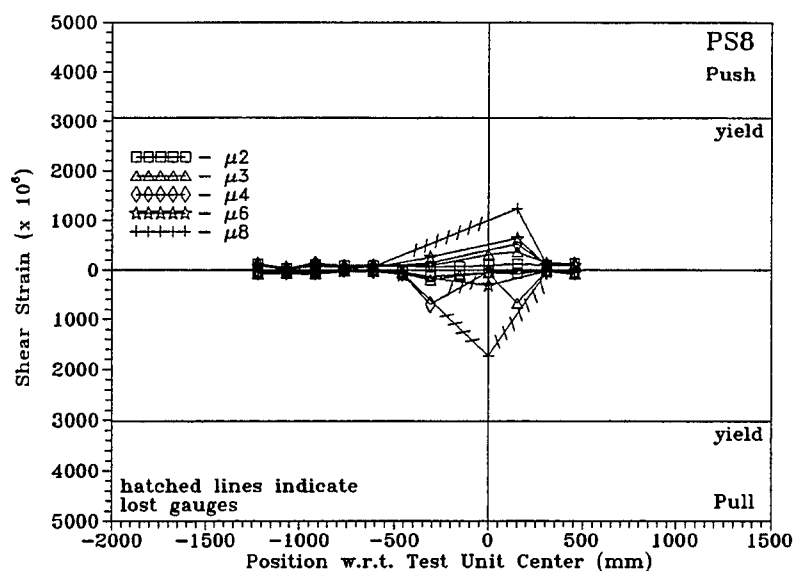


Fig. 5.2.6: Confining steel strains, prestressed pile shaft test unit PS8

Fig. 5.2.7 shows shear steel strain in PS8. Though some of the strain gauges in the critical region were lost at higher levels of ductility, enough remain to infer that the shear steel was not as highly mobilized as in the case of PS7 (fig. 5.1.7). PS8's shear steel seems to have remained largely in the elastic range.

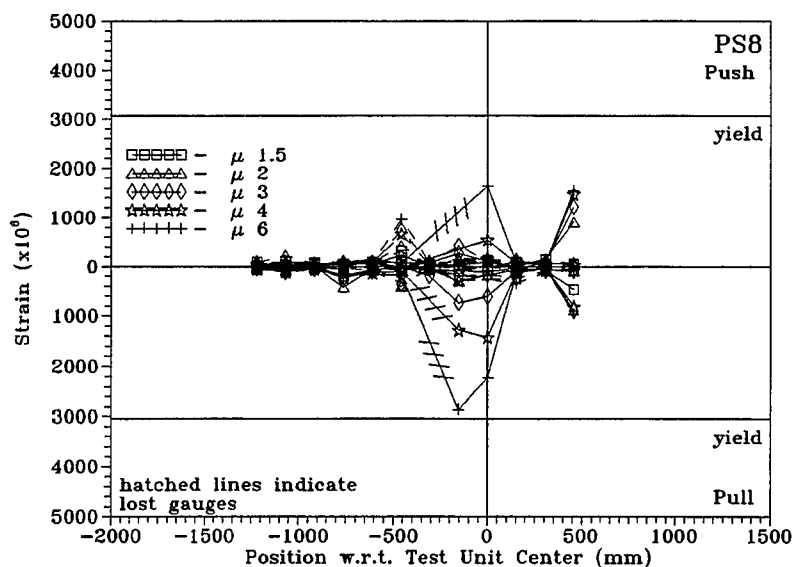


Fig. 5.2.7: Shear steel strains, prestressed pile shaft test unit PS8

5.3 PS9

Gross examination of PS9 during and after the test showed that plasticity was present over a fairly wide area ($\approx 1D$), centered on the test unit's longitudinal midpoint. Incipient crushing began here (beneath the central saddle; 'C' in fig. 5) at $\mu=2$, and led to a sudden drop in load-carrying capacity at the height of the first cycle at $\mu=3$; the cover would have begun to spall but for the constraint provided by the loading saddles. Crushing and limited spalling continued (and eventually spread about nearly the entire circumference of the pile) as the test unit was cycled through $\mu=8$, but strength was maintained after the drop at $\mu=3$. Spalling was not seen beneath the inboard sections of saddles 'B' and 'D' (ref. fig. 5) (a small amount of incipient crushing was observed in this area in the test of PS8). After the saddles were removed, large chunks of the cover could be pried away by hand; the cover beneath the top center saddle was extensively cracked and fissured, but it had approximately retained its original shape (when the bottom center saddle was removed, a large amount of fragmented cover came away with it).

Very few cracks were seen or expected, because of the high degree of prestressing. Flexural cracks were seen up to 2 m from the longitudinal midpoint of the test unit, indicating a significant degree of curvature to that point. At high levels of ductility ($\mu=6$ and above) very deep cracks were observed about the specimen's longitudinal midpoint, under the central saddle ('C' in fig. 5). Some of these were judged to extend at least 75 mm into the core (rods cast into the specimen for the mounting of curvature-measuring hardware were found to be loose after the test was concluded).

The force-deflection loops are shown in fig. 5.3.3. PS9 reached its peak strength just before $\mu=3$, at which point the cover began to spall away, reducing the load-carrying capacity of the section by a significant amount. Repeated cycling at $\mu=3$ and beyond resulted in maintenance of the post-spalling strength through high levels of ductility. Some degradation in strength was seen in repeated cycles at a given level of ductility.

Predicted force-deflection also appears on fig. 5.3.3. This prediction takes into account the $P-\Delta$ effect. The prediction agreed relatively well with the experimental results in terms of maximum lateral force capacity; however, PS9 showed more ductility capacity than was expected. Peak load occurred at a greater level of displacement ductility than was predicted ($\approx \mu=2.2$ predicted vs. $\mu=3$ actual). Failure was predicted at $\mu \approx 4$, and PS9 was still carrying load at $\mu=8$. As has been noted, neither observation of the specimen during the test nor examination of the data showed evidence that either tendons or transverse steel broke. In contradistinction with units PS7 and PS8, load carrying capacity after initial spalling matched or exceeded (on the pull cycles) theoretical strength, and capacity was maintained until ductilities greatly in excess of predicted ultimate levels.

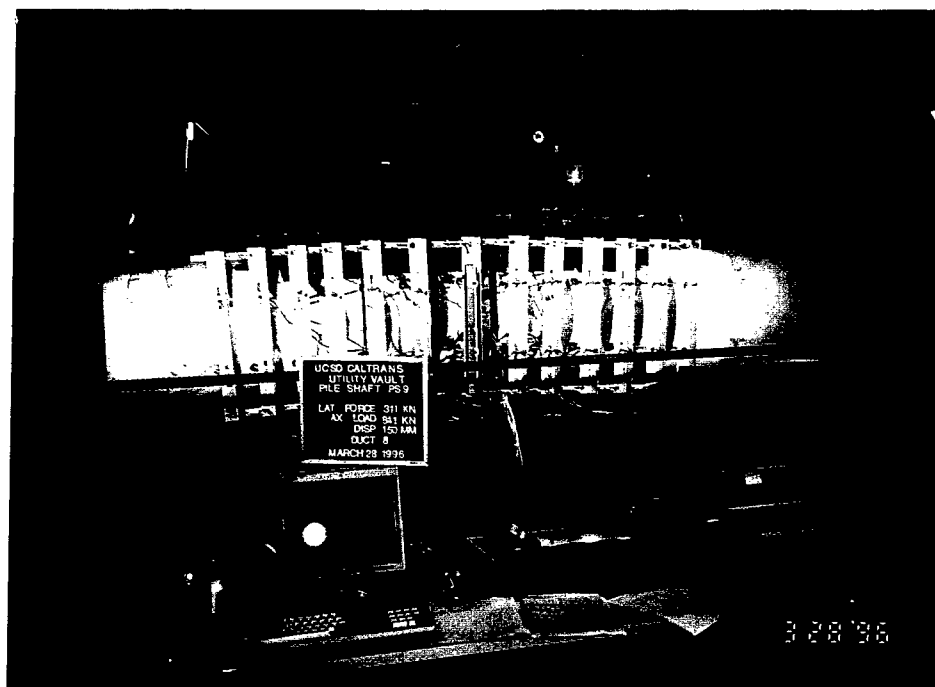


Fig. 5.3.1: Prestressed pile shaft test unit PS9 at $\mu=8$

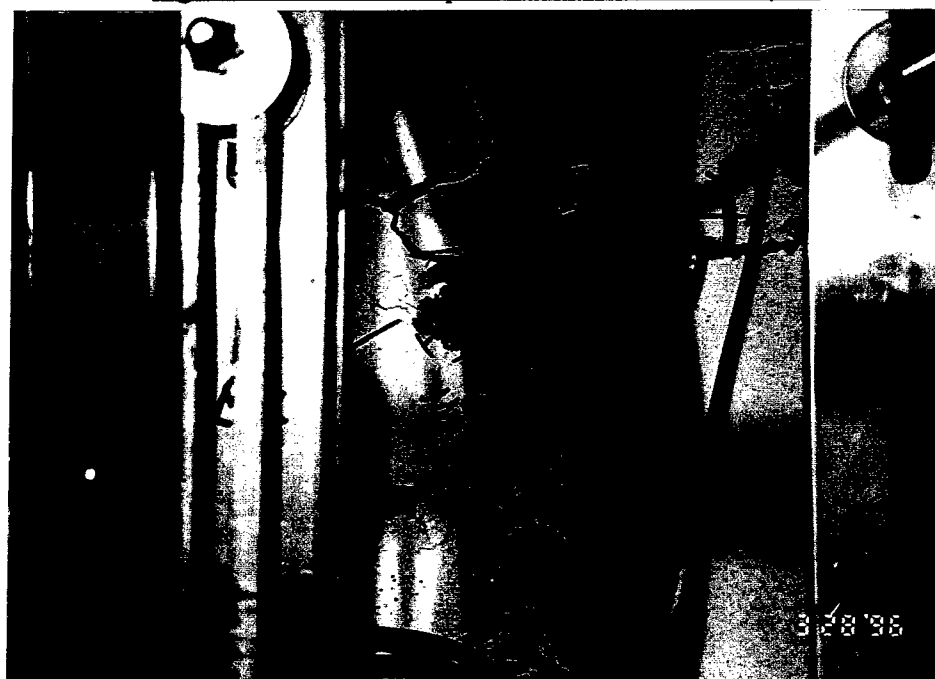


Fig. 5.3.2: Detail of crushing and spalling of cover, PS9 at $\mu=8$



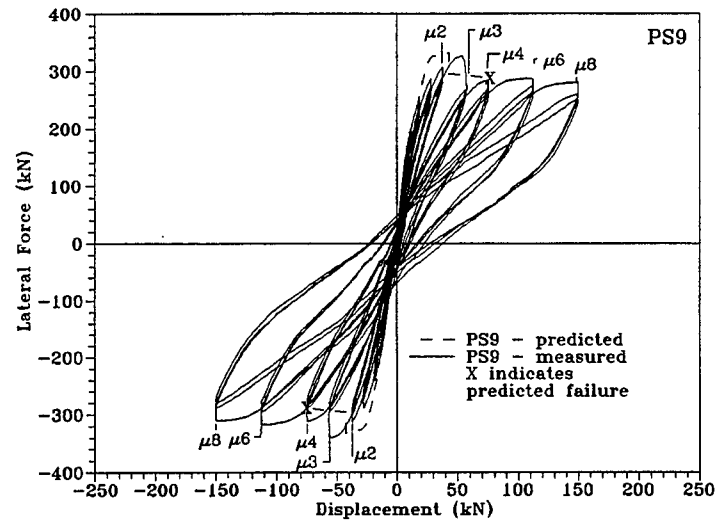


Fig. 5.3.3: Force-displacement hysteresis loops for pile shaft test unit PS9

Shown in fig. 5.3.4 are moment-curvature hysteresis loops for PS9, taken about the test unit's longitudinal midpoint. Interestingly, greater curvature is seen at high ductilities for the push cycles than for the pull cycles (also to be noted in the curvature profiles of fig. 5.3.5). This is probably because of a slight asymmetry in the pattern of prestressing strand allowing a shallower depth of cover concrete on the bottom of the shaft (i.e., that side which would be in compression during the pull cycles). Evidence to support this is seen in the force-displacement hysteresis loops (fig. 5.3.3), in which the pull-cycle post-spalling strength is somewhat higher than both the prediction, and the push-cycle post-spalling strength.

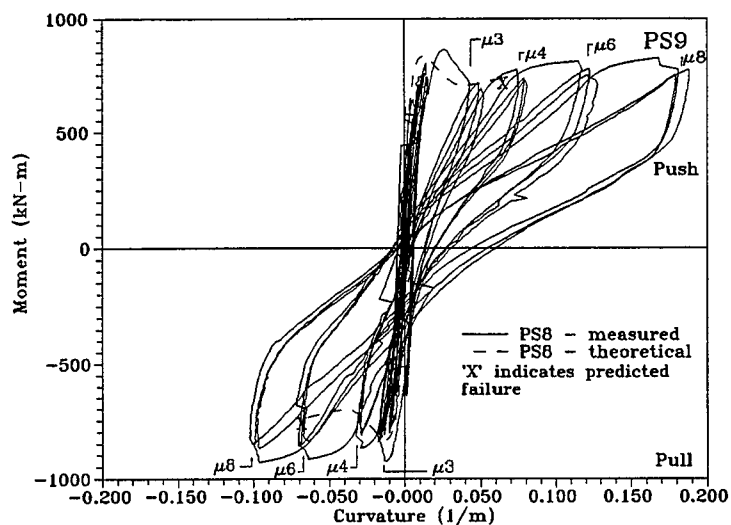


Fig. 5.3.4: Moment-curvature hysteresis loops about test unit midpoint, prestressed pile shaft test unit PS9

Aside from the obvious asymmetry mentioned above, a point of interest in the curvature profiles of fig. 5.3.5 is the good agreement with theory through the earlier (low levels of ductility) part of the test.

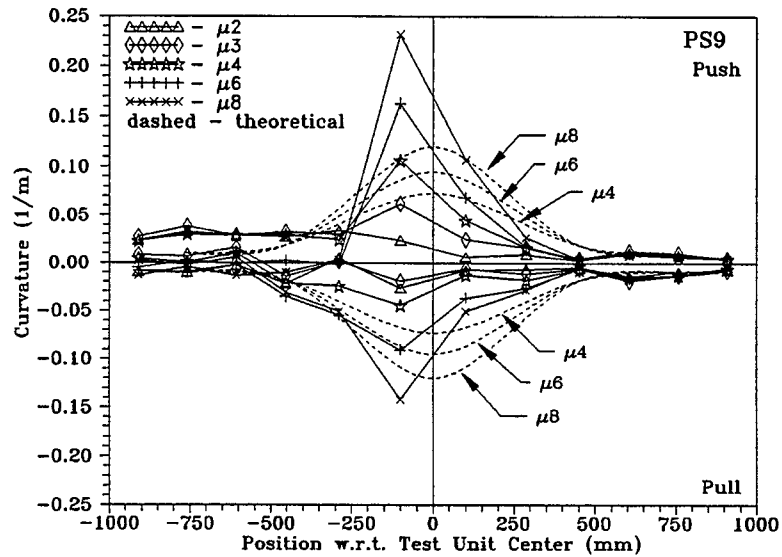


Fig. 5.3.5: Curvature profiles, prestressed pile shaft test unit PS9

Confining steel strains for PS9 are shown in fig. 5.3.6, and shear steel strains are shown in fig. 5.3.7. The confining steel seemed to see very little mobilization, showing to good effect the support provided by the external confinement (and restraint of the 'spalled' cover) from the load fixture simulating the soil about the shaft.

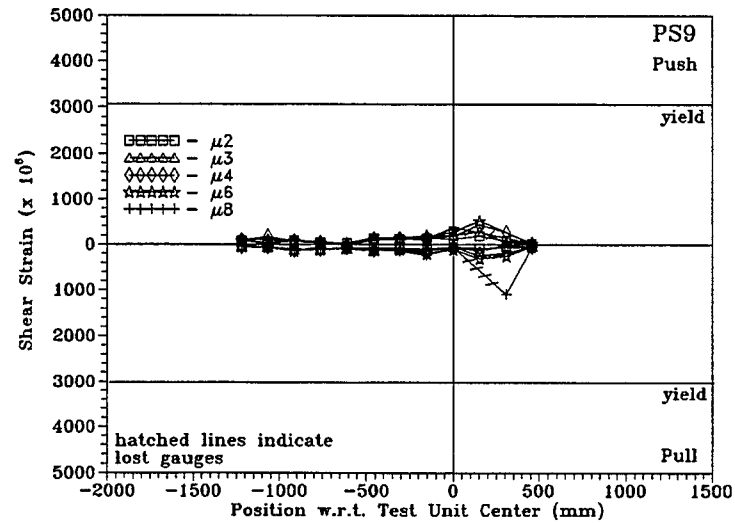


Fig. 5.3.6: Confining steel strains, prestressed pile shaft test unit PS9

Except for a single peak at $\mu=8$, the shear steel does not show much mobilization in the testing of PS9. Again, the external confinement was the likely cause, giving considerable support to the maintenance of the concrete shear-resisting mechanisms.

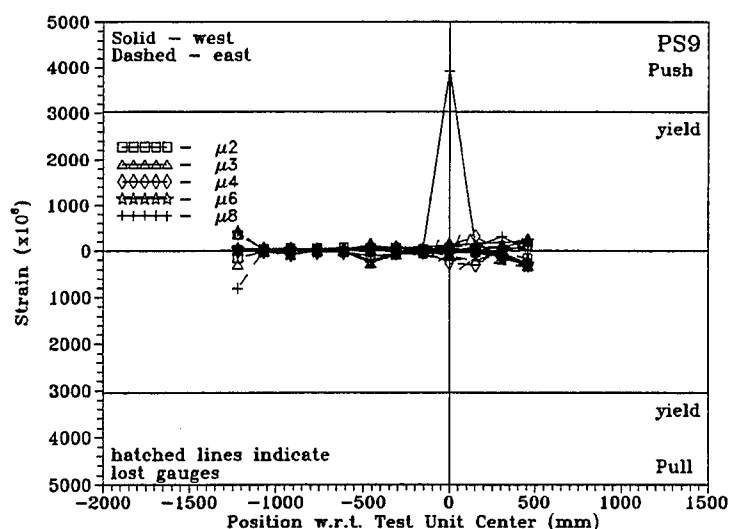


Fig. 5.3.7: Shear steel strains, prestressed pile shaft test unit PS9

5.4 PS10

Gross examination of PS10 during and after the test showed that plasticity was evident over a fairly wide area ($\approx 1D$), centered on the test unit's longitudinal midpoint. Initial crushing began at $\mu=2$, and spalling at $\mu=3$. Development of the plastic hinge seemed to be slightly asymmetric; more crushing was observed on the north margin of saddle 'C'. Conversely, flexure cracking was seen further from the longitudinal midpoint on the south half of the test unit (see fig. 5.4.2). This was most pronounced at $\mu=4$. (Thereafter, the center of plasticity seemed to migrate southward until, at the conclusion of the test, the plastic hinge seemed to be centered slightly to the south of the test unit's longitudinal midpoint.)

Crushing and limited spalling continued (and eventually spread about the entire circumference of the pile) as the test unit was cycled through $\mu=10$, but strength degraded only slowly through $\mu=8$, then rather more quickly as individual strands within the prestressing tendons started breaking on the way to $\mu=10$. After the saddles were removed, large chunks of the cover could be pried away by hand; the cover beneath the top center saddle was extensively cracked and fissured, but it had approximately retained its original shape (as in the case of PS9, when the bottom center saddle was removed, a large amount of fragmented cover came away with it).





Fig. 5.4.1: Prestressed pile shaft test unit PS10 at $\mu=8$

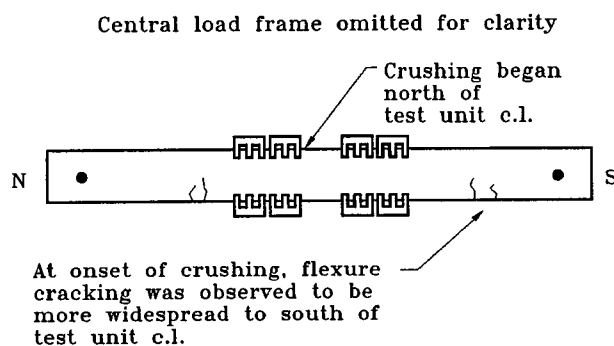


Fig. 5.4.2: Initial asymmetry of plastic hinge of pile shaft test unit PS10

Few cracks were seen (or expected), because of the high degree of prestressing. Onset of flexural cracking was noted at $\mu=1$. As noted above, flexural cracking showed some degree of asymmetry. Flexural cracks were seen up to 2 m south of the longitudinal midpoint of the test unit at the first cycle of $\mu=4$ (concurrent with crushing that seemed to be centered ≈ 0.2 m north of the longitudinal midpoint); by the third cycle at this level of ductility two wide, deep flexural cracks were observed under the center and south margin of saddle 'C'. Flexural cracks did not appear 2 m north of the longitudinal midpoint until $\mu=6$. At high levels of ductility ($\mu=6$ and above) the aforementioned deep cracks seemed to concentrate rotation. These cracks did extend into the core; however, the rods on which the curvature-measuring hardware (set 76.2



mm into the core) were still solidly embedded after the test was concluded (in the case of PS9, some had been loose, indicating that concrete had been degraded at that depth). Taken as a whole, cracking after $\mu=2$ was limited to minor extensions (many with shear inclination ... @ 45°) of existing cracks.

The force-deflection loops are shown in fig. 5.4.3. PS10 reached its peak strength just before $\mu=3$, at which point the cover began to crush and spall, reducing the load-carrying capacity of the section by a significant amount in the push (positive) cycle. The pull cycle, however, showed a more gradual reduction in strength through $\mu=4$, with symmetry restored beyond this point. Repeated cycling at $\mu=3$ and beyond resulted in maintenance of a great proportion of post-spalling strength through high levels of ductility, with some P- Δ degradation. Some degradation in strength was seen in repeated cycles at a given level of ductility.

Predicted force-deflection also appears on fig. 5.4.3. This prediction takes into account the P- Δ effect. The prediction agreed relatively well with the experimental results in terms of maximum lateral force capacity; however, the test unit showed considerably more ductility than was expected. Peak load occurred at a greater level of displacement ductility than was predicted ($\approx \mu=2.2$ predicted vs. $\mu=3$ actual). Failure was predicted at just past $\mu=3$, but PS10 was still carrying load at $\mu=10$, though its strength was degrading at this point. Observation of the specimen during the test, confirmed by 'post-mortem', indicated breakage of individual strands within the prestressing tendons during the $\mu=10$ cycle. At least one strand broke during $\mu=10$ push (positive), and at least seven broke during $\mu=10$ pull (negative). At most, four strands from a seven-strand tendon had ruptured. These were probably low-cycle fatigue failures, as the intact strands in a typical tendon were slightly separated, indicating buckling at maximum compression. This was facilitated by yielding observed in four adjacent spirals in the plastic hinge region.

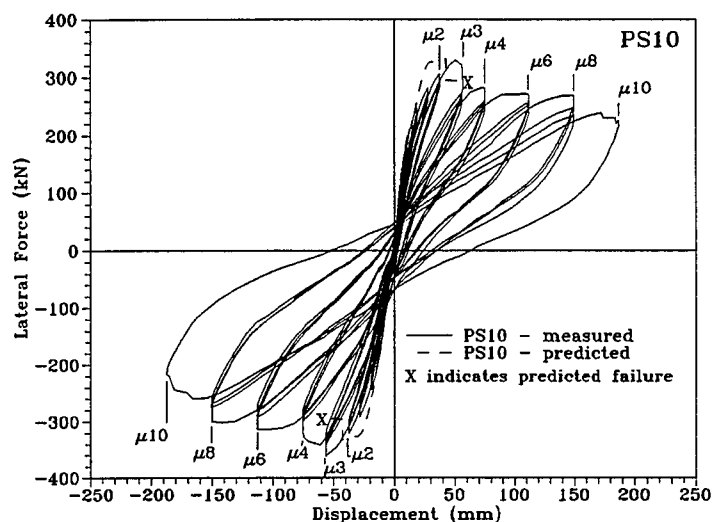


Fig. 5.4.3: Force-displacement hysteresis loops for pile shaft test unit PS10

Shown in fig. 5.4.4 are moment-curvature hysteresis loops for PS10, about the longitudinal midpoint of the pile shaft. The influence of the external confinement in forestalling the development of severe localized curvature (and subsequent failure) is evident.

Shown in fig. 5.4.5 are PS10's curvature profiles. While the curvature achieved at high levels of displacement ductility are greater than those predicted, they maintain the same general shape of the theoretical curves, lending credence to the conclusion drawn above that the external confinement provided to PS10 forestalled the development of a localized lethal level of curvature. (This is also borne out by observations during the test, and by the ultimate failure mechanism, i.e., failure of individual strands within the prestressing tendons.)

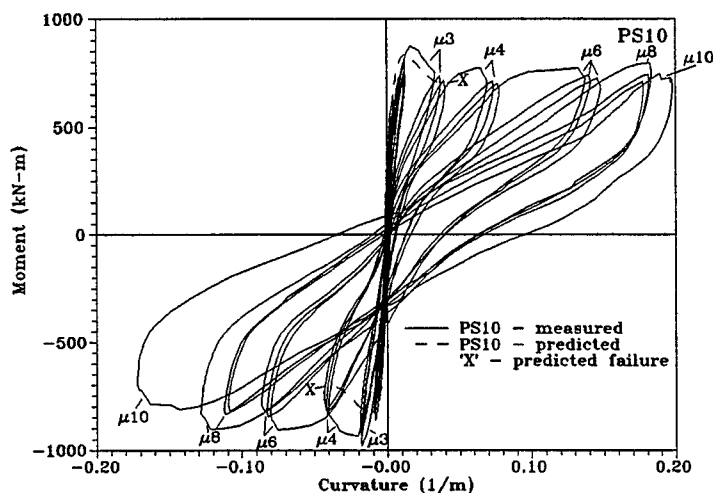


Fig. 5.4.4: Moment-curvature hysteresis loops about test unit midpoint, prestressed pile shaft test unit PS10

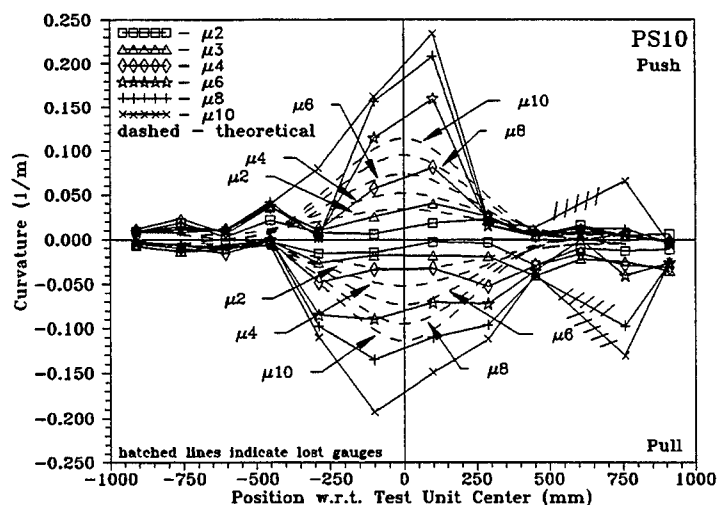


Fig. 5.4.5: Curvature profiles, prestressed pile shaft test unit PS10

Unfortunately, data from strain gauges on the confining and shear steel was unavailable in the critical region, but what data there is points to considerable mobilization of the transverse reinforcement in the shear-resisting truss mechanism (recall that this was the most lightly-reinforced test unit in this series).

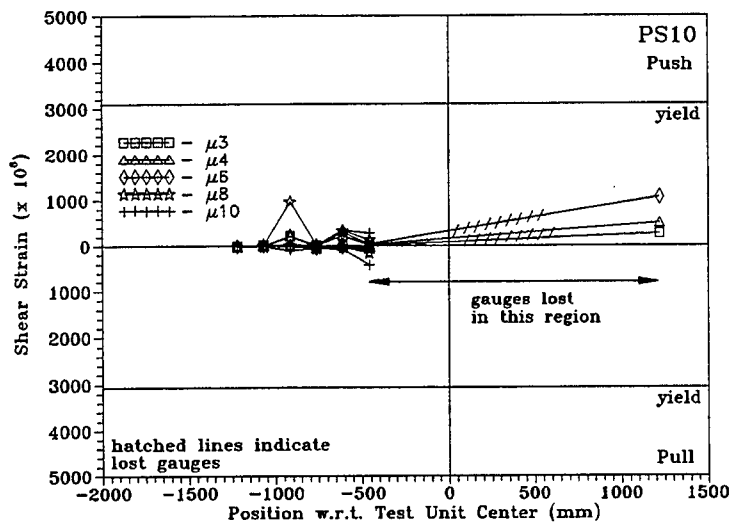


Fig. 5.4.6: Confining steel strains, prestressed pile shaft test unit PS10

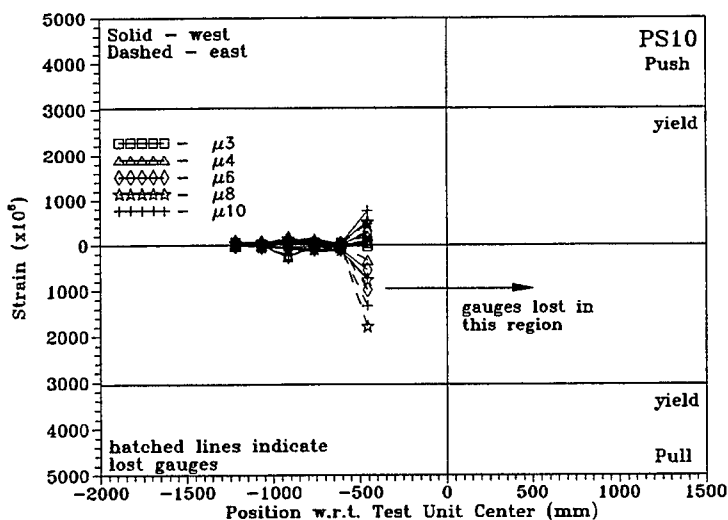


Fig. 5.4.7: Shear steel strains, prestressed pile shaft test unit PS10

5.5 Comparisons between Solid Prestressed Piles PS7 - PS10

Shown in fig. 5.5.1 are the force-displacement hysteresis loops for PS7 - PS10. Regarding the provision of external confinement (PS9 and PS10) or its absence (PS7 and PS8), it is immediately apparent that this variation has a significant effect. The post-spalling strengths of PS7 and PS8 were somewhat below that predicted, while those of PS9 and PS10 matched or exceeded predicted strength. Also, failure modes were different; PS7 failed through spiral fracture followed by core crushing, while PS10 (with one-third the volumetric transverse reinforcement ratio of PS7) maintained its core integrity up to failure of individual strands within the prestressing tendons. The effect of external confinement is also seen to advantage in a comparison of the force-displacement envelopes of the similarly-reinforced PS8 and PS9 (fig. 5.5.4), which reflect both the greater post-spalling strength of the externally-confined example, and its greater displacement ductility capacity. It should be noted that in the case of PS9, the post-spalling plateau is flat, while PS8 begins to soften.

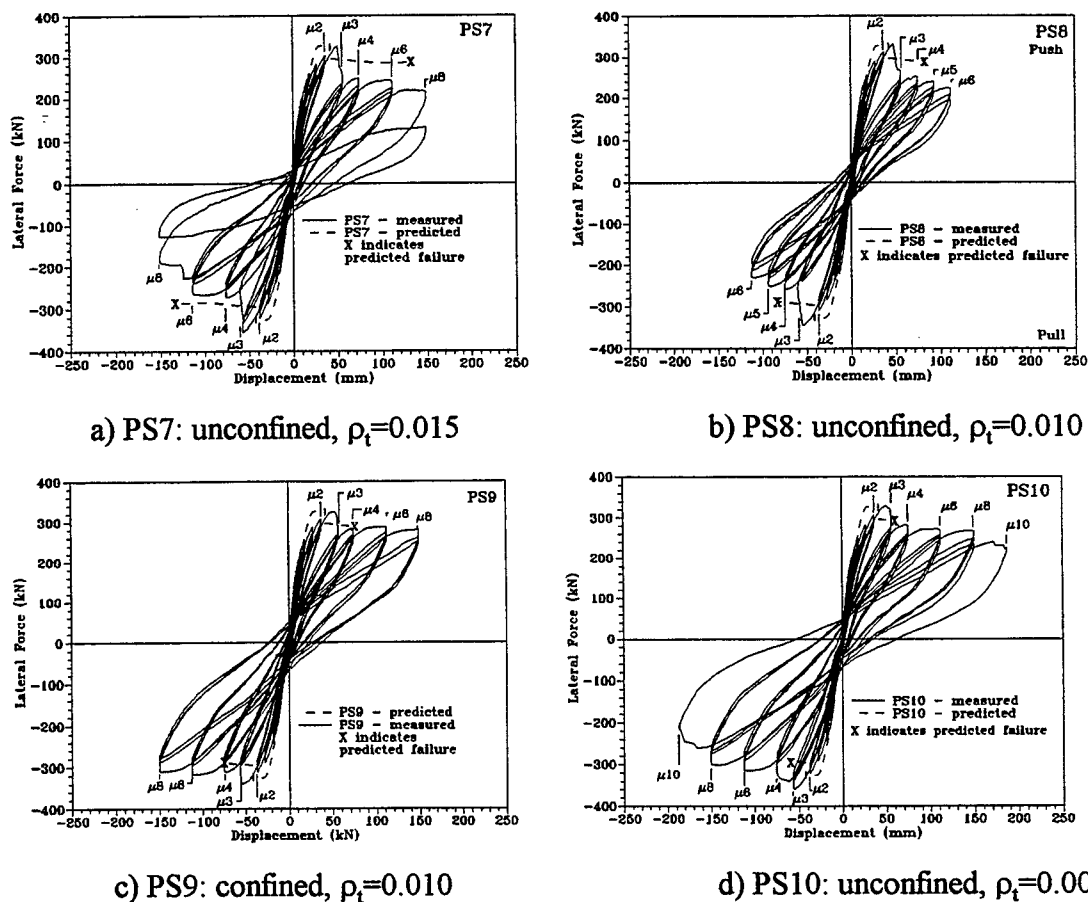


Fig. 5.5.1: Comparison of force-displacement hysteresis loops for prestressed pile shaft test units PS7 - PS10

The presence of external confinement did not seem to have an effect on the point of onset of crushing and spalling. In all cases, incipient crushing was seen at $\mu=2$, and spalling took place at $\mu=3$. Where external confinement was provided, the cover was, as mentioned previously, constrained to remain largely in place (if not intact); actual crushing and spalling was seen between the 'teeth' of the load saddles on the exposed surface of the pile. External confinement clearly did not prevent the drop in lateral capacity that occurred at $\mu=3$, but the retention of the damaged cover did contribute to the post-spalling strength.

Variation of transverse steel ratios had, as was expected from prior testing of cast-in-place pile shaft specimens PS1 - PS6 [15], a greater effect in the absence of external confinement to the plastic hinge. Indeed, it may be said that up to the limit of travel of the test rig, there was no significant variation in performance caused by varying transverse steel when external confinement was provided.

The effect of external confinement and varying transverse steel may be seen more clearly in the force-displacement envelopes shown in figs. 5.5.2 (PS7 and PS8) and 5.5.3 (PS9 and PS10). In fig. 5.5.2 (no external confinement), the performance of PS8 ($\rho_t=0.010$) is beginning to drop off at $\mu=6$ (at which point the test was halted). PS7 ($\rho_t=0.015$) reached this level of degradation at $\mu=8$.

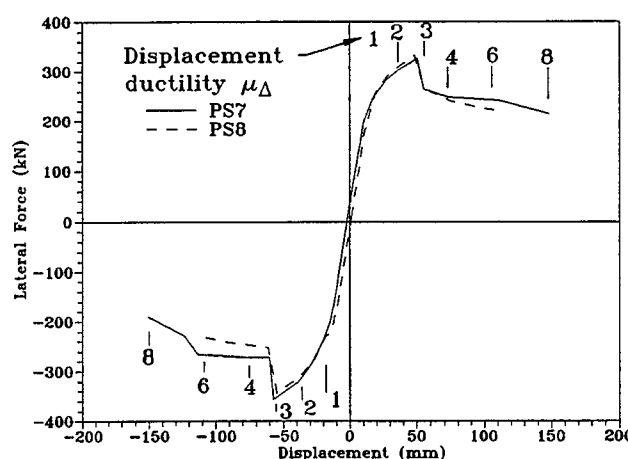


Fig. 5.5.2: Force-displacement envelopes for PS7 ($\rho_t=0.015$) and PS8 ($\rho_t=0.010$); no external confinement about plastic hinge

Fig. 5.5.3, on the other hand, shows that the presence of external confinement makes the level of transverse steel almost moot. (The testing of PS9 was stopped at $\mu=8$.)

Fig. 5.5.4 shows the considerable influence of external confinement on post-spalling strength. PS8 and PS9 show similar behavior to $\mu=3$, but whereas the post-spalling plateau in the unconfined example (PS8) shows progressive degradation, the

external confinement in PS9 allows the pile to maintain its load-carrying capacity virtually unimpaired for $\mu=3$ to $\mu=6$, with some degradation setting in above that point.

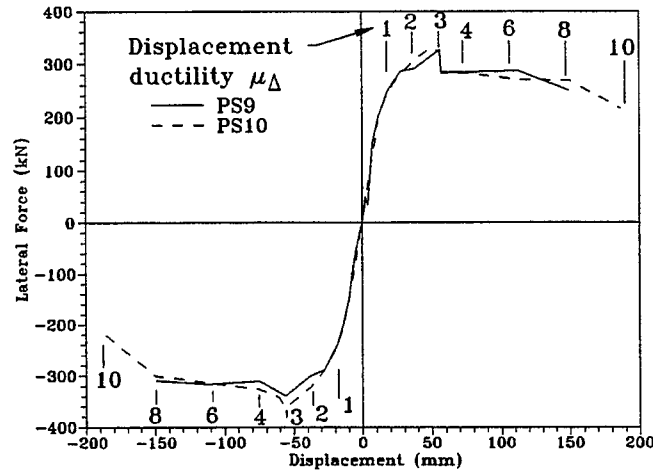


Fig. 5.5.3: Force-displacement envelopes for PS9 ($\rho_t=0.010$) and PS10 ($\rho_t=0.005$); with external confinement about plastic hinge

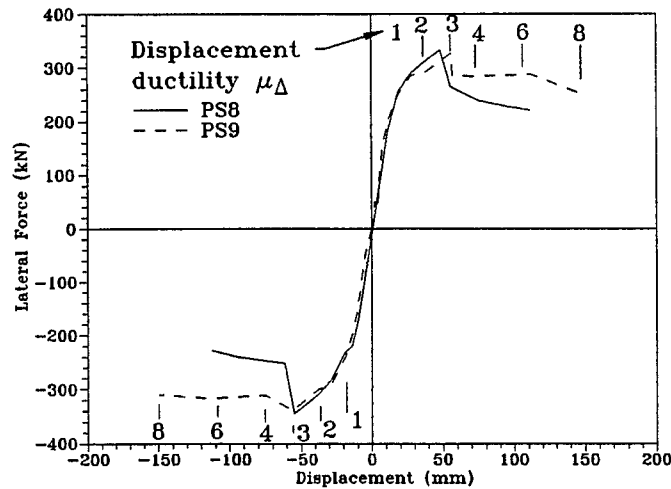


Fig. 5.5.4: Force-displacement envelopes for PS8 ($\rho_t=0.010$) and PS9 ($\rho_t=0.010$); PS8 with no external confinement about plastic hinge, PS9 with external confinement

Table 5.5.1 gives predicted and experimental ultimate displacements, and plastic hinge lengths. The theoretical plastic hinge length was defined as the inelastic rotation (graphically represented in fig. 5.5.5) divided by the predicted inelastic curvature (i.e., the maximum predicted curvature minus the curvature predicted at the theoretical unitary ductility). The experimental plastic hinge length was defined as the ratio of the plastic rotation (plastic curvature integrated over the length over which cracking was observed) to the maximum inelastic curvature in the center of the plastic hinge region^[17] (fig. 5.5.5):

$$l_p = \frac{\Theta_p}{\Phi_p} = \frac{\Theta_{ultimate} - \Theta_{yield}}{\Phi_{ultimate} - \Phi_{yield}} \quad (5.1)$$

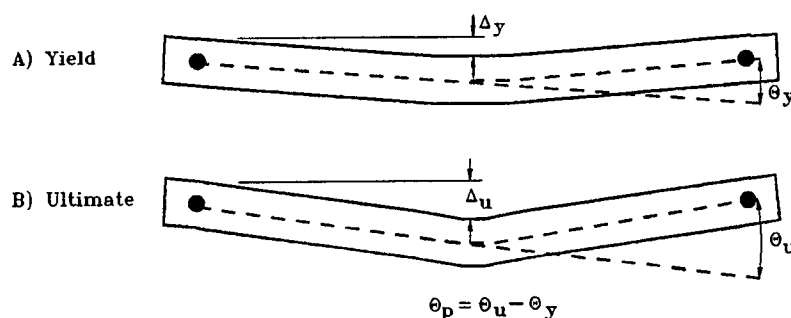


Fig. 5.5.5: Determination of plastic rotation

The large plastic rotations and relatively wide spread of damage resulted in the unconfined pile shafts (PS7 and PS8) having somewhat greater plastic hinge lengths than their confined counterparts. It should be noted that the results from PS8 and PS9 may be artificially low, because these tests were not taken to total failure.

TABLE 5.1: PREDICTED VS. ACTUAL PLASTIC HINGE LENGTHS, PS7-10

Test Unit	External Confinement of Hinge	Predicted l_p (diameters D)	Actual l_p (diameters D)	$\frac{l_{p, exp}}{l_{p, pred.}}$
PS7	No	1.22	1.60	1.31
PS8	No	1.18	1.11	0.94
PS9	Yes	1.28	0.71	0.55
PS10	Yes	1.11	1.01	0.91

Table 5.5.2 compares the predicted and actual ultimate midpoint displacements. One may notice again that, for the most part, the prestressed sections displayed considerably more ductility capacity than had been expected. Consideration should be given to the fact that of the four tests, only PS7 and PS10 were carried to the point of failure; thus it can be seen that the shorter-than-predicted plastic hinge length experienced by PS7 allowed only a small increase in actual displacement above that predicted, while PS10, with its close agreement in predicted and actual plastic hinge lengths, showed much higher displacements than were expected. What is described for PS10 may also be said of PS9, though that test pile did not fail at $\mu=8$, the highest ductility to which it was taken; in contrast, PS8, which was close to failure at $\mu=6$, followed the pattern of PS7 in its close-to-predicted displacements and shorter-than-predicted plastic hinge length. It should be noted that the prediction of failure was based

on the ultimate concrete compression strain allowed by the Mander model for confined concrete, which is inherently conservative.

TABLE 5.2: PREDICTED VS. ACTUAL ULTIMATE DISPLACEMENT, PS7-10

Test Unit	External Confinement of Hinge	Predicted Δ_{ult}	Actual Δ_{ult}	$\Delta_{ult, exp.} / \Delta_{ult, pred.}$
PS7	No	132.6 mm	149.6 mm	1.13
PS8	No	83.6 mm	112.6 mm	1.34
PS9	Yes	78.5 mm	149.6 mm	1.91
PS10	Yes	60.7 mm	187 mm	3.08

Confinement provided by the load fixture to the central region of the plastic hinge in PS9 and PS10 may be approximated as an equivalent lateral soil pressure. The rubber pads chosen (see fig. 3.3) model a soil with a subgrade reaction modulus of $K \approx 25600$ kN/m³; the lateral confining pressure supplied by the rubber pads is calculated as

$$f_l = \frac{P}{bl} \quad (5.2)$$

in which

P = maximum shear load (348 kN; average over four tests)
 b = transverse dimension of load saddle (0.53 m)
 l = half-length of loaded area (=0.85 m)

The maximum lateral pressure provided is thus 0.77 MPa. The transverse steel provides a confining pressure of^[17]

$$f_l = \frac{2A_s f_{yh}}{D' s} \quad (5.3)$$

in which

A_s = transverse steel bar area
 f_{yh} = transverse steel yield stress
 D' = transverse steel spiral diameter
 s = spiral pitch

The lateral pressure provided by the transverse steel is thus

PS7 - 3.7 MPa
 PS8, PS9 - 2.4 MPa
 PS10 - 1.68 MPa

The level of 'soil' confinement is thus small compared to that from transverse reinforcement. It thus appears that the critical influence is the ability to at least partly maintain the integrity of the cover concrete.

A comparison of moment-curvature hysteresis loops (taken about the longitudinal midpoint) is shown in fig. 5.5.5. The effect of external confinement is very clearly seen in the development of a large amount of curvature at high levels of ductility in the 'unconfined' examples (PS7 and PS8); compare this to the very regular loops produced by PS9 and PS10. The latter show little change in curvature when cycled at high ductilities (even though there is some reduction in moment capacity) until the point of failure (PS9 did not overtly fail).

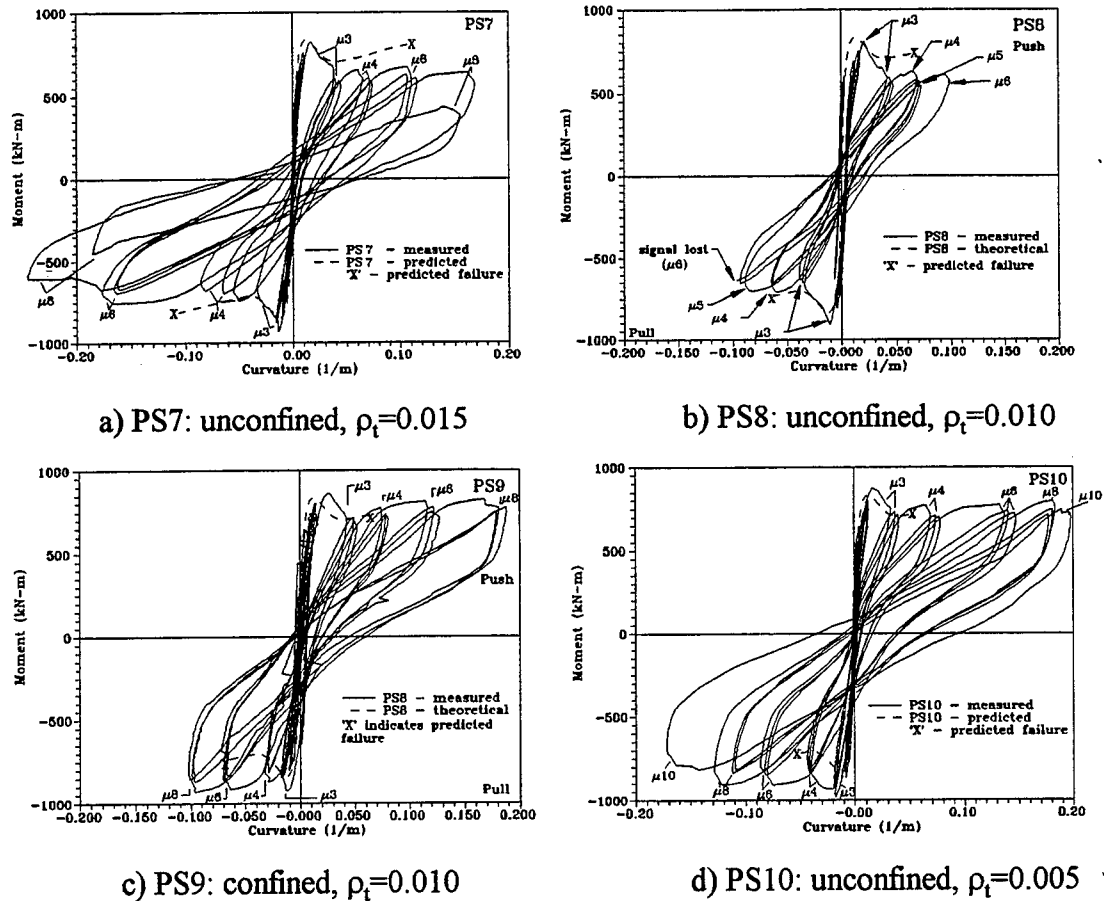


Fig. 5.5.6: Comparison of moment-curvature hysteresis loops for prestressed pile shaft test units PS7 - PS10

Shown in fig. 5.5.7 - 5.5.9 are curvature profiles comparing, first, the unconfined examples PS7 and PS8; then, the confined PS9 and PS10, and finally PS8 and PS9, similarly reinforced but differing in external confinement. The results support those

discussed above, that the lack of external confinement allowed a lethal degree of curvature to be concentrated into the center of the plastic hinge at an earlier point in the test, presaging failure. At a given level of displacement ductility (post-spalling; i.e., $\mu=4$), this amounted to $\approx 15\text{-}20\%$ more curvature for the unconfined example. It is noteworthy that the overall shape of the profiles does not drastically differ; the loss (or loss of integrity) of the cover certainly allowed a concentration of rotation into a short length, but the constraint of the cover retarded its speed of development.

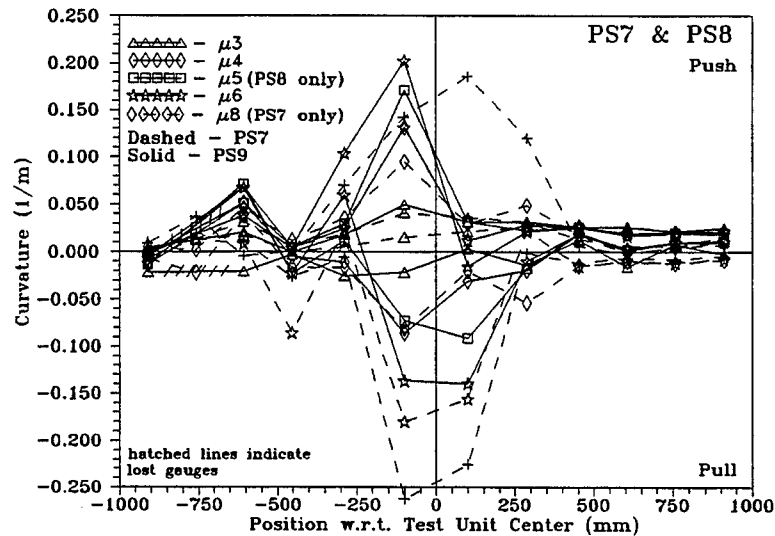


Fig. 5.5.7: Curvature profiles, PS7 ($\rho_t=0.015$) and PS8 ($\rho_t=0.010$); no external confinement

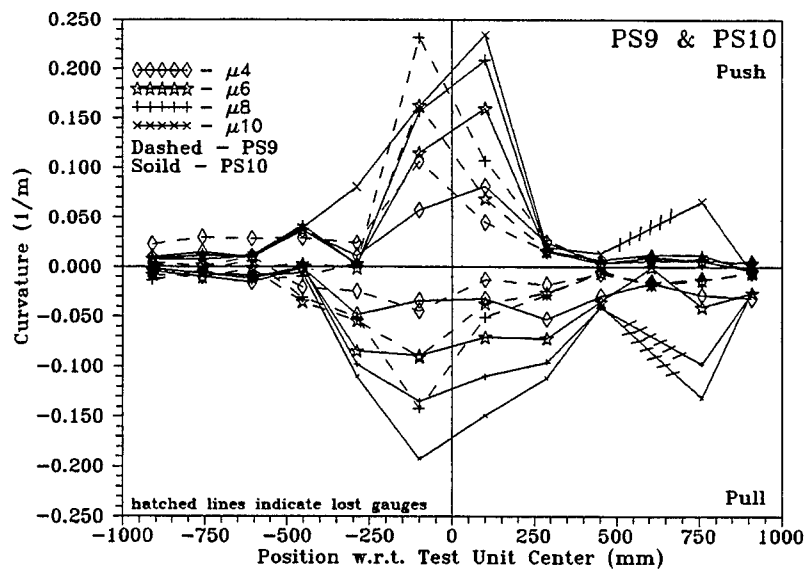


Fig. 5.5.8: Curvature profiles, PS9 ($\rho_t=0.010$) and PS10 ($\rho_t=0.005$); with external confinement

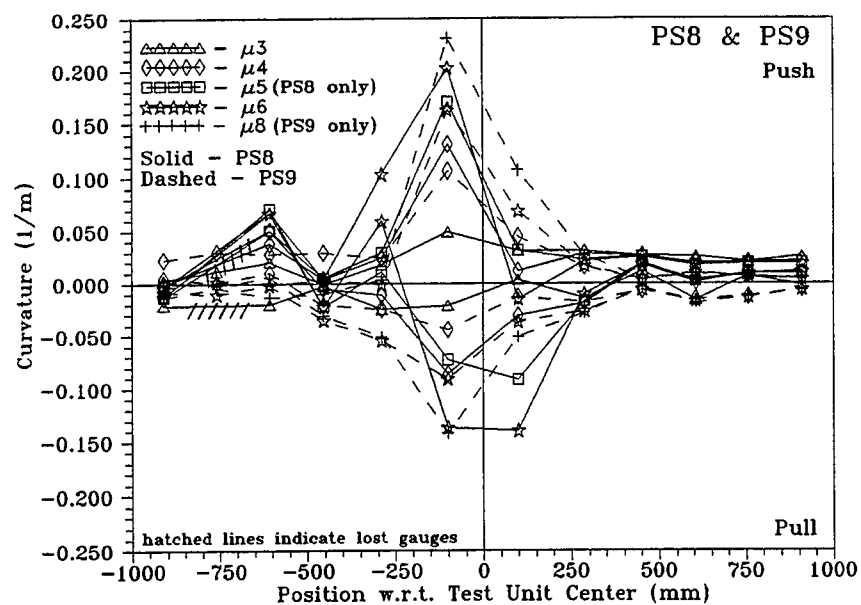


Fig. 5.5.9: Curvature profiles, PS8 and PS9 (both $\rho_t=0.010$); PS9 with external confinement, PS8 without

6. Results - Hollow Prestressed Piles

6.1 PS11 (heavy reinforcement, plastic hinge confined)

Observations of PS11 through the course of the test showed the first flexural cracks appearing at the longitudinal midpoint of the pile at $\mu=1$, and spreading through (and beyond) the loading area by the end of the test. The pattern of flexural cracks eventually covered a length of slightly more than three meters ($\approx 5D$), and was centered about 200 mm south of the test unit's longitudinal midpoint. This led one to anticipate that failure would likely occur at this point (offset slightly south of the midpoint), and this was indeed the case. Only minor shear cracking was observed through the loading area; onset was at $\mu=1.5$. Some shear cracks turned past the nominal 45° inclination to lie almost parallel with the pile's long axis. Very little incipient crushing or spalling was observed prior to failure.

The failure of PS11 during the first push excursion to $\mu=4$ very sudden, with an almost instantaneous drop in 50% of the lateral load, and over 10% of the axial load. An area of cover concrete under the top center load saddle was observed to be damaged; the center of the damaged area was @200 mm south of the longitudinal midpoint of the pile, as anticipated in the above paragraph. (It should be noted that the testing of PS14, first of the hollow piles to be tested, was halted at this juncture, to preserve the test unit in the cleanest possible state for sectioning and further examination). The fate of PS11, however, was to be cycled through to a pull maximum at $\mu=4$, which resulted in very symmetrical behavior, followed by very heavy damage when the remaining compression zone failed. The lateral force dropped from 250 to 110 kN almost instantaneously; while PS11 was held at $\mu=4$ for examination, the load continued to drop off to 34 kN as the test pile groaned and shifted within its restraints. Axial load dropped by 40%. The damage was not symmetrical; most seemed to be centered about 200 mm north of the longitudinal midpoint. As mentioned, it was very severe, with large pieces of cover shattered, exposing the transverse steel (cover thickness was 41 mm). The core concrete thus exposed was seen to be extensively cracked and fissured, and its integrity was certainly gone (the void had been filled with water during storage, to dissolve the Sonovoid™ that formed the core; while most of the water had been removed before test, some that remained began to leak out through the damaged pull-cycle compression zone on the bottom of the pile after the pull to $\mu=4$). In fig. 6.1.1 is shown the appearance of the push-cycle compression area after removal of the fixturing; at first glance the damage does not seem severe. This is deceiving, however, as the integrity of the shell was gone. Fig. 6.1.2, taken after sectioning, shows the spalled area of the inner core face. The spalled concrete of the shell was only lightly held in place by friction, and could be prised away by hand (fig. 6.1.3) to show that the damage extended all the way through the shell.



Fig. 6.1.1: Push-cycle compression zone of PS11 after removal of fixturing (heavy reinforcement, plastic hinge confined)



Fig. 6.1.2: PS11 after sectioning, showing spalled area of core face (heavy reinforcement, plastic hinge confined)





Fig. 6.1.3: The spalled cover of PS11 could be easily removed, showing that the damage went all the way through the shell (heavy reinforcement, plastic hinge confined)

Shown in fig. 6.1.4 are the force-deflection hysteresis loops for PS11. The prediction matches the actual performance of the test unit quite well, but underestimates the total displacement achieved. Because the failure mechanism was restricted to the concrete compression zone, it was to be expected that a second half-cycle (a reversal of load to the same displacement) would show symmetrical behavior to failure; this is seen in fig. 6.1.4.



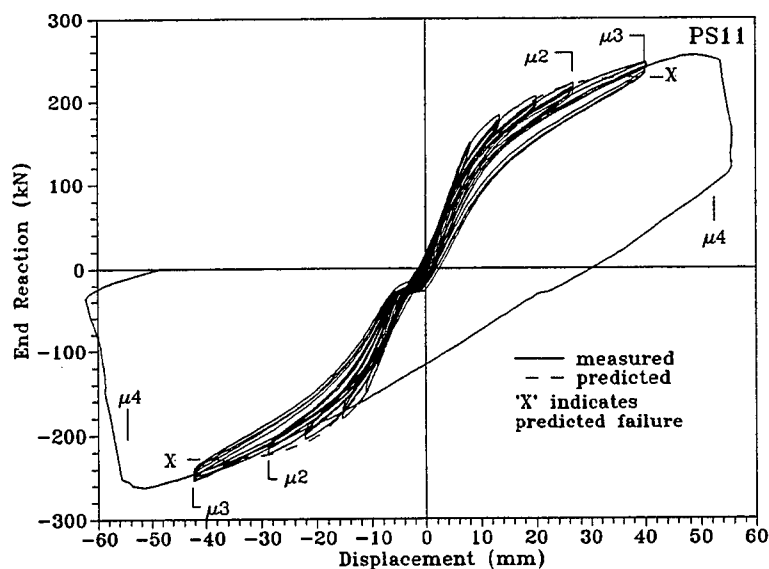


Fig. 6.1.4: Force-deflection hysteresis loops for hollow pile shaft test unit PS11 (heavy reinforcement, plastic hinge confined)

Shown in fig. 6.1.5 is a comparison of interpolated core strain versus curvature for PS11. It may be seen that the actual core strain and curvature withstood by PS11 was considerably in excess of that which was predicted.

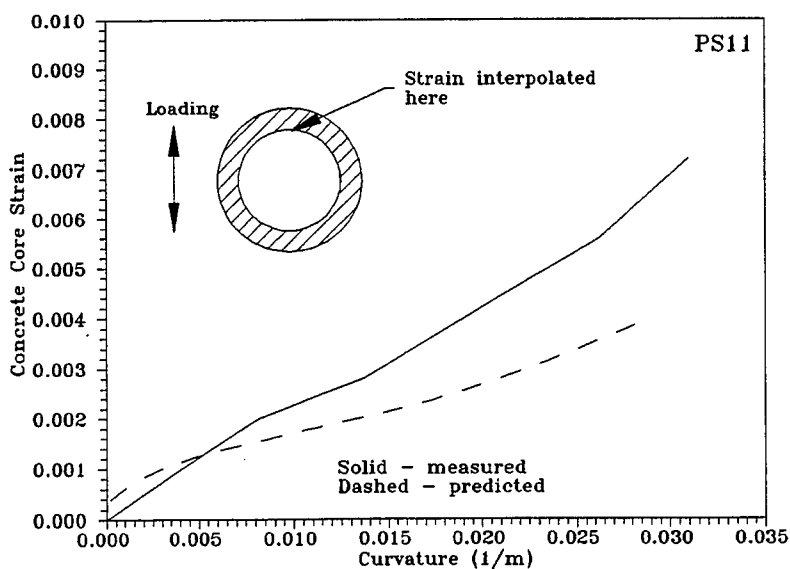


Fig. 6.1.5: Interpolated critical section core strain envelope vs. curvature for hollow pile shaft test unit PS11, push cycles (heavy reinforcement, plastic hinge confined)

Fig. 6.1.6 shows moment-curvature hysteresis loops for PS11, taken at the longitudinal midpoint. They show fairly good agreement as regards the overall envelope response.

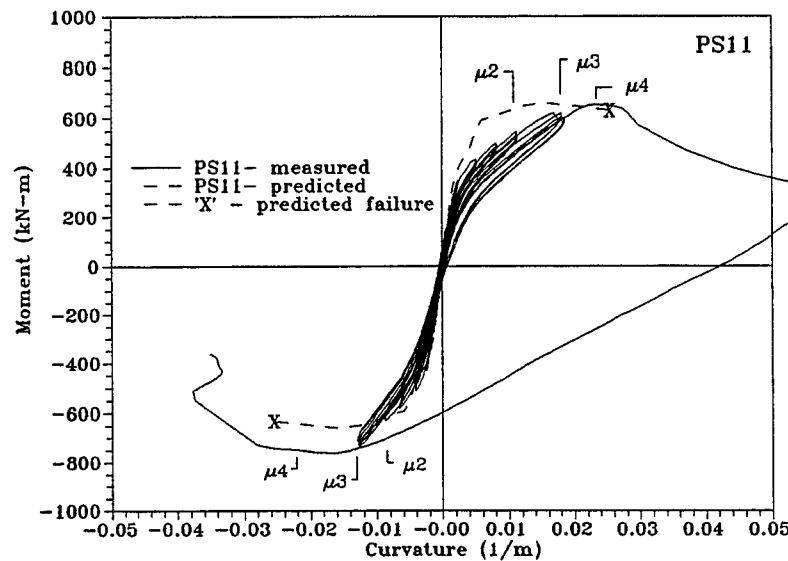


Fig. 6.1.6: Moment-curvature hysteresis loops at longitudinal midpoint, hollow pile PS11 (heavy reinforcement, plastic hinge confined)

Curvature profiles for PS11 are shown in fig. 6.1.7, and show generally good agreement through the test; the large concentration of curvature at failure is notable.

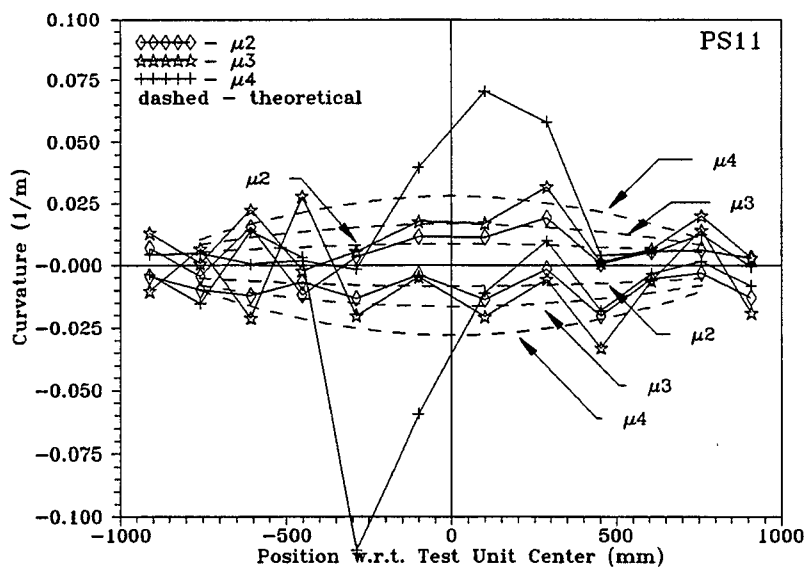


Fig. 6.1.7: Curvature profiles, hollow pile PS11 (heavy reinforcement, plastic hinge confined)

Confining steel strains are shown in fig. 6.1.8, and see, to indicate some mobilization of the confining steel in the later stages of the test. One peak is ≈ 200 mm south of longitudinal midpoint, where, as discussed above, initial failure occurred. The other major peak (left-hand-most in fig. 6.1.8) did not correlate with any significant damage seen during the test, or in the post-mortem.

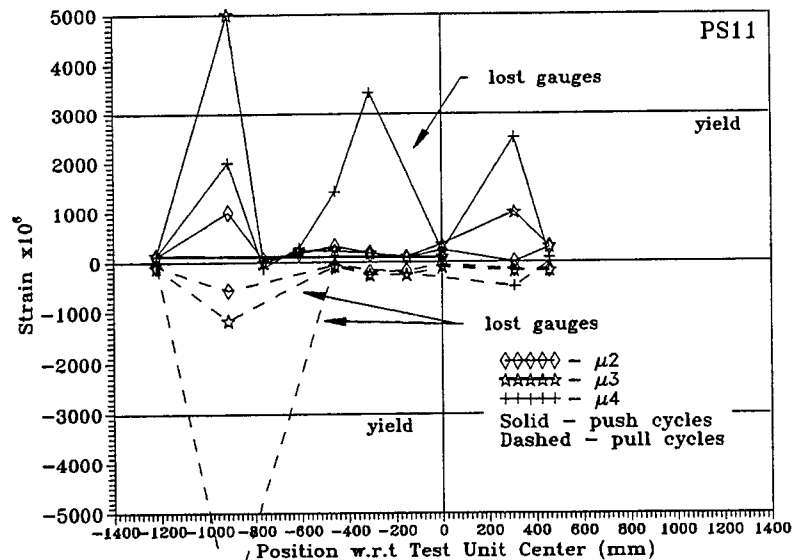


Fig. 6.1.8: Confining steel strain, hollow pile test unit PS11 (plastic hinge confined, heavy reinforcement)

Sadly, little can be said concerning the shear steel strains (fig. 6.1.9) in PS11, as most of the gauges were inoperative. A peak may be developing at $\mu=2$ which would correlate to one seen in the confining steel strains in fig. 6.1.8.

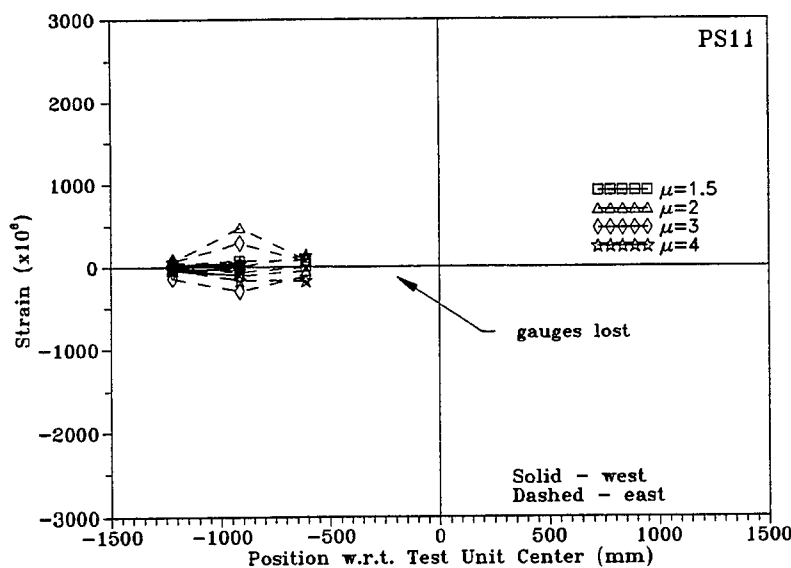


Fig. 6.1.9: Shear steel strain, hollow pile PS11 (heavy reinforcement, plastic hinge confined)



6.2 PS12 (medium reinforcement, plastic hinge unconfined)

Visual examination of PS12 during the test showed flexural cracking to begin at a load (i.e., end reaction) of 150 kN, and to have spread through the loading area through cycling at $\mu=1$. Flexural cracking was eventually noted over half of the length of the pile (from quarter-point to quarter-point). The cracks reached mid-section depth at $\mu=1.5$. Most of the cracking observed after $\mu=1.5$ consisted of extensions to existing cracks. It should be noted that, because of the relatively high degree of prestressing (compressive) force in the section, extensive flexural cracking was neither expected, nor seen.

Inclined extensions to existing cracks, indicating the development of shear cracking, were first observed at $\mu=2$ in the outboard portion of the loaded area (i.e., at loading points 'A' and 'E' of fig. 3). Shear cracking moved toward the longitudinal midpoint as the test progressed.

Incipient spalling was first observed at the peak of the first pull cycle (second half-cycle) at $\mu=3$, at the longitudinal midpoint.



Fig. 6.2.1: Hollow pile PS12, compression zone failure (medium reinforcement, plastic hinge unconfined)





Fig. 6.2.2: Hollow pile PS12, buckled prestressing tendons (medium reinforcement, plastic hinge unconfined)

The demise of PS12 took place on the way to $\mu=4$, by means of a sudden and total failure of the compression zone. Failure was extremely violent; sizable bits of spall were thrown up to 6 meters from the pile. Spalling of the shell was over an area roughly rhomboidal in shape, with a longitudinal dimension of ≈ 600 mm, and a transverse extent of more than half the circumference of the shaft. The failure exposed the reinforcing steel and prestressing tendons in this area; all of the tendons in the compression zone were buckled, some individual strands through a sharp bend of nearly 90° over ≈ 150 mm (which was approximately twice the spacing of the transverse steel spirals; the spiral that straddled the buckled strand seemed to have yielded). Buckled tendons were seen over nearly one-half of the circumference of the shaft (fig. 6.2.3).



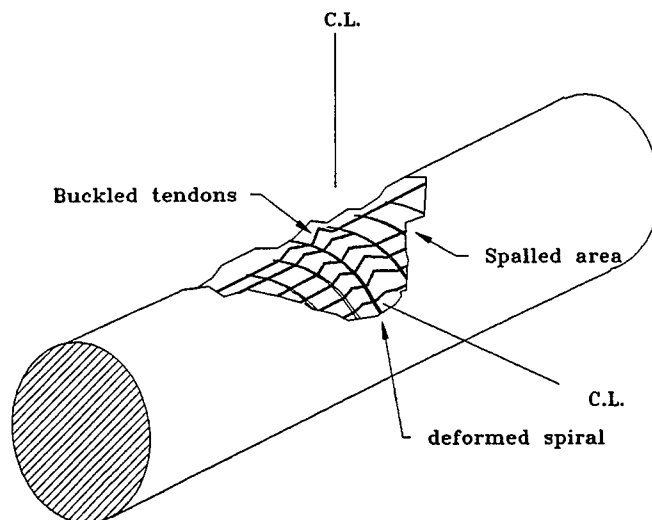


Fig. 6.2.3: Spalling and tendon buckling on hollow pile test unit PS12 (medium reinforcement, plastic hinge unconfined)

It had been anticipated that PS12 would fail at this point; the original test plan was to carry out one full cycle at $\mu=4$ (as had been done with PS11). After the failure described above, no continued cycling was possible; there really wasn't much left to test.

The force-deflection loops for PS12 are shown in fig. 6.2.4. PS12 reached its peak strength at $\mu=3$, with failure occurring just before the attainment of $\mu=4$. Failure was sudden, explosive, and catastrophic, with a complete loss of lateral load capacity. Also, the axial load dropped by over 10% at failure.

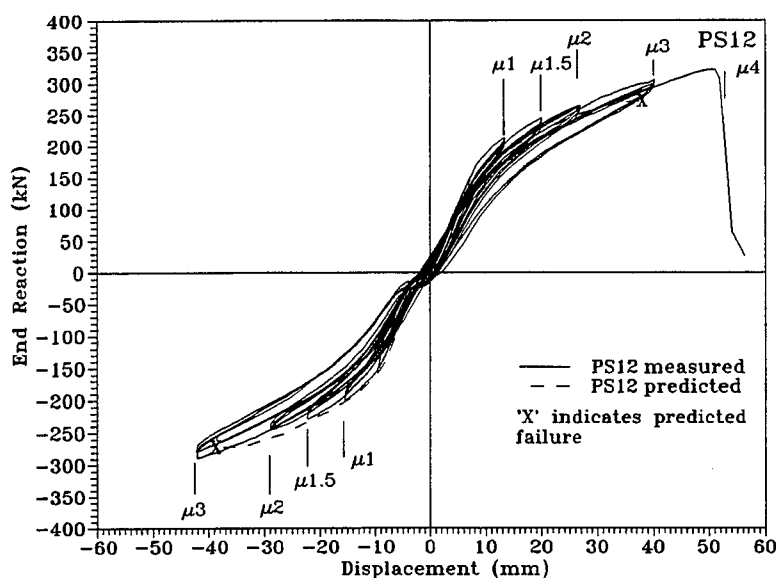


Fig. 6.2.4: Force-displacement hysteresis loops for hollow pile shaft test unit PS12 (medium reinforcement, plastic hinge unconfined)

Predicted force-deflection also appears on fig. 6.2.4. This prediction takes into account the P- Δ effect. The prediction agreed well with the experimental results; overall displacement exceeded predictions, and maximum strength was very slightly in excess of that predicted.

Our current theoretical approach assumes that a hollow section should fail catastrophically when the concrete strain in the inner core reaches a value of $\epsilon=0.004$, the nominal maximum strain for unconfined concrete (it should be noted that this figure is generally considered to be conservative). Fig. 13 shows a comparison of measured vs. predicted core strain at the critical section; the curves can be seen to show reasonable agreement. The core strain of PS12 clearly exceeded the nominal value of 0.004; the maximum was about 0.0057

Post-mortem examination of the test unit showed that the pile wall in the compression zone was spalled all the way through; its remains could be easily prised out by hand.

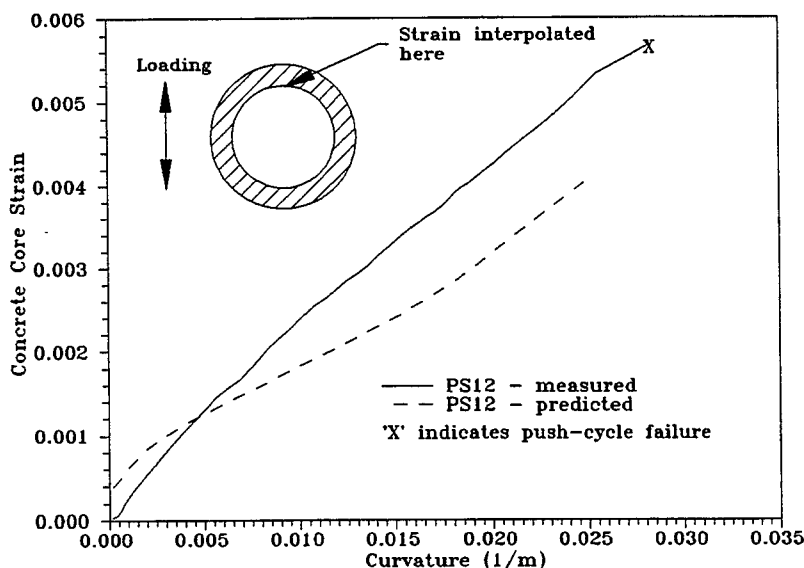


Fig. 6.2.5: Interpolated critical section core strain envelope vs. curvature for hollow pile shaft test unit PS12, push cycles (medium reinforcement, plastic hinge unconfined)

The measured moment-curvature data (fig. 6.2.6) agrees relatively well with that predicted for the section as regards overall moment and curvature capacities; a somewhat stiffer response through the early stages of the inelastic range was predicted than was observed, particularly in the push direction.

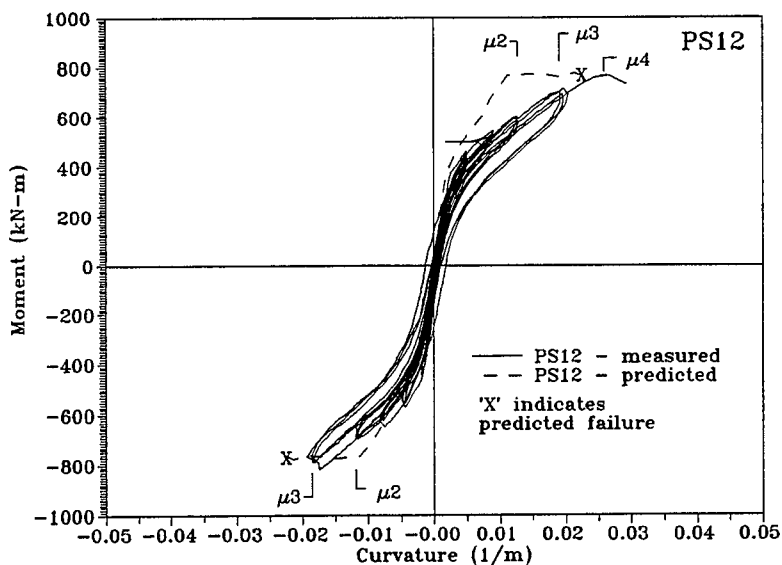


Fig. 6.2.6: Moment-curvature hysteresis loops at longitudinal midpoint, hollow pile PS12 (medium reinforcement, plastic hinge unconfined)

Curvature profiles for PS12 are shown in fig. 6.2.7; they show a relatively well-balanced spread in increasing curvature through the terminal level of ductility, and good agreement with prediction.

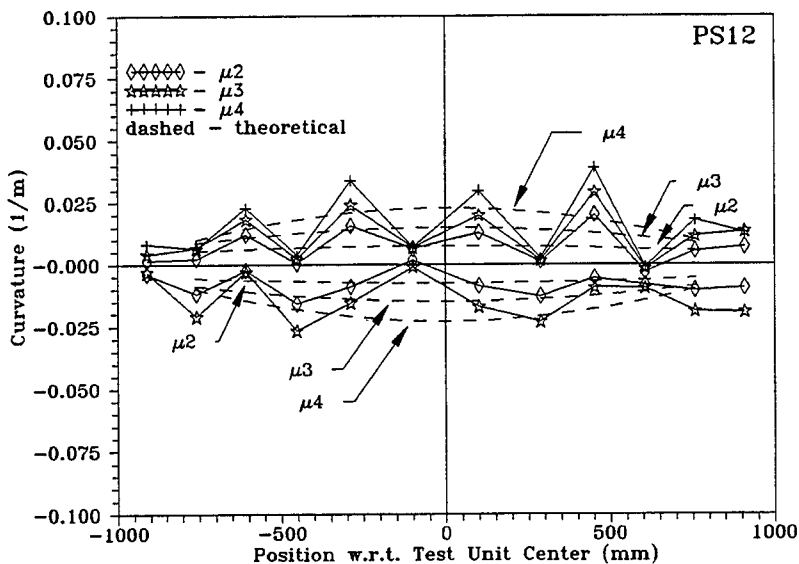


Fig. 6.2.7: Curvature profiles, hollow pile PS12 (medium reinforcement, plastic hinge unconfined)

Confining steel strains for PS12 are shown in fig. 6.2.8. They show the development of some incipient yielding of the transverse reinforcement during the pull to $\mu=3$.

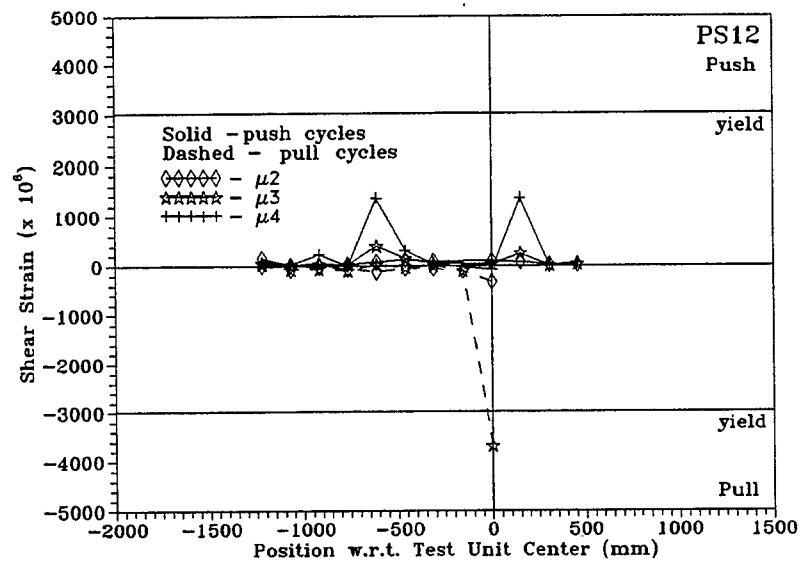


Fig. 6.2.8: Confining steel strains, hollow pile PS12 (medium reinforcement, plastic hinge unconfined)

Shear steel strain is shown in fig. 6.2.9, and indicates little mobilization of that mechanism.

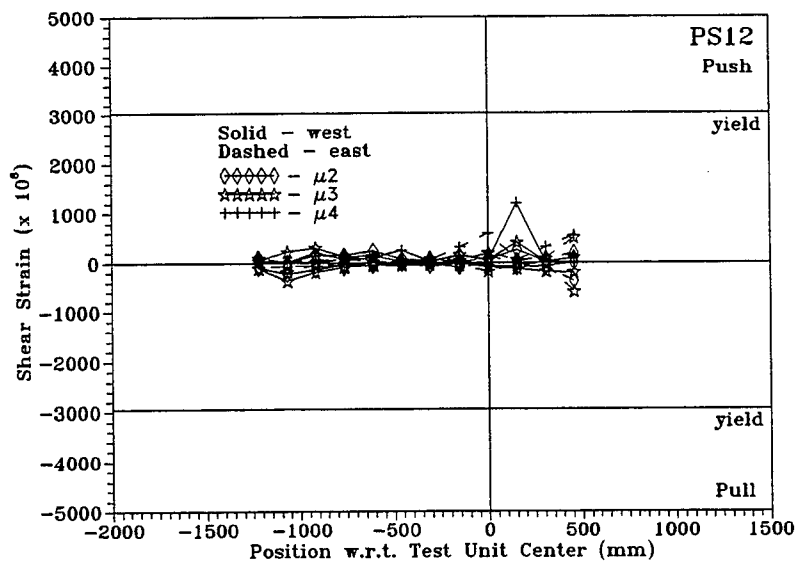


Fig. 6.2.9: Shear steel strain, hollow pile PS12 (medium reinforcement, plastic hinge unconfined)

6.3 PS13 (medium reinforcement, plastic hinge unconfined, dowels in p.h. region)

The first flexural cracks in PS13 were seen at the longitudinal midpoint of the pile at $\mu \approx 1$, and spread through (and beyond) the loading area by the end of the test. The pattern of flexural cracks eventually covered a length slightly greater than three meters ($\approx 5D$). Only minor shear cracking was observed through the loading area; onset was at $\mu = 1.5$. Some shear cracks turned past the nominal 45° inclination to lie almost parallel with the pile's long axis. In contrast to PS12, however, incipient crushing in the push-cycle compression zone was observed at the peak of the third push cycle at $\mu = 2$ (observe from the figure above that failure came shortly before $\mu = 2.5$). Very little incipient crushing or spalling was observed on the pull-cycle compression side..

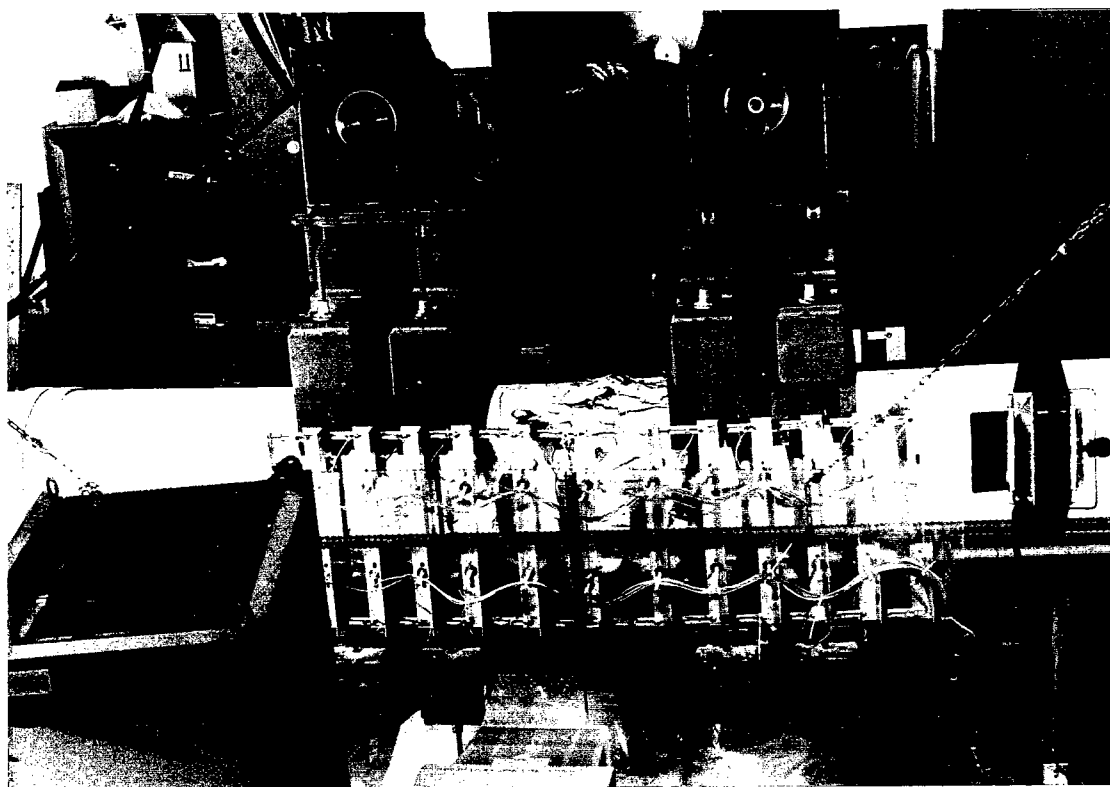


Fig. 6.3.1: Initial compression failure of hollow pile PS13 (medium reinforcement, plastic hinge unconfined, dowels in p.h. region)

The failure of PS13 during the first push excursion to $\mu = 2.5$ was milder than that which took place in the testing of PS12, because the earlier damage described above softened the structure; the presence of longitudinal Grade 60 bars in the plastic hinge region also played a role in that they could make up some of the compressive capacity lost when the shell's integrity was lost. The push-cycle failure just short of $\mu = 2.5$ resulted in a drop of well over 50% in lateral force, but only 10% of the axial load was dropped. Since the pull-cycle compression zone was still intact, it was decided to complete the second half-cycle at $\mu = 2.5$. This resulted in an extremely violent failure; all of the lateral force was unloaded, and nearly 50% of the axial load was immediately dropped. The axial load continued to drop as it was unloaded into axial deformation (shortening) in the badly-



damaged plastic hinge region, but the full extent of the drop was not recorded, as the test was manifestly over and it was desired that the axial load system be powered down.

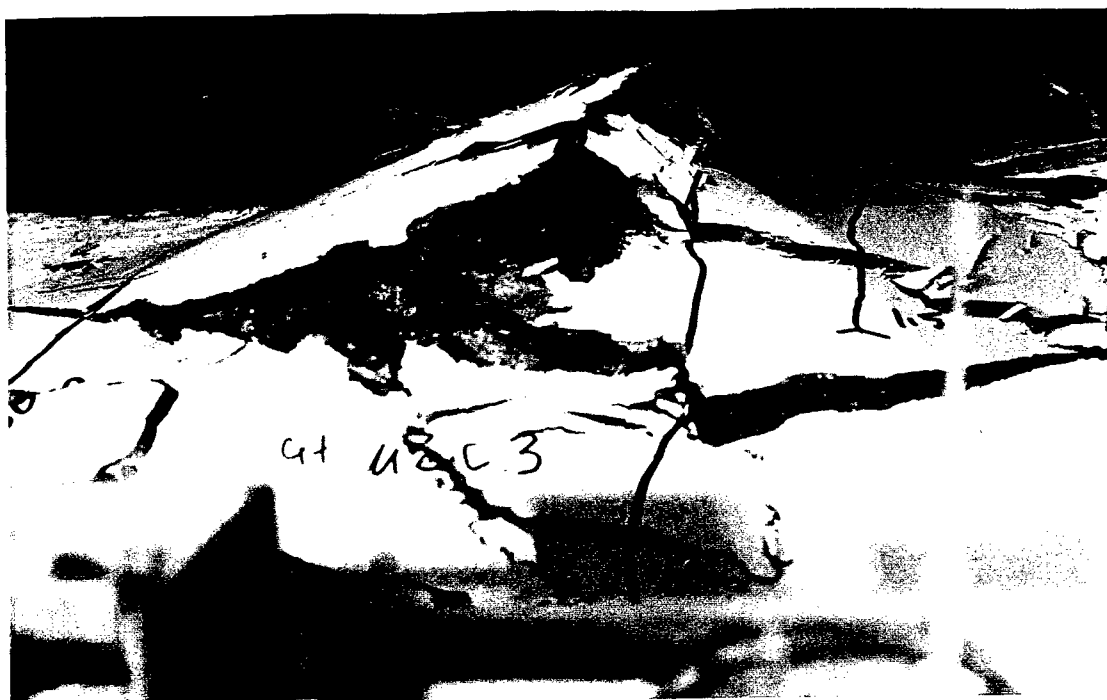


Fig. 6.3.2: Close-up of compression zone failure, hollow pile PS13 (medium reinforcement, plastic hinge unconfined, dowels in p.h. region)

Post-mortem examination of PS13 was generally similar to that of PS12; however, there was rather more strand buckling, and the nonprestressed longitudinal bars suffered buckling and low-cycle fatigue failures.

Shown in fig. 6.3.3 are the force-deflection hysteresis loops for PS13. It is clear that the addition of nonprestressed reinforcement to PS13's plastic hinge region did not delay the onset of failure, or render it less catastrophic. Failure can clearly be seen just past $\mu=2$, with a large drop in lateral capacity. Because the failure mechanism was restricted to the concrete compression zone, it was to be expected that a second half-cycle (a reversal of load to the same displacement) would show symmetrical behavior to failure; this is seen in fig. 6.3.3. The predicted force-displacement curve agreed very well with the results.



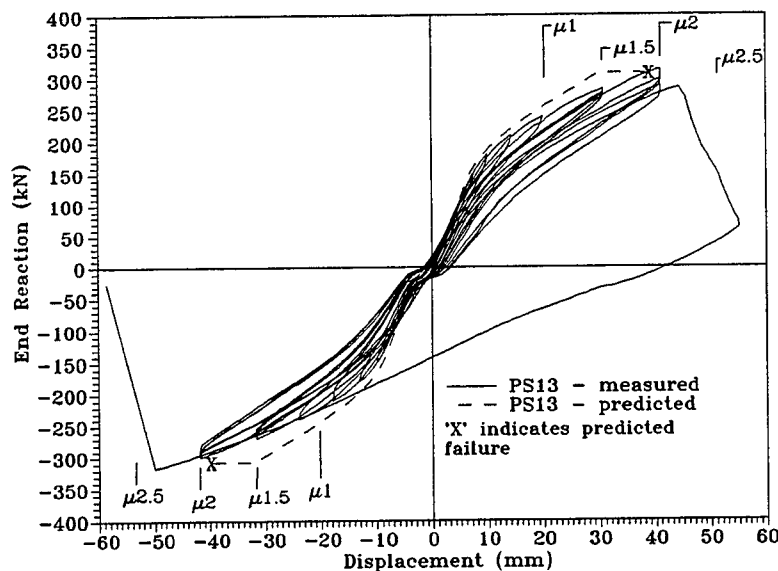


Fig. 6.3.3: Force-deflection hysteresis loops for hollow pile shaft test unit PS13 (medium reinforcement, plastic hinge unconfined, dowels in p.h. region)

Shown in fig. 6.3.4 is a comparison of interpolated core strain versus curvature for PS13. The results are similar to those given for PS12 (which was similar in all respects save the presence of the Grade 60 reinforcement to the plastic hinge region), though PS12 reached somewhat higher core compression strain and critical-section curvature before failure. It was expected that the curvatures seen in PS13 would be less than those observed in PS12, as the greater amount of tension steel in PS13 would have shifted the neutral axis toward the center of the pile. The lower concrete strains may be a function of the nonprestressed longitudinal bars' inelastic deformation degrading the integrity of the shell; recall that incipient spalling was seen during cycling at $\mu=2$, with failure at $\mu \approx 2.5$.

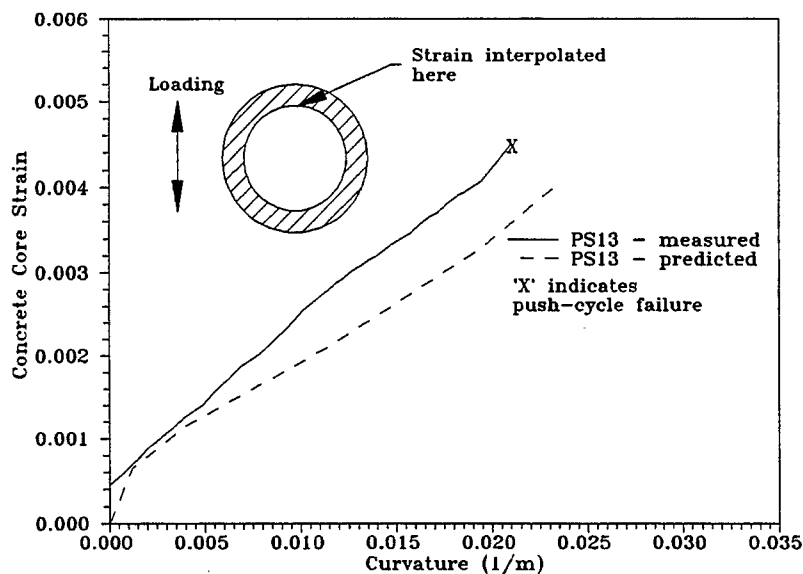


Fig. 6.3.4: Interpolated critical section core strain envelope vs. curvature for hollow pile shaft test unit PS13, final push cycle (medium reinforcement, plastic hinge unconfined, with mild steel dowels in p.h. region)

Moment-curvature data corresponds relatively well to the predicted values, though the overall flexural strength was somewhat lower than predicted; also, the ultimate curvature capacity was slightly lower than that predicted; some softening may have occurred because the steps between ductility increments were quite small (i.e., $\mu=1.5$ to $\mu=2$ to $\mu=2.5$).

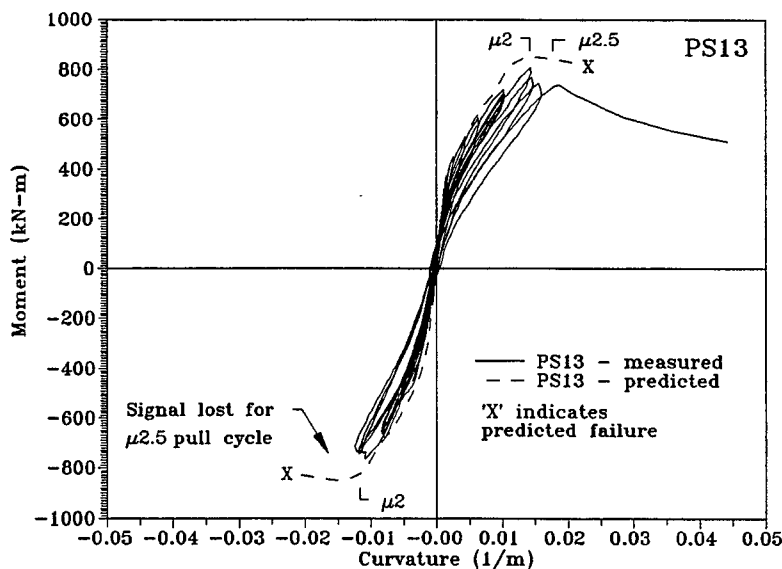


Fig. 6.3.5: Moment-curvature hysteresis loops at test unit midpoint, hollow pile PS13 (medium reinforcement, plastic hinge unconfined, with mild steel dowels in p.h. region)

The curvature profiles (fig. 6.3.6) show excellent agreement with the predicted curvature levels up to $\mu=2$. The spikes at $\pm \mu=2.5$ are an interesting illustration of the relatively soft push-cycle failure, contrasted with the very sharp and violent pull-cycle failure, which resulted in a more widespread destruction of the plastic hinge region.

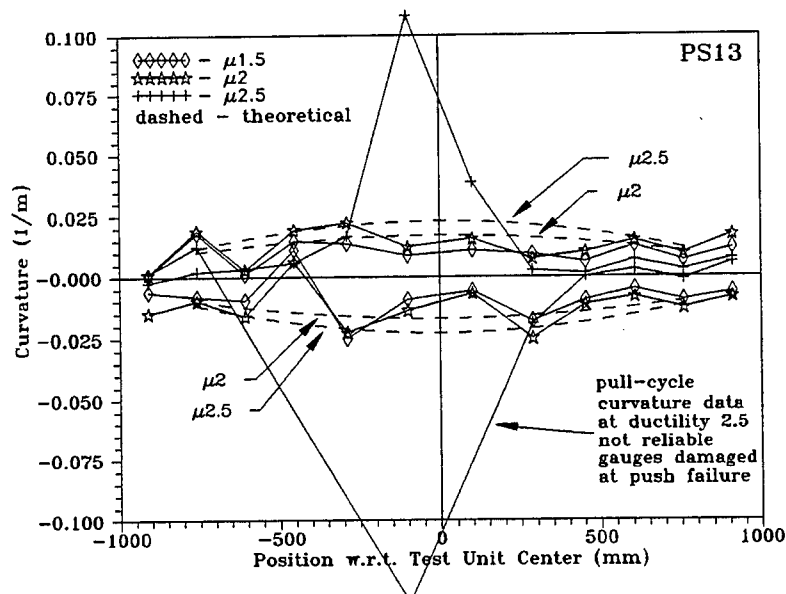


Fig. 6.3.6: Curvature profiles, hollow pile PS13 (medium reinforcement, plastic hinge unconfined, with mild steel dowels in p.h. region)

Fig. 6.3.7 shows confining steel strains in PS13, and show the yielding of the spirals as the push-cycle plastic hinge initiated the pile's failure on the way to $\mu=2.5$.

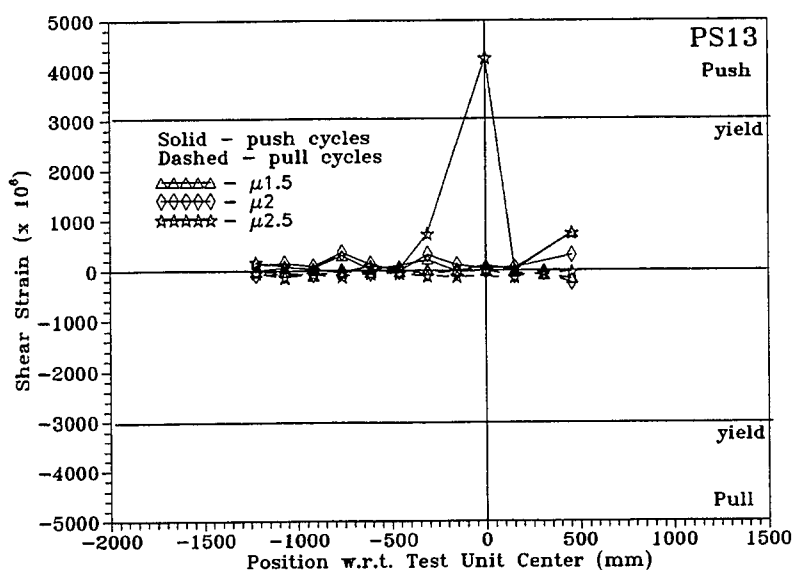


Fig. 6.3.7: Confining steel strains, hollow pile PS13 (medium reinforcement, plastic hinge unconfined, with mild steel dowels in p.h. region)

Shear steel strains for PS13 are shown in fig. 6.3.8; inelastic strains associated with the development of the push-cycle hinge, and the pile's incipient failure, are clear. The localized area of damage is also notable; in areas immediately adjacent to the hinge, there was clearly no requirement for the mobilization of the steel shear-resisting mechanism.

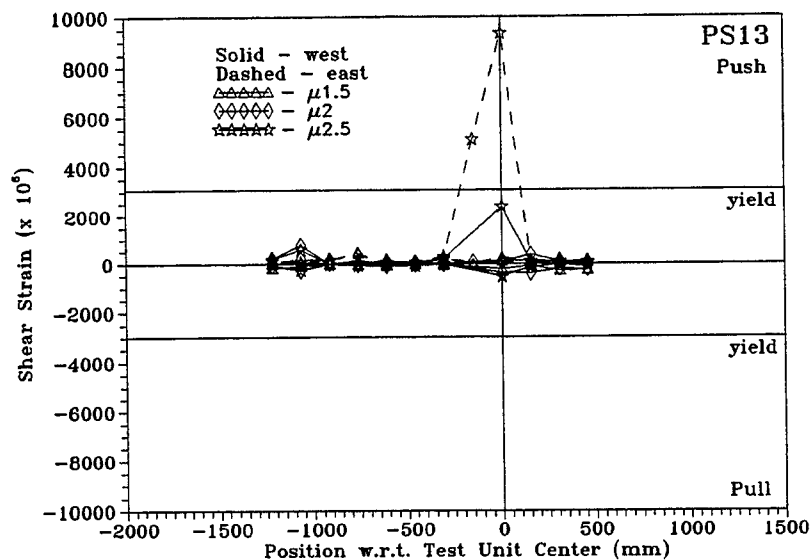


Fig. 6.3.8: Shear steel strains, hollow pile PS13 (medium reinforcement, plastic hinge unconfined, with mild steel dowels in p.h. region)

6.4 PS14 (light reinforcement, plastic hinge confined)

Observation of PS14 during the test, and examination of the data, did not show evidence of rupture of either tendons or transverse steel. Visual examination of PS14 during and after the test did show that plasticity was evident over a fairly wide area ($\approx 1D$), centered just north of the test unit's longitudinal midpoint, close to the northern edge of saddle 'C' (ref. fig. 3). Incipient crushing began here (beneath the central saddle; 'C' in fig. 3.1) at $\mu=3$, but no significant crushing or spalling was seen until failure; indeed, removal of the load fixtures showed the pile to be cosmetically fairly sound. The cover was cracked and fissured, but almost none fell away with removal of the central set of saddles. (After testing of solid prestressed piles PS9 and PS10, great chunks of cover came away when the central saddles were removed.)

Very few cracks were seen or expected, because of the high degree of prestressing in the section. Flexural cracks were seen up to 2 m from the longitudinal midpoint of the test unit, indicating a significant degree of curvature to that point. Flexural cracking was first observed at $\mu=1$; shear cracking was first seen at $\mu=1.5$, and some possible splitting cracks were seen at $\mu=3$.

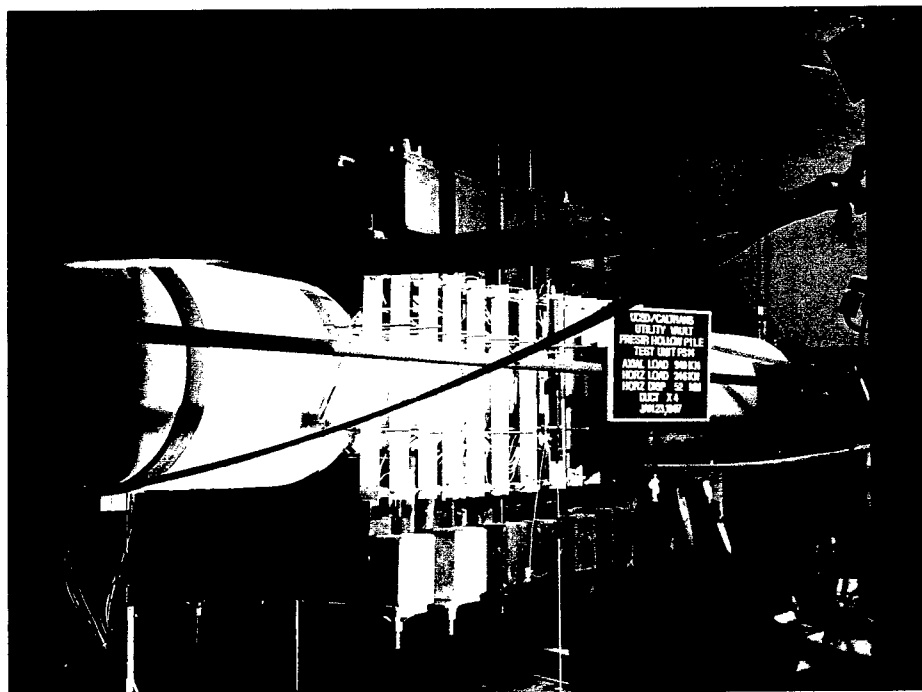


Fig. 6.4.1: Hollow pile PS14 at $\mu=4$ (light reinforcement, plastic hinge confined)

Post-mortem examination of the test unit involved cutting it in half adjacent to the plastic hinge region. This way, the core surface could be examined for crushing and spalling. A band of spalling was seen on the compression side of the section, subtending an angle of slightly over 180° ; this band was at an angle to the pile's longitudinal axis, approximately following the line of the transverse reinforcing spiral. The spalled core was not actually loose; it was held in place by the surrounding material. However, its structural integrity was gone, and very little effort was required to remove spalled pieces of concrete. The spalling and crushing extended all the way through the wall of the section (The damage observed was virtually identical to that shown in fig. 6.1.3). Sectioning the pile also provided confirmation that the Sonovoid™ which was used as the form for the core was totally degraded by its soaking with water.

The force-deflection loops for PS14 are shown in fig. 6.4.2. PS14 reached its peak strength at $\mu=3$, with failure occurring just before the attainment of $\mu=4$. Failure was both sudden and catastrophic, with a dramatic drop in lateral capacity. Also, the axial load dropped by over 10% at failure.



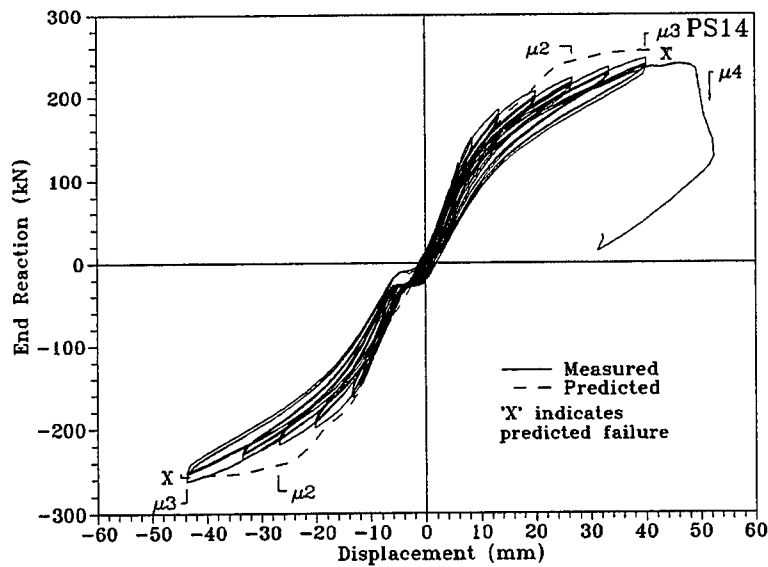


Fig. 6.4.2: Force-displacement hysteresis loops for hollow pile shaft test unit PS14 (light reinforcement, plastic hinge confined)

Predicted force-deflection also appears on fig. 6.4.2. This prediction takes into account the P- Δ effect. The prediction agreed relatively well with the experimental results; ultimate displacement was slightly in excess of that predicted.

As mentioned previously, current design practice assumes that a hollow section should fail catastrophically when the concrete strain in the inner core reaches a value of $\epsilon = 0.004$, the nominal maximum strain for unconfined concrete (it should be noted that this figure is generally considered to be conservative). Fig. 6.4.3 shows a comparison of measured vs. predicted core strain at the critical section; the curves can be seen to show good agreement. The core strain of PS14 clearly exceeded the nominal value of 0.004; the maximum was close to 0.006

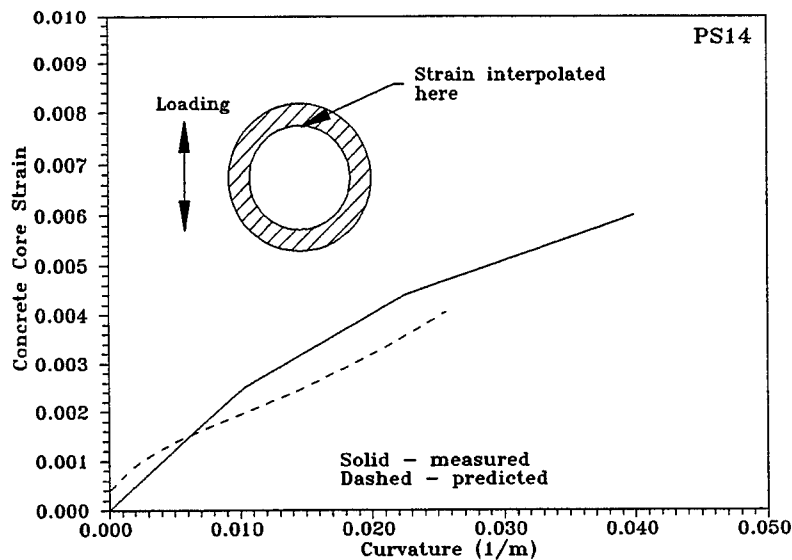


Fig. 6.4.3: Interpolated critical section core strain envelope vs. curvature for hollow pile shaft test unit PS14, push cycles (light reinforcement, plastic hinge confined)

Moment-curvature hysteresis loops for PS14 (fig. 6.4.4) indicate a fairly good agreement with prediction to failure.

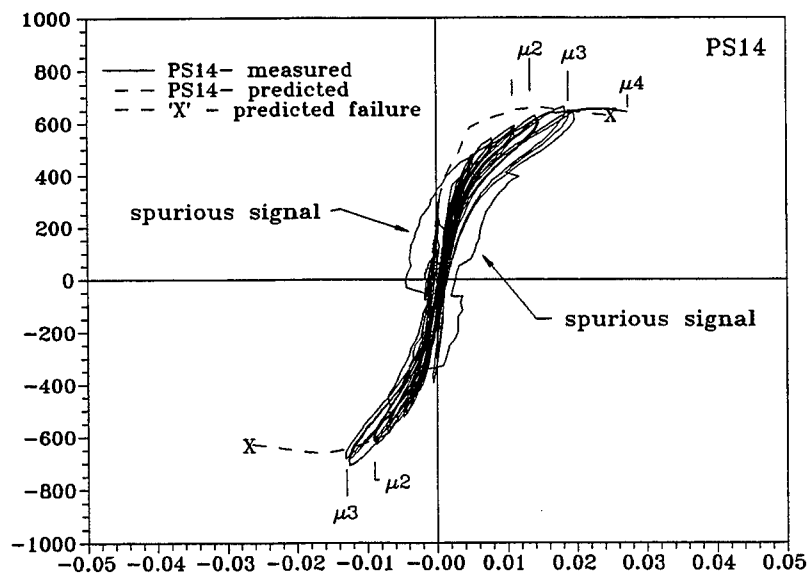


Fig. 6.4.4: Moment-curvature hysteresis loops at longitudinal midpoint, hollow pile PS14 (light reinforcement, plastic hinge confined)

Curvature profiles for PS14 are shown in fig. 6.4.3, and show good agreement with predicted curves until the large 'spike' in curvature at failure (also, recall that PS14 was not taken to $\mu=4$ in pull).

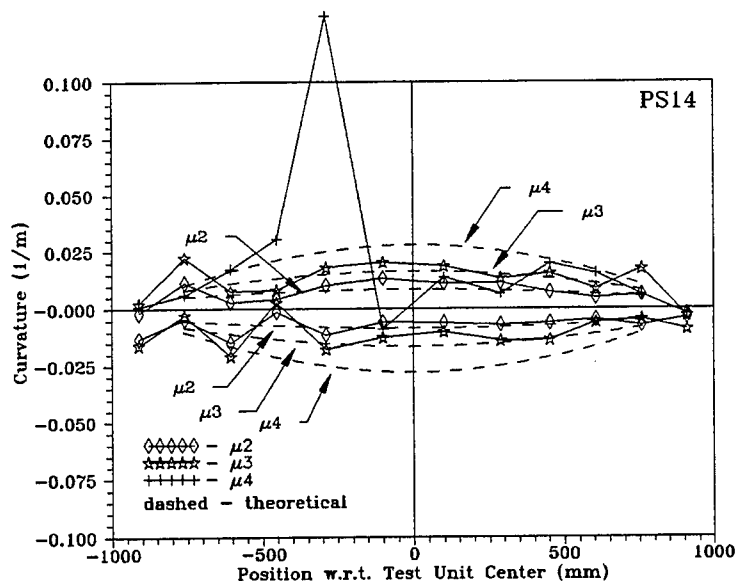


Fig. 6.4.5: Curvature profiles, hollow pile PS14 (light reinforcement, plastic hinge confined)

Fig. 6.4.6, showing PS14's confining steel strains, indicates some mobilization of the transverse steel in the later stages of the test, at $\mu=2$ (and perhaps $\mu=3$; that gauge was lost at this point) in the last pull cycle, and $\mu=4$ in the last push cycle.

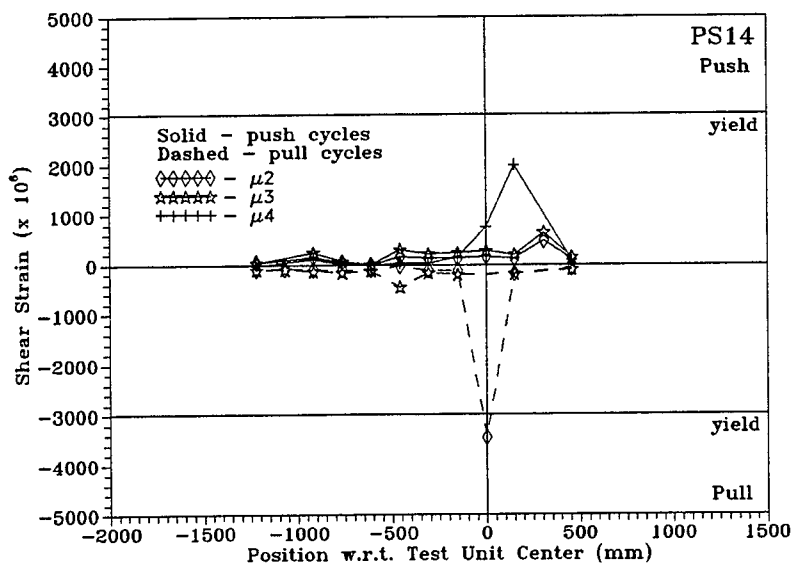


Fig. 6.4.6: Confining steel strains, hollow pile PS14 (light reinforcement, plastic hinge confined)

Shear steel strains for PS14 are shown in fig. 6.4.7, and indicate that there was not much mobilization of the steel truss mechanism to the very end of the test.

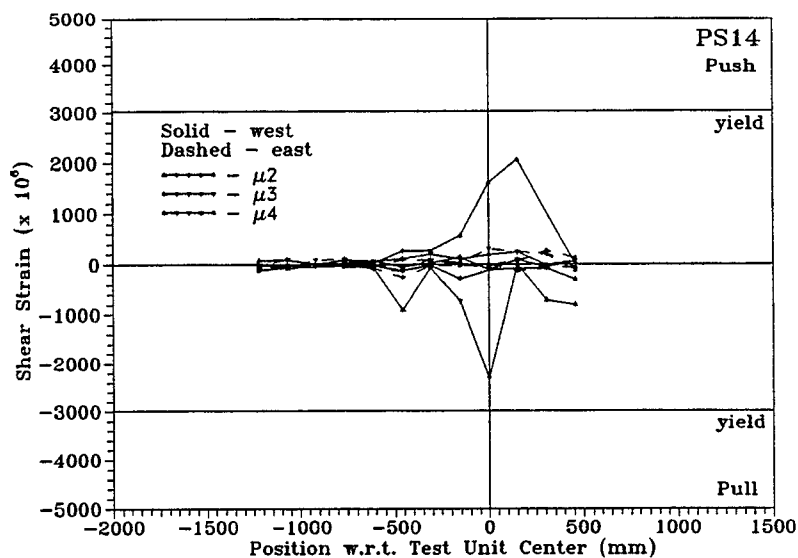


Fig. 6.4.7: Shear steel strain, hollow pile PS14 (light reinforcement, plastic hinge confined)

6.5 Comparisons Between the Hollow Pile Tests

The hollow pile tests described above best lend themselves to comparison in three areas: first, the effect of varying levels of transverse reinforcement; second, the presence or absence of nonprestressed longitudinal steel in the plastic hinge region; third, the effect of external confinement to the plastic hinge region.

In examining the effects of varying levels of transverse reinforcement, we may see this most directly by comparing the most heavily reinforced pile (PS11, nominal $\rho_t=0.03$) with that which was the most lightly reinforced (PS14, nominal $\rho_t=0.01$). Both piles were loaded in a similar manner; their plastic hinge regions did receive external confinement. Their comparative force-displacement envelopes are shown in fig. 6.5.1; there is clearly no difference in the maximum level of ductility attained. Nor could any have reasonably have been expected, as the exposed face of the core could withstand only a compression strain similar to that of unconfined concrete.

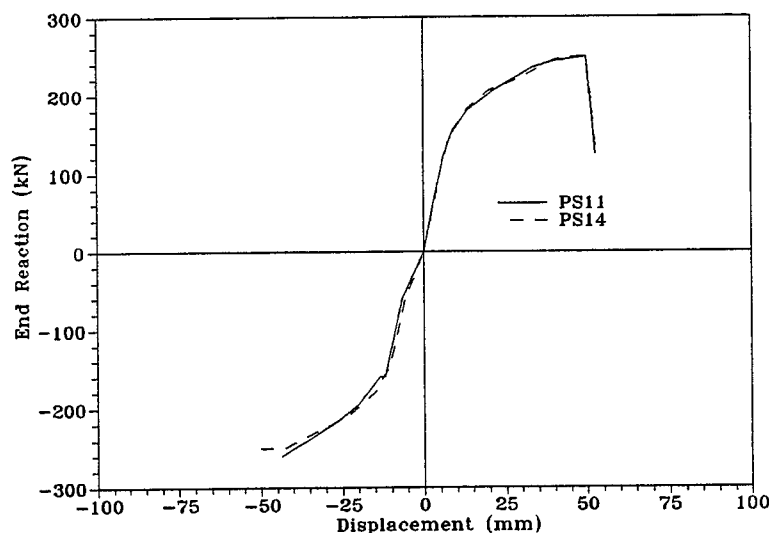


Fig. 6.5.1: Comparison of force-displacement envelopes, PS11 (heavy transverse reinforcement) and PS14 (light transverse reinforcement)

Core strain versus curvature for PS11 and PS14 is shown in fig. 6.5.2; again, there is no substantive difference that may be attributed to different levels of transverse reinforcement.

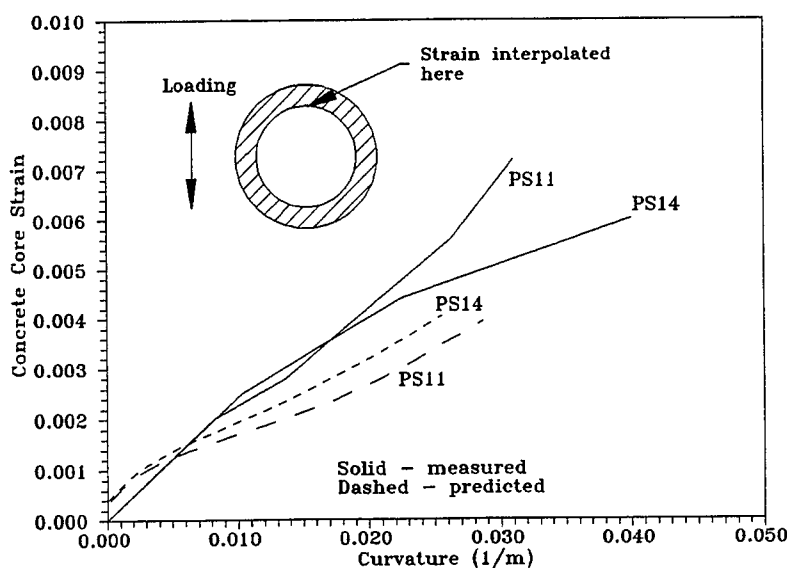


Fig. 6.5.2: Comparison of core strain, PS11 (heavy transverse reinforcement) and PS14 (light transverse reinforcement)

The effect of adding nonprestressed mild steel longitudinal reinforcement to the plastic hinge region may be seen by comparing PS12 and PS13; these piles were identical in structural details and loading (plastic hinge unconfined), save that PS13 had eight #4 Grade 60 bars reinforcing its plastic hinge region.

Examination of the force-displacement envelopes (fig. 6.5.3) shows that while flexural strength in PS13 was slightly greater than in the unreinforced PS12, displacement ductility capacity was slightly lower.

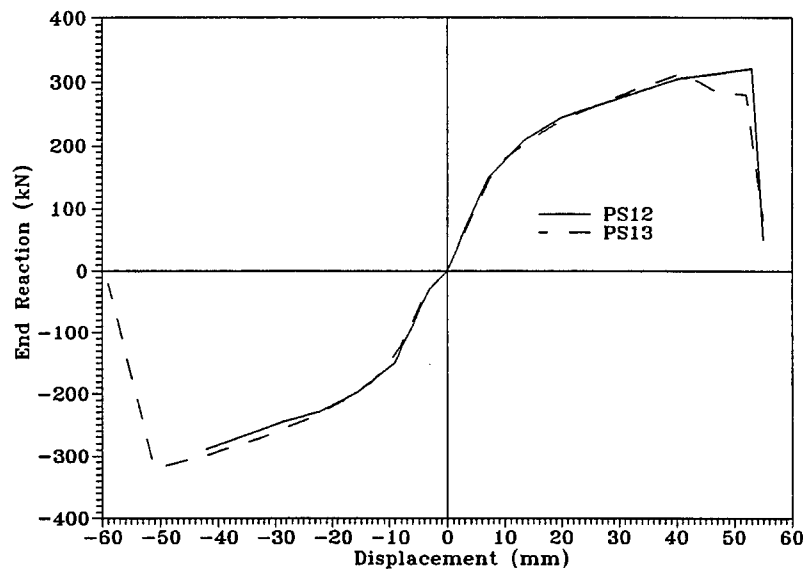


Fig. 6.5.3: Comparison of force-displacement envelopes, PS12 (no nonprestressed reinforcement in plastic hinge region) and PS13 (with nonprestressed longitudinal reinforcement in plastic hinge region)

The failure mechanism was the same (spalling through the shell, and subsequent loss of the compression zone), and so the ultimate displacements (governed by maximum sustainable concrete core strain) were similar. It bears repeating, however, that the curvatures seen in PS13 were lower than those in PS12, as the tension steel would have shifted to neutral axis deeper into the section, away from the compression side. This is seen in fig. 6.5.4.

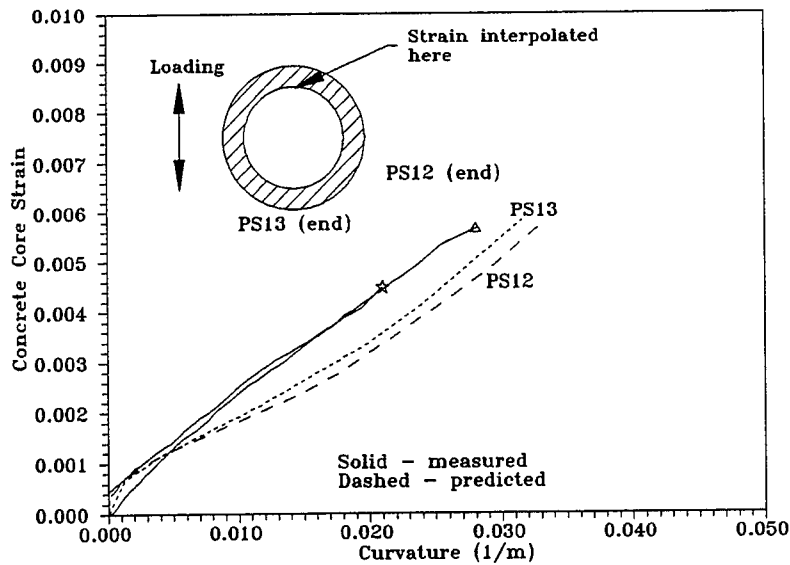


Fig. 6.5.4: Comparison of core strain, PS12 (no nonprestressed reinforcement in plastic hinge region) and PS13 (with nonprestressed longitudinal reinforcement in plastic hinge region)

The effect of external confinement to the plastic hinge region may best be described in quantitative terms, in reference to the force-displacement hysteresis loops of all four hollow pile test units (fig. 6.5.5). There was no difference in the ultimate displacements achieved (or in the maximum sustainable core strain, see fig. 6.5.2 and 6.5.4 above); however, the failures that occurred when external confinement was present were somewhat 'softer'; the drop in lateral load was generally somewhat less, and the destruction to the shell not quite as total, since the cover was constrained to remain more or less in place, and could still bear some load (this was seen to a more pronounced degree in the higher post-spalling flexural strength plateaus of the solid piles, PS9 and PS10, in which external confinement was modeled).

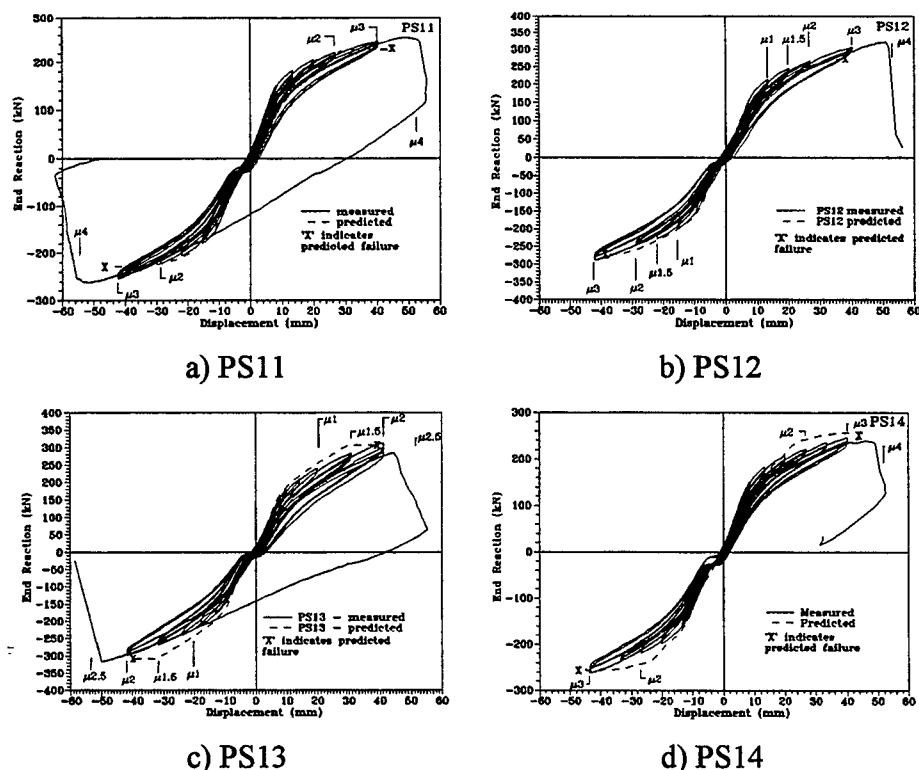


Fig. 6.6.5: Comparison of force-displacement hysteresis loops for hollow piles PS11 - PS14: a) PS11 (heavy reinforcement, plastic hinge confined); b) PS12 (medium reinforcement, plastic hinge unconfined); c) PS13 (medium reinforcement, plastic hinge unconfined, Gr. 60 bars in p.h.); d) PS14 (light reinforcement, plastic hinge confined)

Shown in table 6.1 are the predicted and observed plastic hinge lengths for PS11 through PS14. The unconfined examples (PS12 and PS13) show a somewhat greater plastic hinge length than do the confined examples; the absence of confinement allowed damage, and thus large curvatures, to spread over a wider area.

TABLE 6.1: PREDICTED VS. ACTUAL PLASTIC HINGE LENGTH, HOLLOW PILES PS11-14

Test Unit	External Confinement of Hinge	Predicted l_p (diameters D)	Actual l_p (diameters D)	$\frac{l_{p, actual}}{l_{p, pred.}}$
PS11	Yes	1.15D	0.876D	0.76
PS12	No	1.04D	1.40D	1.35
PS13	No	0.88D	1.45D	1.65
PS14	Yes	1.16D	1.11D	0.96

Shown in table 6.2 is a comparison of predicted and measured ultimate displacements for PS11 through PS14. Since the anticipated failure mechanism was based

on a conservative analysis (an ultimate core concrete strain of 0.004), it would be expected that the actual displacements achieved would be in excess of prediction, and so they are.

**TABLE 6.2: PREDICTED VS. ACTUAL ULTIMATE DISPLACEMENT,
HOLLOW PILES PS11-14**

Test Unit	External Confinement of Hinge	Predicted Δ_{ult}	Actual Δ_{ult}	$\Delta_{ult, exp.} / \Delta_{ult, pred.}$
PS11	yes	45 mm	52 mm	1.15
PS12	no	38 mm	52 mm	1.37
PS13	no	39 mm	45 mm	1.15
PS14	yes	44 mm	50 mm	1.14



7. RESULTS, GLASSFIBRE-JACKETED SOLID PRESTRESSED PILES

7.1 PS15 (jacket uncut, plastic hinge confined)

Visual examination of PS15 during the test showed no distress in the jacket up to $\mu=3$. At the peak of the first push cycle at this level of load, concurrent with the drop in lateral capacity mentioned in the paragraph above, a load 'pop' was heard, and a crack flexural crack opened in the jacket under the central load frame (loading point 'C' in fig. 3.1). This crack reached PS15's midline at $\mu=4$, and went past the midline at $\mu=6$ (the singular is used for clarity; there was actually symmetrical cracking from push and pull loading). At high ductilities ($\mu=6$ and above) powdered concrete was seen to issue from the flexure crack at the bottom of PS15 as it opened, indicating crushing of the concrete. Few other cracks were seen (or expected), because of the presence of the jacket and the high degree of prestressing in the section. Onset of some minor flexural cracking outboard of the jacket was noted at $\mu=1$; no extensions or new cracks in the outboard area were seen after $\mu=3$. Failure (in both directions) was by (audible) tendon rupture.

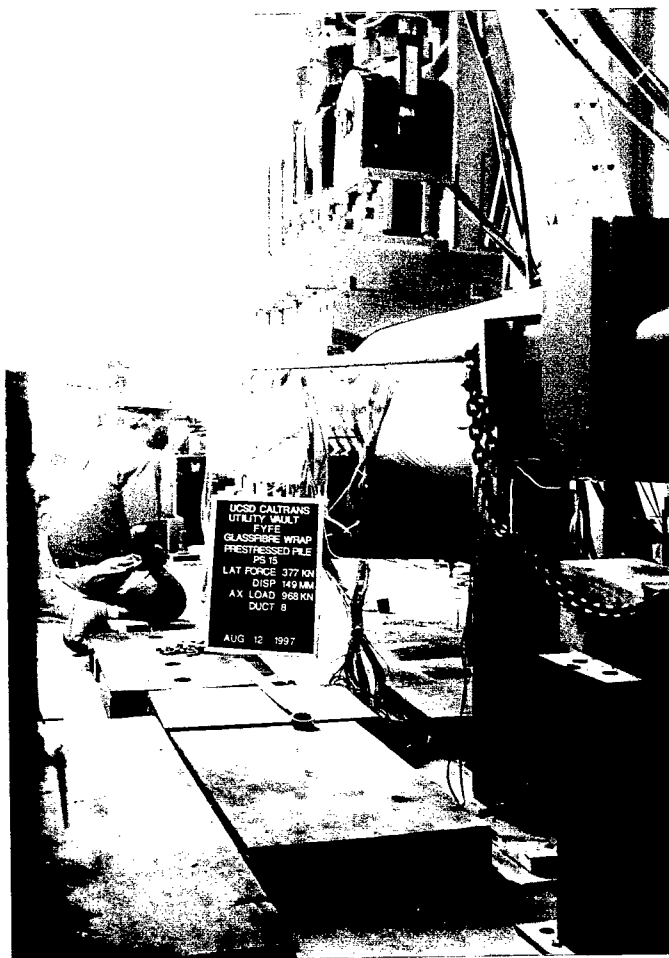


Fig. 7.1.1: Pile shaft test unit PS15 at $\mu=8$ (low reinforcement, glassfibre-jacketed, jacket uncut)





Fig. 7.1.2: Flexure crack in jacket of PS15 (low reinforcement, glassfibre-jacketed, jacket uncut)

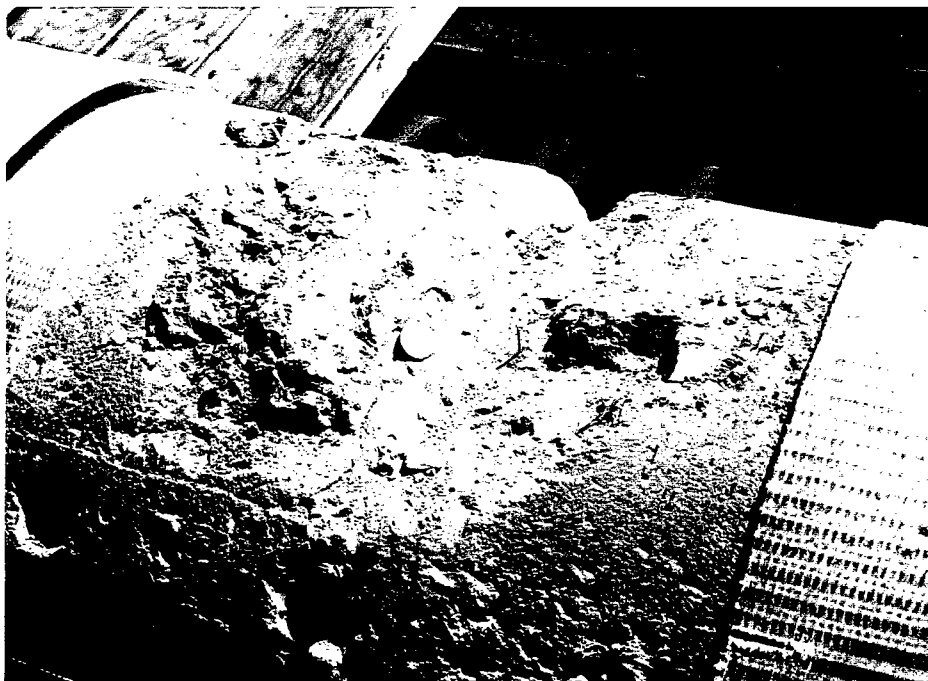


Fig. 7.1.3: Jacket removed from PS15's pull-cycle compression side; note "notch" where concrete has been crushed and has powdered away (low reinforcement, glassfibre-jacketed, jacket uncut)





Fig. 7.1.4: Ruptured and buckled tendons, PS15 (low reinforcement, glassfibre-jacketed, jacket uncut)

Postmortem examination of PS15 showed a very concentrated damage region, of a length $\approx D/8$. One tendon on the push-cycle tension side was seen to be ruptured, with two adjacent tendons buckled (the buckling is assumed to have occurred during the last pull cycle (to $\mu=8$)).

The force-deflection loops for PS15 are shown in fig. 7.1.5. Peak strength was reached at $\mu=3$, at which point there was a small (less than 10%) but noticeable drop in capacity. Higher levels of ductility showed a gradual $P-\Delta$ degradation, and there was significant degradation at repeated cycling at a given ductility at and above $\mu=3$. Failure occurred at $\mu \approx 7.6$ in both push and pull (positive and negative loading). The push-cycle failure was gradual, but still brought a drop of $\approx 30\%$ of lateral capacity; the pull-cycle failure was abrupt and fairly violent.



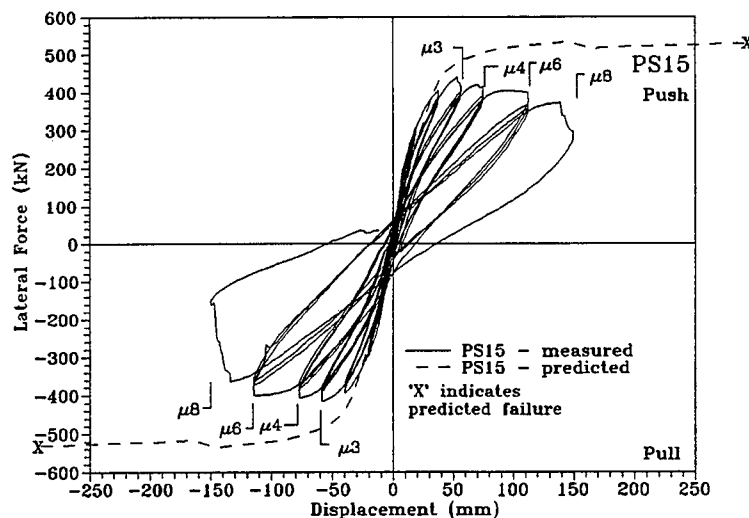


Fig. 7.1.5: Force-displacement hysteresis loops for pile shaft test unit PS15 (jacket uncut, plastic hinge confined)

Predicted force-deflection also appears on fig. 7.1.5. This prediction takes into account the P- Δ effect, and the effect of the longitudinal reinforcement provided by the jacket (along with the loss of that reinforcement when the tensile strains exceeded 5% at the extreme tension fibre, which is the ultimate design strain for the epoxy matrix). The prediction agreed relatively well with the experimental results only through the early stages of loading; the ultimate lateral capacity was considerably lower than predicted, and PS15 showed less ductility than was expected.

The development of the single large flexural crack at midpoint indicated that a large amount of curvature was being concentrated there, and resulting in a very condensed plastic hinge. This is shown clearly in figs. 7.1.6 and 7.1.7, which are moment-curvature hysteresis loops and curvature profiles, respectively. While the overall flexural strength of PS15 was considerably below that predicted, the average midpoint curvature reached at failure was close to the prediction. However, as seen in fig. 7.1.5, the total displacement was considerably less than predicted. Fig. 7.1.7 shows dramatically how curvature was concentrated into the center of the pile.

The conclusion at which one arrives from examination of the curvature data, when coupled with the underperformance of the predicted displacement, is that the jacket, when mobilized, imposed high clamping pressures on the prestressing tendons, and thus preserved the integrity of the tendon-concrete bond. In the areas in which the bond was compromised (i.e., at deep flexural cracks), a high degree of strain was demanded of the tendon over a very short length. These large localized strains soon exceeded the tendon capacity, resulting in total rupture (in contrast with the tendon failure of PS10, in which case the tendons failed on a wire-by-wire basis, with no tendon completely fracturing).

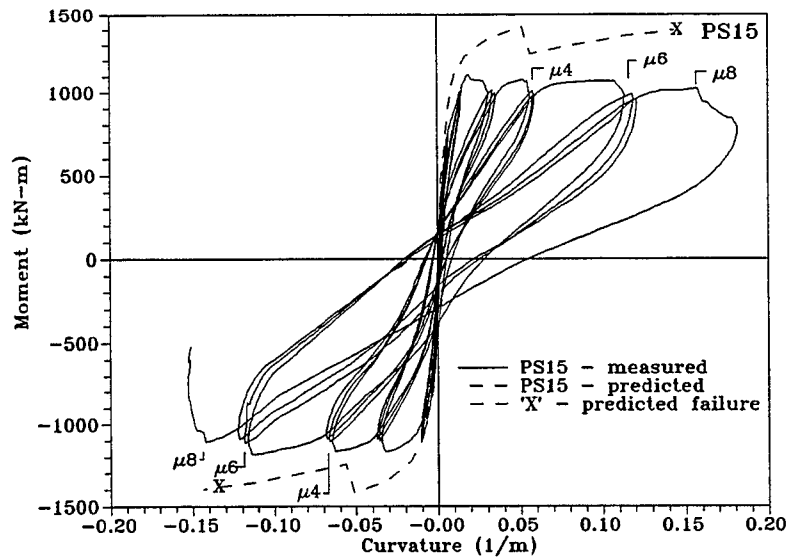


Fig. 7.1.6: Moment-curvature hysteresis loops (at longitudinal midpoint) for glassfibre-jacketed prestressed pile PS15 (jacket uncut, plastic hinge confined)

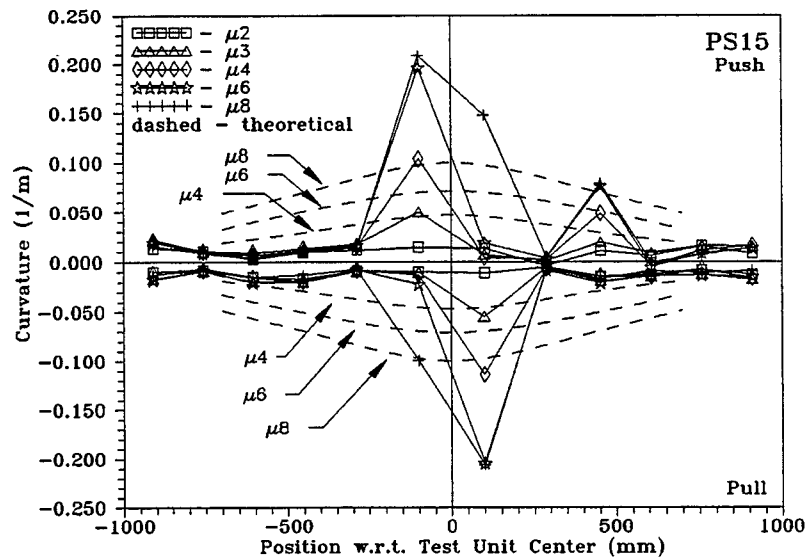


Fig. 7.1.7: Curvature profiles for glassfibre-jacketed prestressed pile PS15 (jacket uncut, plastic hinge confined)

Shown in fig. 7.1.8 are confining strains (that is, transverse strains of the compression surface) for the glassfibre jacket. These can be seen to have progressed smoothly upward through the loading history, but remained well below the nominal ultimate value of $\approx 1.9\%$; no indication was seen that the jacket was in serious distress in the transverse direction. (The flexure cracking across the longitudinal axis was not confined solely to the butt joint between the two wraps, and did not seem to favor that

'route'; the selva edges of the wraps were in such proximity that a substantial thickness of epoxy joined them, and was able to carry considerable tensile forces.)

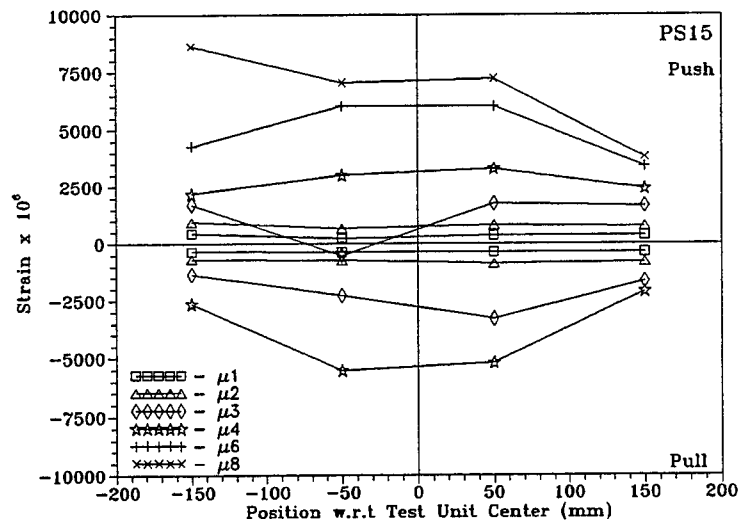


Fig. 7.1.8: Glassfibre jacket confining strains, PS15 (jacket uncut, plastic hinge confined)

The confining steel strains shown in fig. 7.1.9 indicate that there was some mobilization of the spirals late in the test (in push), consistent with the condensed plastic hinge mentioned and illustrated above. Shear steel (fig. 7.1.10) experienced little mobilization. This was expected, as the shear capacity of this section was considerably in excess of the shear forces imposed (see fig. 3.20).

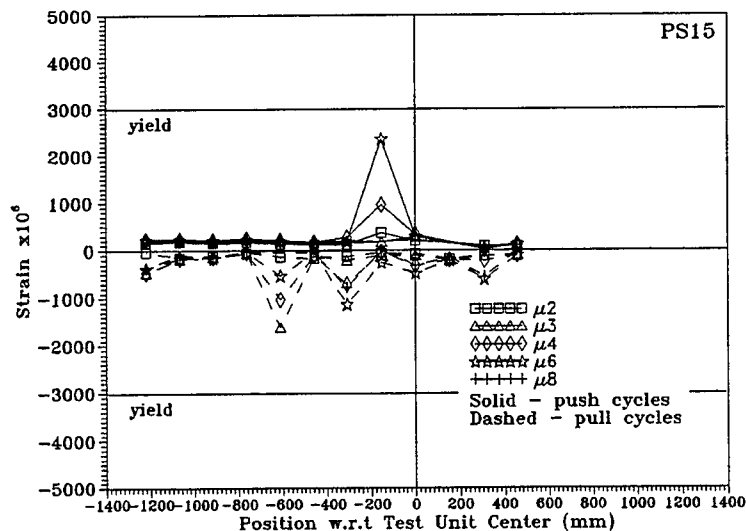


Fig. 7.1.9: Confining steel strains, glassfibre-jacketed prestressed pile PS15 (jacket uncut, plastic hinge confined)

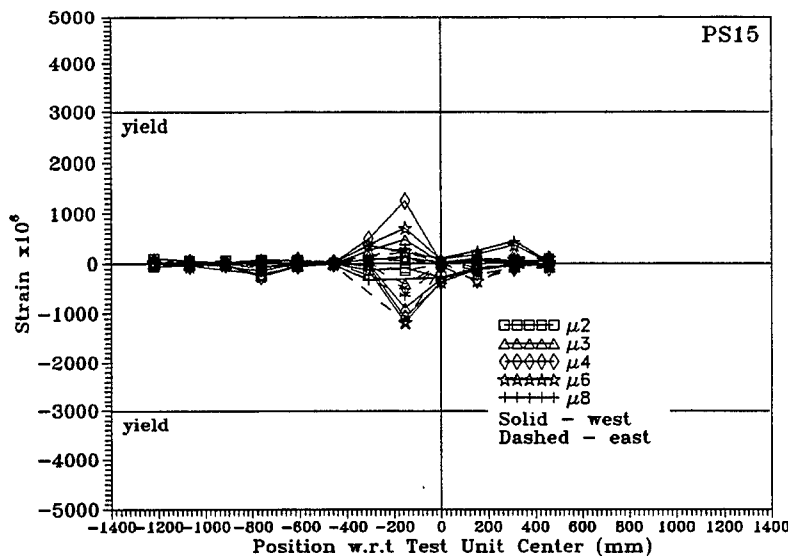


Fig. 7.1.10: Shear steel strains, glassfibre-jacketed prestressed pile PS15 (jacket uncut, plastic hinge confined)

7.2 PS16 (glassfibre jacket with transverse cuts, plastic hinge unconfined)

While the glassfibre jacket was intended to provide transverse reinforcement only, the epoxy alone has a 90° off-axis strength of about 10% of the main axis strength. It was felt that this may have contributed to the somewhat undesirable performance of PS15, and so the jacket of PS16 was slit transversely (over the full circumference) every 152 mm, over a span of 900 mm, centered on the pile's longitudinal centerline. The slits were cut through the full jacket thickness, to remove any additional longitudinal reinforcement.

Instability in the test fixture in the push direction resulted in only one push cycle at $\mu=6$ being completed; after this push displacements were limited to $\mu=3$, and the pull cycles continued on to $\mu=8$, at which point failure occurred.

Flexure cracking was first seen at $\mu=1$, though it was evident from the force-displacement data that the onset was rather earlier (around 200 kN). Very limited flexure cracking was seen outboard of the edges of the wrap, and extended to the test unit's quarter-points. No new cracks, or extensions, were seen in this area after $\mu=4$. No shear cracks were observed.

Failure of PS16 came at $\mu=8$ in pull, at an overall displacement far below that which was predicted. PS16 failed by (very audible) tendon rupture, with a large and sudden decrease in lateral capacity. At least one tendon failed during the first cycle at $\mu=8$; a total of at least five tendons failed through cycling at $\mu=8$. All strands in the failed tendons ruptured; this is similar to PS15 but in contrast to PS10 (with similar transverse reinforcement, but unjacketed), in which no tendon completely failed. Three cycles were completed at the terminal ductility level, but the first one can be said to have caused failure of the pile.

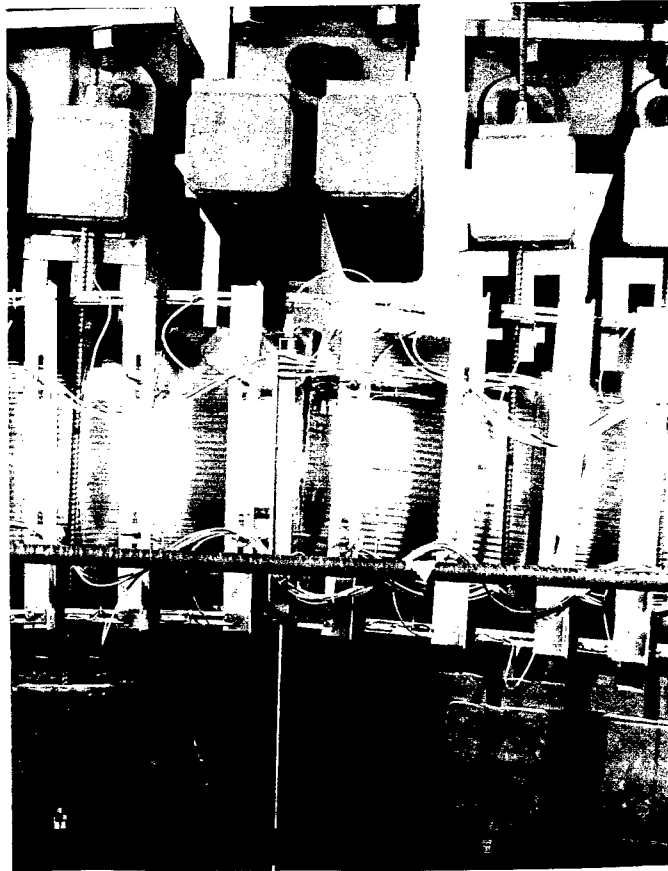


Fig. 7.2.1: Pile shaft test unit PS16 at $\mu=8$, showing flexure crack in jacket (glassfibre jacket with transverse cuts, plastic hinge unconfined)



Fig. 7.2.2: Midline flexural crack in PS16 (glassfibre jacket with transverse cuts, plastic hinge unconfined)



Force-displacement hysteresis loops for PS16 are shown in fig. 7.2.3, and show predicted force-displacement curves. Ultimate displacement achieved was perhaps half of that predicted, and overall flexural strength was somewhat lower as well. The reason for this is that described in the preceding section, for PS15; the glassfibre jacket's confining force imposed a heavy clamping pressure on the prestressing tendons, preserving their bond with the concrete. As a result, high rotations were forced to concentrate where the bond had degraded, at the points of flexural cracking. This resulted in higher-than-forecast localized strain in the tendons, which led to their rupture long before the section was expected to fail.

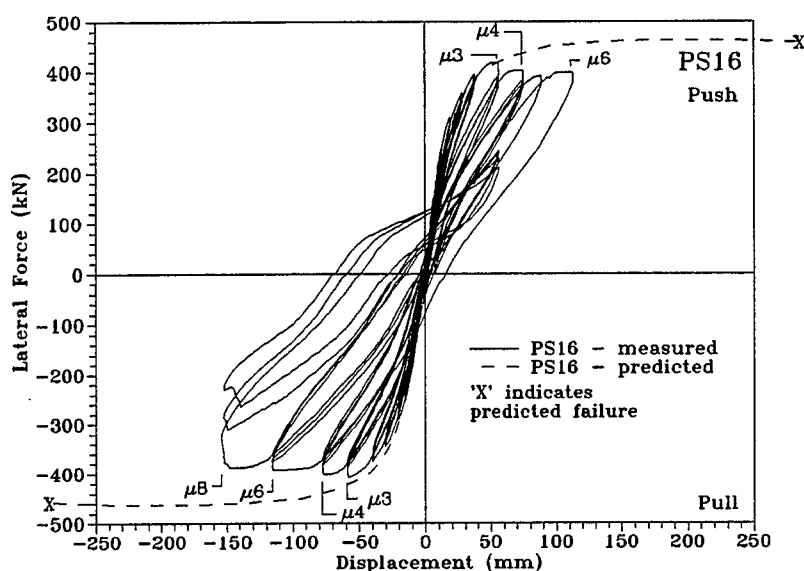


Fig. 7.2.3: Force-displacement hysteresis loops, pile shaft test unit PS16 (glassfibre jacket with transverse cuts, plastic hinge unconfined)

The slitting of the jacket forced flexural cracks at the locations of the slits, and these were first observed to open at $\mu=1$. The centerline slit was, as might be expected, the most active, and concentrated the largest share of curvature through the test (as seen in fig. 7.2.5, the curvature profiles). The outboard slits did open slightly.

The moment-curvature hysteresis loops (fig. 7.2.4) show good agreement with prediction through the lower range of loading, but the softening associated with the development of a very concentrated plastic hinge resulted in lower-than-predicted moment capacity at higher levels of ductility.

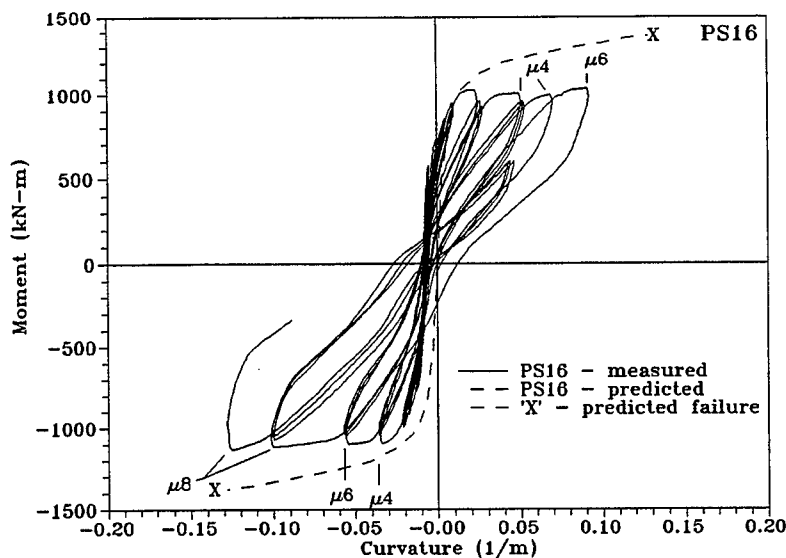


Fig. 7.2.4: Moment-curvature hysteresis loops, PS16 (glassfibre jacket with transverse cuts, plastic hinge unconfined)

The curvature profiles for PS16, fig. 7.2.5, show graphically the development of a very concentrated plastic hinge through the attainment of high localized curvatures on the longitudinal midline.

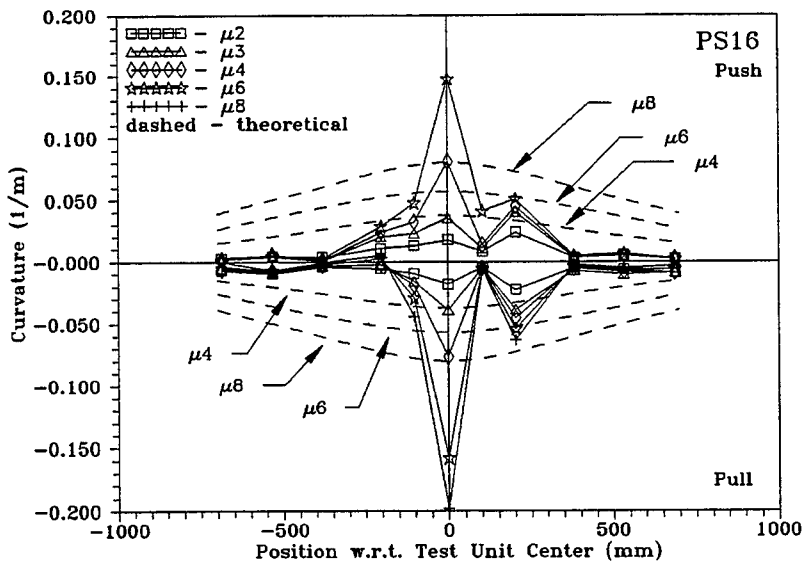


Fig. 7.2.5: Curvature profiles, pile shaft test unit PS16 (glassfibre jacket with transverse cuts, plastic hinge unconfined)

The jacket itself showed no signs of distress through the test. Transverse strains are shown in fig. 7.2.6; they indicate a fairly broad mobilization of the jacket through $\mu=4$, with some concentration at $\mu=6$ and beyond.

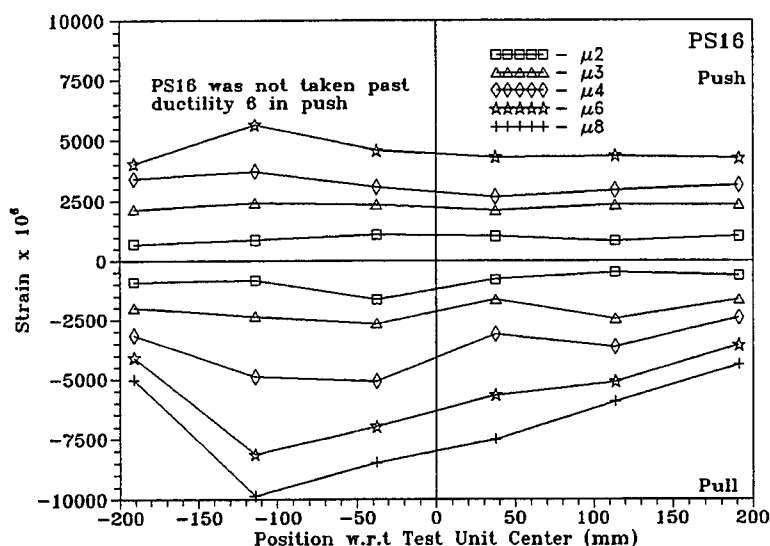


Fig. 7.2.6: Glassfibre jacket strains, PS16 (glassfibre jacket with transverse cuts, plastic hinge unconfined)

Confining steel strains for PS16 are shown in fig. 7.2.7. The unfortunate loss of many of the gauges in the critical region prevents any firm conclusions as to just what was happening to the confining steel, but any possible mobilization does not seem to have been wide in its extent.

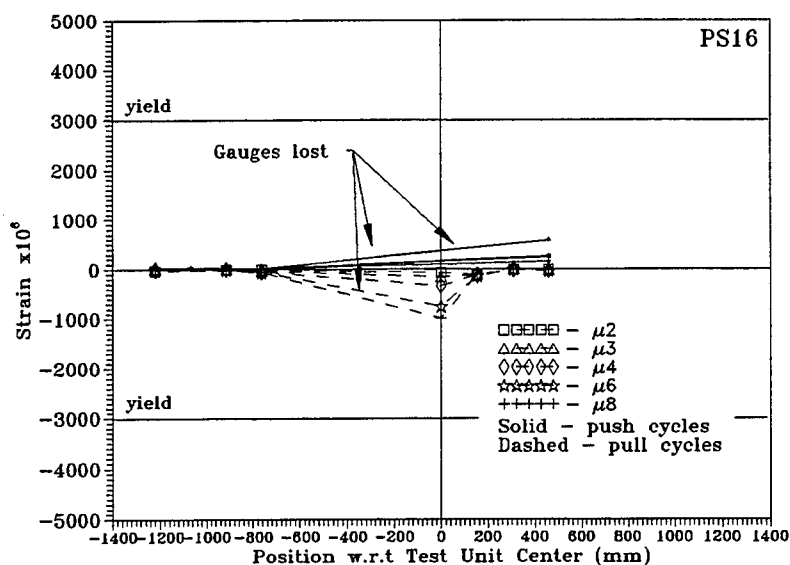


Fig. 7.2.7: Confining steel strains, PS16 (glassfibre jacket with transverse cuts, plastic hinge unconfined)

Shear steel strains for PS16, shown in fig. 7.2.8, indicate that the steel shear-resisting mechanism may have been employed during the final stages of the test ($\mu=6$ and $\mu=8$ pull cycles).

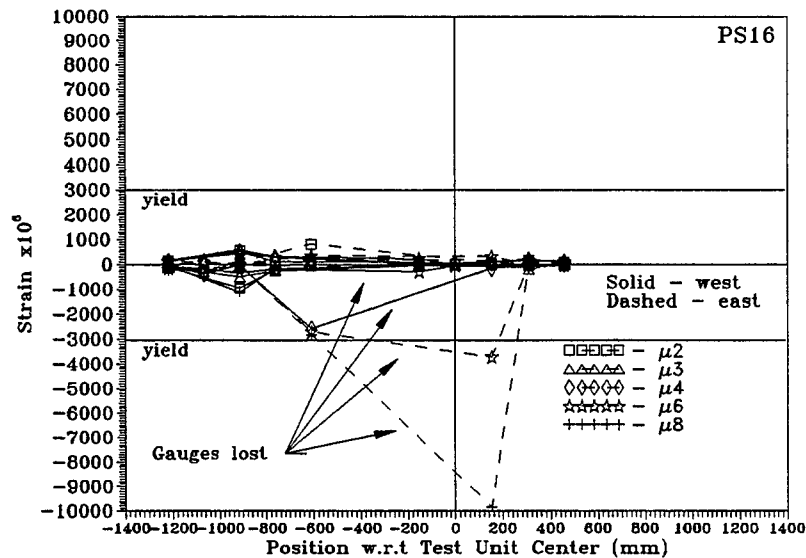


Fig. 7.2.8: Shear steel strains, PS16 (glassfibre jacket with transverse cuts, plastic hinge unconfined)

7.3 Comparisons between PS15, PS16, and PS10 (unjacketed)

As shown by the comparative force-displacement envelopes in fig. 7.3.1, the overall performance of PS16 was very similar to that of PS15. After the testing of PS15, it was thought that the longitudinal reinforcement provided by the jacket was the culprit in condensing the plastic hinge and causing failure at a significantly lower drift angle than was withstood by the unjacketed PS10. However, as the effective contribution of longitudinal reinforcement of the jacket was removed by the transverse cuts in PS16, this was clearly not the case. Rather, it seems that the jacket imposed a significant clamping force on the section, and thus protected the bond between the prestressing tendons and the concrete. Thus, when the initial flexural cracking at the midpoint of the pile caused some localized degradation of the bond, it was a very limited length of tendon that was forced to accommodate the inelastic rotations that would otherwise have been more generously spread over a greater length. The tendon(s) thus affected therefore broke earlier than in PS10 (which survived to $\mu=10$, before failing through tendon rupture).

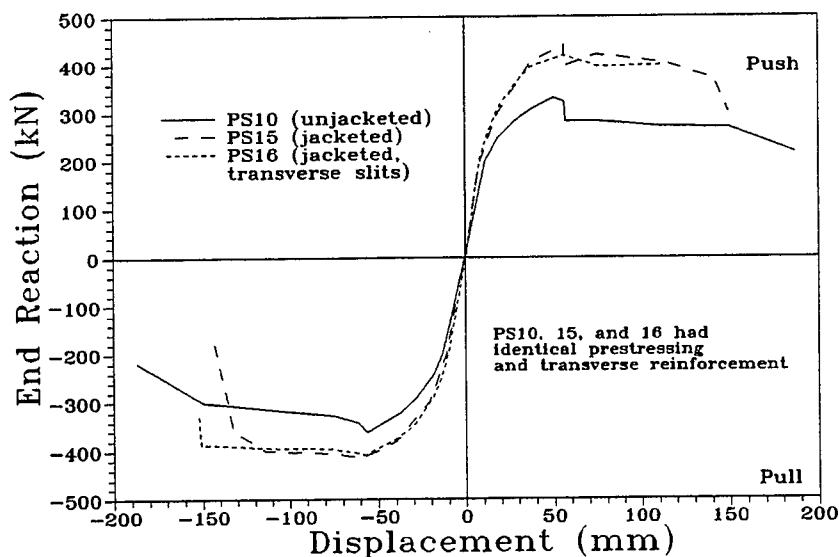


Fig. 7.3.1: Force-displacement envelopes, PS10, PS15, and PS16

Shown in fig. 7.3.2 is a comparison of curvature profiles for PS15 and PS16, and the solid unjacketed pile with comparable transverse reinforcement, PS10. It may be observed that the jacketing of the pile actually served to increase the tendency of concentrated curvature; this was exacerbated by the unconfined plastic hinge in PS16

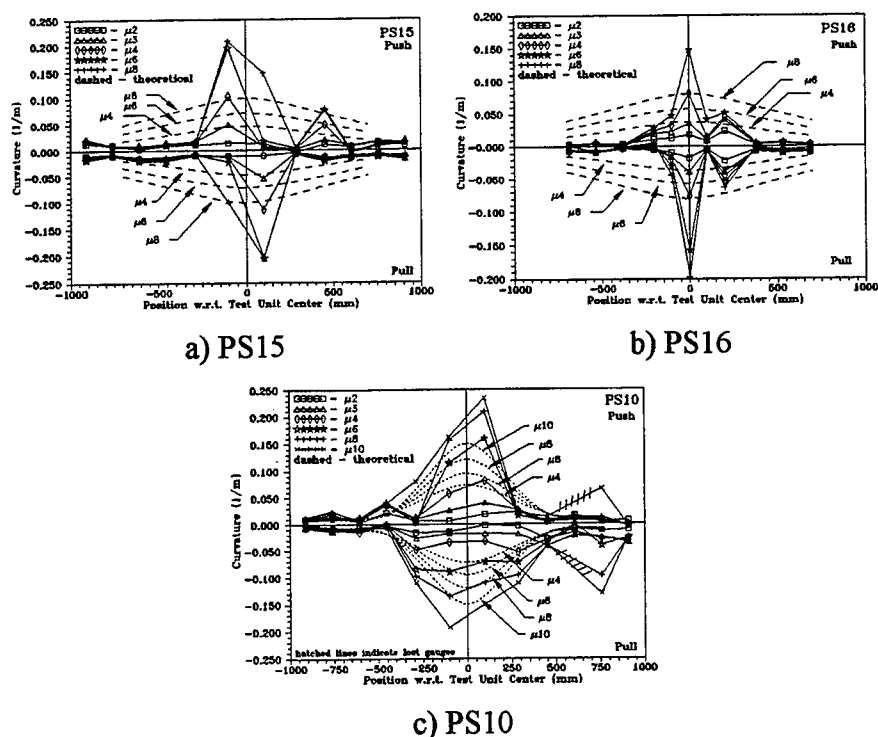


Fig. 7.3.2 : Comparison of curvature profiles: a) PS15 (glassfibre jacket, plastic hinge confined); b) PS16 (glassfibre jacket w/transverse slits, plastic hinge unconfined); c) PS10 (unjacketed, plastic hinge confined)...all had transverse reinforcement $\rho_t=0.005$

Predicated and experimentally derived plastic hinge lengths are shown in table 7.1. The concentration of curvature into the center of the plastic hinge region, which is so evident in the curvature profiles above, would lead one to expect a plastic hinge length far shorter than that predicted, and indeed this is the case.

**TABLE 7.1: PREDICTED AND ACTUAL PLASTIC HINGE LENGTH,
GLASSFIBRE-JACKETED PILES PS15 AND PS16**

Test Unit	External Confinement of Hinge	Predicted l_p (diameters D)	Actual l_p (diameters D)	$\frac{l_{p, actual}}{l_{p, pred.}}$
PS15	yes	2.26D	0.75D	0.33
PS16	no	2.26D	0.93D	0.41

Predicted and actual ultimate displacements are shown for PS15 and PS16 in table 7.2; in neither case did the test unit reach even 55% of the predicted displacement. As mentioned previously, this was most likely due to the inelastic rotations having to be borne by only a very short length of prestressing tendon in the area of flexure cracks.

**TABLE 7.2: PREDICTED VS. ACTUAL ULTIMATE DISPLACEMENT,
GLASSFIBRE-JACKETED PILES PS15 AND PS16**

Test Unit	External Confinement of Hinge	Predicted Δ_{ult}	Actual Δ_{ult}	$\frac{\Delta_{ult, exp.}}{\Delta_{ult, pred.}}$
PS15	yes	295 mm	139 mm	0.47
PS16	No	295 mm	149 mm	0.51

8. CONCLUSIONS AND RECOMMENDATIONS

8.1 Solid Prestressed Piles

This series of tests showed prestressed pile shafts to have a considerably greater plastic potential than has been commonly believed. Early tests, such as the first Santa Fe/Pomeroy series, showed the brittle failure characteristics of very lightly reinforced piles, and poor performance of very early prestressed piles in severe earthquakes led to a long-lasting mistrust of prestressed piles in all but completely elastic applications. This attitude has persisted even in the face of more recent experimental work which showed that precast prestressed piles could be designed for ductile response

Some conclusions that may be directly drawn from the testing of PS7 - PS10 are:

- 1) When there is no effective external confinement in the critical region, ρ_t has a strong influence on displacement ductility capacity, up to a volumetric transverse reinforcement ratio of about 0.02 for piles configured as those tested; beyond this point, the flexural ductility of the section is more likely to be governed by the ultimate tensile strain of the prestressing tendons than by the compressive strain capacity of the core.
- 2) The level of displacement ductility at which spalling (and, thus, the maximum flexural strength of the section) occurs is not influenced by the amount of transverse reinforcement.
- 3) The level of displacement ductility at which spalling occurs (between $\mu=2.5$ and $\mu=3$) is not influenced by the presence of external confinement; external confinement may reduce the suddenness of the concurrent drop in flexural strength, and will provide a somewhat higher (on the order of 10-20%) post-yield flexural strength.
The maximum practical ductility level that may be achieved in the presence of adequate soil confinement to the plastic hinge region is $\mu=8$.
- 4) Spalling of the cover concrete typically occurs at an extreme fibre compression strain of $\epsilon_c \approx 0.005 - 0.006$.
- 5) Plastic hinge length can be taken as equal to one pile diameter D .
- 6) When soil confinement occurs, ρ_t is ineffective in increasing ductility capacity; the most lightly reinforced test pile (PS10, with $\rho_t=0.005$) was taken to the tensile limit of the prestressing tendons without serious consequences to the transverse steel.

On the basis of these observations, it appears that a comparatively low level (on the order of $\rho_t=0.005$) of transverse reinforcement is sufficient for an in-ground hinge,

though a higher level ($\approx \rho_t = 0.010$) is appropriate for the hinge forming at the pile-cap interface.

8.2 Hollow Prestressed Piles

The testing of PS11-PS14 showed that hollow-section prestressed pile shafts have a remarkable insensitivity to most parameter variations. This was not entirely unexpected, but was still striking (note, in section 6.5, how the force-displacement response envelopes overlapped). The conclusions derived were as follows:

- 1) Failure was initiated when strain at the core's inner surface reached a value of about 0.005, and was caused by implosion, with rapid strength reduction. This was concurrent with spalling of the cover at $\mu=4$ for the hollow piles without Grade 60 longitudinal bars, and $\mu \approx 2.5$ for the pile with nonprestressed longitudinal bars.
- 2) The level of transverse reinforcement supplied to a hollow section has no influence on its ultimate ductility capacity.
- 3) The inclusion of nonprestressed longitudinal steel in the shaft's plastic hinge region provides no extra ductility; on the contrary, ductility is reduced by virtue of a higher yield displacement coupled with the same limiting concrete core strain. Addition of nonprestressed longitudinal bars may limit the amount of available curvature, and may cause early degradation in the shell when they buckle.
- 4) External confinement to the plastic hinge region has no effect on the available ductility capacity, but it does provide a somewhat 'softer' failure.
- 5) Hollow section prestressed piles have minimal energy-absorbing hysteretic behavior; they fail suddenly and violently, with the loss of most, if not all, of their lateral and axial load capacity.

It is clear from the results of testing PS11-PS14 that the use of hollow prestressed piles in seismic applications should be approached with caution, and that all efforts should be made to keep such members in the elastic range. Transverse reinforcement in a hollow section need only be specified for adequate shear capacity, and nonprestressed longitudinal steel should not be used unless necessary for the additional flexural strength it offers at the expense of ductility capacity.

8.3 Glassfibre-Jacketed Solid Prestressed Piles

The testing of PS15 and PS16 was intended to see whether external confinement to the subgrade hinge in the pile shaft could be 'built in', so to speak, and give the benefits of greatly increased ductility as seen in the testing of PS10 (which had low transverse reinforcement, but was nonetheless able to turn in an excellent performance through the presence of external confinement). For the configurations of wrap tested, the answer would seem to be, No.

- 1) The clamping effect of the jacket caused high very high strains to be developed over very short lengths of prestressing tendons (in the immediate vicinity of flexural cracks, which were few and far between). This led to total failure of the tendons, and 'sharp' pile shaft failure.
- 2) The plastic hinges developed were very much condensed, because rotation was concentrated at existing flexural cracks.
- 3) The confinement provided by the jacket added to the flexural strength by keeping the cover concrete mobilized in the compression zone.
- 4) The additional longitudinal reinforcement provided by the epoxy matrix and the cross-link fibres had little effect on the overall flexural strength.

Glassfibre wraps in the configurations tested are not suitable for use in the subgrade hinge region of a pile shaft; they may be useful at the pile head, where a condensed plastic hinge is already to be expected.

9. REFERENCES

1. Budek, A.M., Benzoni, G., and Priestley, M.J.N, An Analytical Study of the Inelastic Seismic Response of Reinforced Concrete Pile Shafts in Cohesionless Soil, Division of Structural Engineering, University of California at San Diego, La Jolla, California, Report No. SSRP 95/13, December 1995
2. Wood, J.H., and Phillips, M.H., "Lateral Stiffness of Bridge Foundations: Load Tests on Newman's Bridge", Report ST 87/2, Mills and Wood Consulting Engineers, Lower Hutt, New Zealand, 1987
3. Wood, J.H., and Phillips, M.H., "Lateral Stiffness of Bridge Foundations: Load Tests on Wai-iti Bridge", Report ST 88/1, Phillips and Wood Consulting Engineers, Lower Hutt, New Zealand, 1988
4. Wood, J.H., "Lateral Stiffness of Bridge Foundations: Load Tests on Matai River Bridge", Report ST 89/1, Phillips and Wood Consulting Engineers, Lower Hutt, New Zealand, 1989
5. Wood, J.H., "Lateral Stiffness of Bridge Foundations: Load Tests on the Charwell River Bridge", Report ST 90/2, Phillips and Wood Consulting Engineers, Lower Hutt, New Zealand, 1990
6. Cox, W.R., Reese, L.C., and Grubbs, B.R., "Field Testing of Laterally Loaded Piles in Sand", Proceedings of the Sixth Offshore Technology Conference, Houston, Texas, vol. 2, pp. 459-472
7. Priestley, M.J.N., "Mangere Bridge Foundation Cylinder Load Tests", MWD Central Laboratories Report No. 488, 1974
8. Sheppard, D.A., "Seismic Design of Prestressed Concrete Piling", PCI Journal, vol. 28, no. 2, March/April 1983, pp. 20-49
9. Ikeda, S., Tsubaki, T., and Yamaguchi, T., "Ductility Improvement of Prestressed Concrete Piles", Transactions of the Japan Concrete Institute, vol. 4, 1982, pp. 531-538
10. Banerjee, S., Stanton, J.F., and Hawkins, N.M., "Seismic Performance of Precast Concrete Bridge Piles", Journal of Structural Engineering, ASCE, vol. 113, no. 2, February 1987, pp. 381-396
11. Falconer, T.J., and Park, R., Ductility of Prestressed Concrete Piles under Seismic Loading, Research Report No. 82-6, Department of Civil Engineering, University of Canterbury, New Zealand, February 1982

12. NZS3101, The Design of Concrete Structures: Part 1 - Practice, Part 2 - Commentary, Standards Association of New Zealand, Wellington, New Zealand, 1982
13. Pam, H.J., Park, R., and Priestley, M.J.N., Seismic Performance of Prestressed Concrete Piles and Pile-Pile Cap Connections, Research Report 88-3, Department of Civil Engineering, University of Canterbury, New Zealand, March 1988
14. Muguruma, H., Watanabe, F., and Nishiyama, M., "Improving the Flexural Ductility of Pretensioned High Strength Spun Concrete Piles by Lateral Confining of Concrete", Proceedings of the Pacific Conference on Earthquake Engineering, vol. 1, Wairakei, New Zealand, August 1987, pp. 385-396
15. Budek, A.M., Benzoni, G., and Priestley, M.J.N., The Effect of External Confinement and Transverse Reinforcement on Plastic Hinges in Cast-in-Place Pile Shafts, Division of Structural Engineering, University of California at San Diego, La Jolla, California, Report No. SSRP 97/04, June 1997
16. Kowalsky, M., Priestley, M.J.N., and Seible, F., Shear Behavior of Lightweight Concrete Columns under Seismic Conditions, Division of Structural Engineering, University of California at San Diego, La Jolla, California, Report No. SSRP 95/10, July 1995
17. Priestley, M.j.n., Seible, F., and Calvi, G, Seismic Design and Retrofit of Bridges, John Wiley and Sons, New York, 1996

